



Title	Coherent control of nuclear spins in GaAs using spin injection techniques from a half-metallic spin source
Author(s)	秋保, 貴史
Citation	北海道大学. 博士(工学) 甲第11751号
Issue Date	2015-03-25
DOI	10.14943/doctoral.k11751
Doc URL	http://hdl.handle.net/2115/58792
Type	theses (doctoral)
File Information	Takafumi_Akiho.pdf



[Instructions for use](#)

**Coherent control of nuclear spins in GaAs using spin
injection techniques from a half-metallic spin source**

Takafumi Akiho

Division of Electronics for Informatics

Graduate School of Information Science and Technology

Hokkaido University

February 2015

Copyright (C) 2015 Takafumi Akiho. All Rights Reserved.

Contents

1. Introduction.....	1
1.1 Background.....	1
1.1.1 Nuclear spins for implementing quantum bits.....	1
1.1.2 Highly polarized spin source	3
1.1.3 Spin-dependent transport properties of semiconductors.....	3
1.2 Purpose	5
2. Principle of spin injection/detection of electron spins and nuclear spins	11
2.1 Conductance mismatch problem.....	12
2.2 Nonlocal local, and three-terminal geometry	13
2.3 Spin signals.....	13
2.3.1 Spin-valve effect.....	15
2.3.2 Hanle effect.....	16
2.4 Spin orbit interaction	18
2.5 Influence of nuclear spins	20
2.5.1 Oblique Hanle effect	20
2.5.2 Nuclear magnetic resonance.....	22
3. Spin injection into GaAs and development of a highly polarized spin source	25
3.1 Introduction.....	26
3.2 Experimental methods	27
3.3 Experimental results	30
3.3.1 Structural properties of CoFe/MgO/n-GaAs	30

3.3.2 Effect of MgO barrier insertion on junction resistance and TAMR characteristics	31
3.3.3 Effect of MgO barrier insertion on non-local spin valve effect...	33
3.4 Discussion.....	35
3.4.1 Effect of MgO barrier insertion on TAMR characteristics	35
3.4.2 Effect of MgO barrier insertion on non-local spin-valve effect ..	36
3.5 Experimental results for Co ₂ MnSi/CoFe/n-GaAs	39
3.5.1 Structural properties of Co ₂ MnSi/CoFe/n-GaAs.....	39
3.5.2 TAMR effect for Co ₂ MnSi/CoFe/n-GaAs	40
3.5.3 All electrical injection and detection of spin-polarized electrons through the observation of spin-valve signals and Hanle signals.....	41
3.6 Comparison of spin polarization between Co ₂ MnSi and CoFe	44
3.7 Summary.....	47
4. All electrical investigation of spin dependent transport properties of strained InGaAs channels	51
4.1 Introduction.....	52
4.2 Experimental methods.....	53
4.3 Experimental results	53
4.3.1 Structural properties of strained InGaAs channels	53
4.3.2 Electrical detection of spin injection	55
4.4. Discussion on the possible origin of the reduction of spin lifetime in strained InGaAs	58
4.5. Summary.....	60

5. Electrical detection of dynamically polarized nuclear spins and coherent control of nuclear spins through nuclear magnetic resonance.....	63
5.1 Introduction.....	64
5.2 Experimental methods	66
5.3 Experimental results and discussion.....	68
5.3.1 Electrical detection of Overhauser field in a lateral spin transport device using $\text{Co}_2\text{MnSi}/\text{CoFe}/\text{n-GaAs}$ junctions	68
5.3.2 Transient behavior of nuclear spins through the electrical detection of oblique Hanle signals.....	70
5.3.3 Estimation of nuclear field strength.....	72
5.4 Coherent control of nuclear spins in GaAs.....	75
5.4.1 Electrical detection of NMR in GaAs using Co_2MnSi	75
5.4.2 Coherent control of nuclear spins using pulsed NMR.....	79
5.5 Summary.....	82
6. Conclusion	87
Acknowledgements	89
Appendix.....	91

Chapter 1

Introduction

1.1 Background

1.1.1 Nuclear spins for implementing quantum bits

Spintronics, which utilizes the spin degree of freedom of electrons, has attracted much attention as a way to create innovative devices. Magnetic random access memory (MRAM) is a promising candidate for a universal memory device because MRAM features high density, high-speed operation, low-power consumption, non-volatility, and high read/write endurance.^{1,2} Each cell of the MRAM is made from a transistor and a magnetic tunnel junction, which consists of two ferromagnetic electrodes sandwiching a thin tunnel barrier. Therefore, development of magnetic tunnel junctions (MTJs) will enable development of high-performance MRAM. Although spintronics devices based on ferromagnet metals have been partially commercialized, the degree of freedom of electrons in semiconductors, which plays an important role in electronics such as logic and communication function is not fully utilized. Development of semiconductor-based spintronics devices such as spin transistors and nuclear spin quantum bits is thus an important step towards spin based logic and communication function.

Nuclear spins in semiconductors are an ideal system for implementing quantum bits because of their extremely long coherence time.³ A quantum algorithm using the liquid-state nuclear spins of ^1H and ^{13}C atoms in a chloroform molecule was

experimentally demonstrated using standard nuclear magnetic resonance (NMR) techniques.⁴ However, development of quantum bits using a solid-state device and efficient polarization of nuclear spins for a high signal-to-noise ratio are required for achieving a scalable quantum computer. A hyperfine interaction transfers the angular momentum from the polarized electrons to the nuclei, leading to effective polarization of the nuclear spins. This is, referred to as “dynamic nuclear polarization (DNP).” For example, with a magnetic field of 0.1 T and a temperature of 4.2 K, the nuclear spin polarization of ⁶⁹Ga is of the order of 10⁻⁶. However, in DNP, the nuclear spin polarization is typically 3–4 orders of magnitude larger than that without DNP under the same conditions. Highly efficient DNP has been achieved in bulk GaAs,⁵ GaAs/AlGaAs quantum wells,⁶ and InAlAs quantum dots⁷ using optical methods.

Machida et al. recently demonstrated coherent control of nuclear spins using pulsed NMR techniques for a quantum-Hall device fabricated on a GaAs/AlGaAs single heterostructure.⁸ The initial state of the nuclear spins was set by using polarized electron spins on the edge channel in the device. Application of a pulsed rf-magnetic field caused the nuclear spin-state to evolve coherently. The final state of nuclear spins was derived from the edge-channel conductance. However, quantum Hall devices work only in quantum Hall states with an extremely large magnetic field (> 5 T) and low temperature (< 1 K).

Sanada et al. demonstrated coherent control of nuclear spins in GaAs/AlGaAs(110) quantum wells.⁹ They set the initial state of nuclear spins by using optically excited electron spins. The nuclear spin state was controlled by application of a pulsed rf-magnetic field, and the final state of the nuclear spins was derived from the Kerr rotation signal. They estimated the intrinsic phase coherence time T_2 of the constituent nuclei by optically detecting the spin echo and found that T_2 depended on the orientation of the static magnetic field with respect to the crystalline axis, as expected from nearest neighbor dipole-dipole interaction. However, the device size for optical polarization and detection of nuclear spins is limited to a few ten μm due to the incident light diameter.

Injection of spin-polarized electrons from a ferromagnetic electrode into a semiconductor creates spin-polarized electronic states in a nanoscale semiconductor region. In 2007, Lou et al. first demonstrated electrical detection of spin injection into GaAs using a lateral spin transport device with Fe electrodes.¹⁰ So far, several groups have demonstrated spin injection into GaAs, Si, Ge, or graphene as possible candidates for spin

transistors.¹⁰⁻¹⁵ NMR along with DNP was recently demonstrated in spin injection devices with Fe/GaAs^{16,17} or GaMnAs/GaAs¹⁸ structures. However, coherent control of nuclear spins using spin injection devices has not been demonstrated because the spin injection efficiency in most of these devices is of the order of a few percent. Thus, a highly polarized spin source is indispensable achieving a semiconductor-based quantum bit as well as other spintronics devices such as spin transistors.

1.1.2 Highly polarized spin source

Co-based Heusler alloys are a promising candidate for a highly polarized spin source because of the half-metallic ferromagnetic nature theoretically predicted for many of these alloys.^{19, 20} Liu et al. demonstrated a giant tunneling magnetoresistance (TMR) ratio of nearly 2000% using Mn-rich Co₂MnSi-based MTJs,²¹ and the effects of non-stoichiometry on the half-metallic characteristic of Heusler alloys Co₂MnSi and Co₂MnGe have been investigated.^{22,23} Although there have been several reports on spin injection into semiconductors using spin LEDs with Co-based Heusler alloy electrodes,^{24, 25} the reported spin-injection efficiency of these devices was less than that of those with Fe electrodes. Moreover, there has been no report on the electrical detection of spin injection using a spin injection device with Heusler alloy electrodes. Thus, the applicability of Co-based Heusler alloys to spin injection has not been fully clarified.

Another possible approach to achieving efficient spin injection is to introduce an epitaxial MgO barrier. Butler et al. theoretically predicted large magnetoresistance in an Fe/MgO/Fe epitaxial MTJ.²⁶ They pointed out that the tunneling conductance strongly depends on the symmetry of the Bloch states in the electrodes and on the evanescent states in the barrier layer. In an epitaxial MgO barrier, the decay of Δ_1 evanescent states is slower than that of the other evanescent states, resulting in the conductance being dominated by the Δ_1 Bloch state. Moreover, the Δ_1 Bloch state of Fe electrodes appears in only the majority-spin band, leading to a high tunneling magnetoresistance ratio. Yuasa et al., fabricated fully epitaxial Fe/MgO/Fe MTJs and demonstrated a higher TMR ratio, which was attributed to the coherent tunneling effect,²⁷ than that of MTJs with an AlOx amorphous tunnel barrier. For spin injection into a semiconductor, Wang et al. achieved relatively high spin injection efficiency even at room temperature for a CoFe/MgO/GaAs spin-LED.²⁸

1.1.3 Spin-dependent transport properties of semiconductors

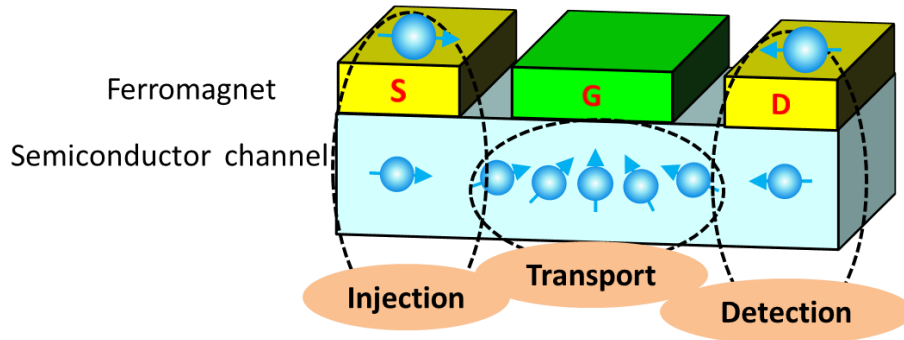


Figure 1.1. Schematic images of spin transistor proposed by Datta and Das. Electron spins are injected from ferromagnet source(S) contact and are detected at ferromagnet drain(D) contact. Polarized spins are controlled by a gate controllable spin-orbit-interaction.

Along with efficient spin injection and detection, understanding the spin-dependent transport properties such as hyperfine interaction and spin-orbit interaction (SOI) in semiconductor channels is important for achieving semiconductor-based spintronics devices. As described in section 1.1.1, the interplay between electron spins and nuclear spins due to the hyperfine interaction has been studied extensively for application to quantum information devices based on nuclear spins as well as for understanding the transport properties of electron spins in semiconductors.

The SOI plays a key role in the operation of the spin transistor proposed by Datta and Das.²⁹ The Datta-Das type spin transistor has a structure similar to that of general transistors except that the source and drain contacts are replaced with ferromagnetic electrodes. Electron spins are injected from a ferromagnetic source contact into a semiconductor channel. The direction of electron spins is controlled using gate-controllable SOI because the spin-orbit interaction works as an effective magnetic field for electron spins without an external magnetic field. Finally, the injected electron spins are detected by a ferromagnetic drain contact. In III–V semiconductors such as GaAs and InAs ones, Rashba-type SOI³⁰ originating from structural inversion asymmetry and Dresselhaus-type SOI³¹ originating from bulk inversion asymmetry affect electron spins. Of particular importance is that Rashba-type SOI can be controlled by adjusting the gate

voltage. Thus, III-V semiconductors are promising materials for achieving a Datta-Das spin transistor.

The effects of SOI on the spin-dependent transport properties of InGaAs/InAlAs quantum wells were investigated using electrical methods,^{32,33} and the effects on those of GaAs/AlGaAs quantum wells were investigated using optical methods.^{34,35} Strain due to pseudomorphic growth also induces SOI. Kato et al., recently investigated the effect of SOI on the spin transport properties of strained InGaAs channels and found that effective SOI fields were obtained even in bulk semiconductors.³⁶ Investigation of the spin-dependent transport properties of semiconductor channels in which SOI strongly affects the electron spins is important for achieving a Datta-Dass spin transistor.

1.2 Purpose

The broad purpose of this research is to develop key technologies for the creation of semiconductor-based spintronic devices such as nuclear spin quantum bits and spin transistors. The purpose of the work reported in this dissertation is to achieve highly efficient spin injection and detection, to clarify spin-dependent transport properties of semiconductors in which spin orbit interaction strongly affects electron spins, and to demonstrate coherent control of nuclear spins in GaAs. Following five points in particular are focused on here.

1. The effect of MgO barrier insertion on electrical spin injection in CoFe/n-GaAs heterojunctions
2. The effect of a Heusler alloy Co₂MnSi as a spin source on electrical spin injection in Co₂MnSi/CoFe/n-GaAs heterojunctions
3. The spin-dependent transport properties of strained InGaAs channels using all-electrical spin injection and detection
4. The electrical detection of dynamically polarized nuclear spins in transient states using Co₂MnSi/CoFe/n-GaAs heterojunctions
5. The electrical detection of nuclear magnetic resonance and coherent control of nuclear spins using Co₂MnSi/CoFe/n-GaAs heterojunctions for nuclear spin quantum bits

This dissertation is organized as follows. In chapter 1, the background and purpose of this study are described.

In chapter 2, principles of electrical detection of electron spins and dynamically polarized nuclear spins using ferromagnet/semiconductor heterojunctions are explained.

In chapter 3, the effects of inserting an MgO barrier and of using a Co_2MnSi spin source on the spin injection properties are described. Introducing an MgO tunnel barrier produced a larger spin signal than that in a sample without MgO. Also described is the first reported demonstration of the electrical detection of spin injection into a semiconductor using a Heusler alloy as a Co_2MnSi spin source via an ultrathin CoFe insertion layer,³⁷ which resulted in much higher spin injection efficiency than for a sample with a CoFe spin source.³⁸ These results indicate that the use of an MgO tunnel barrier and of a Heusler alloy are promising for achieving efficient spin injection into a semiconductor.

In chapter 4, the investigation of the spin-dependent transport properties of strained InGaAs channels is described. Experiments showed that the spin lifetime in strained InGaAs channels is much shorter than that in GaAs channels. A strain-induced SOI model revealed that the reduction in spin lifetime may have been due to the effective magnetic field created by spin orbit interaction originating from strain.

In chapter 5, the coherent control of nuclear spins in a semiconductor for nuclear spin quantum bits is described, and a novel NMR system using spin injection devices is proposed for quantum bit applications. Figure 1.2 shows a schematic image of a nuclear spin quantum bit device using spin injection techniques. The device works as follows. (1) Electron spins are injected from a ferromagnetic electrode into GaAs, (2) the nuclear spins are polarized using DNP, (3) the nuclear spin quantum bits are controlled using NMR, and (4) the nuclear spin state is derived by detecting the nuclear field acting on the electron spins. The development of such a device requires the development of technologies for efficient polarization, control, and detection of nuclear spin states. Investigation of the transient behavior of nuclear spins using oblique Hanle measurements revealed a way to initialize the nuclear spins. We electrically detected dynamically polarized nuclear spins, nuclear magnetic resonance by applying an rf-magnetic field, and achieved coherent oscillation of the nuclear spin states. These results correspond to initialization, control, and detection of the spin states for quantum bits.

In chapter 6, the main results of this dissertation are summarized.

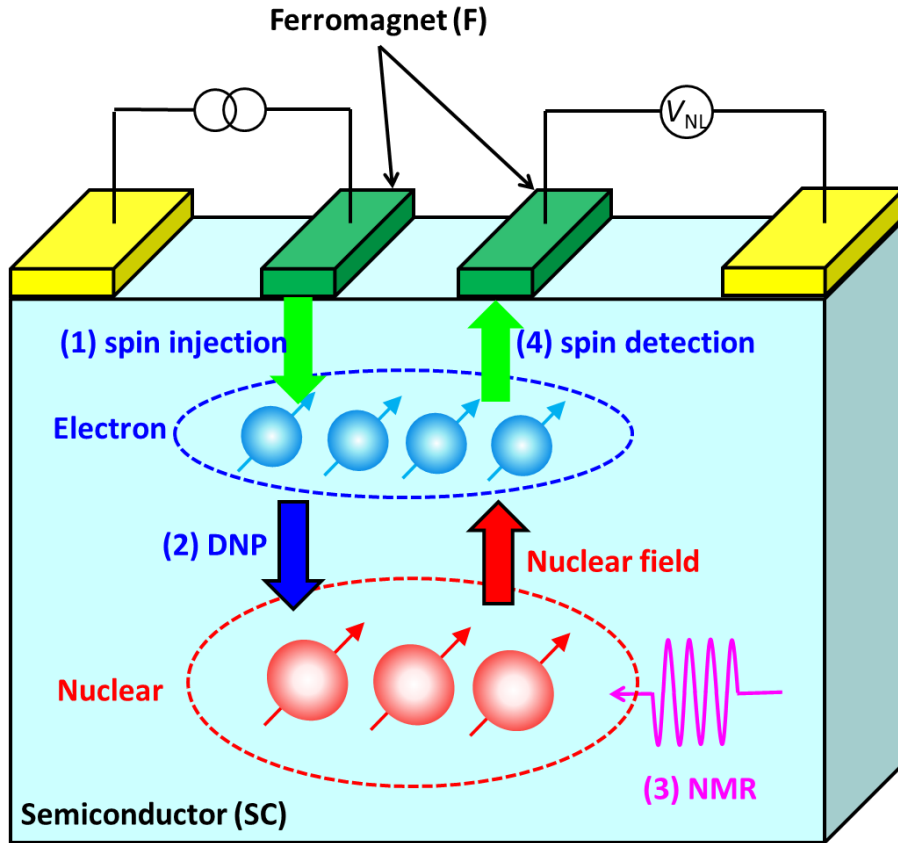


Figure 1.2. Novel NMR system using spin injection device for quantum bit applications. (1) Electron spin injection from Co_2MnSi into GaAs, (2) nuclear spin polarization using DNP, (3) quantum control of nuclear spin quantum bits using NMR, and (4) finally, determination of nuclear spin state by detecting nuclear field acting on electron spins.

References

- ^{1.} S. A. Wolf, D. D. Awschalom, R. A. Buhrman, J. M. Daughton, S. von Molnár, M. L. Roukes, A. Y. Chtchelkanova and D. M. Treger, *Science* **294**, 1488 (2001).
- ^{2.} I. Žutić, J. Fabian, and S. Das Sarma, *Rev. Mod. Phys.* **76**, 323 (2004).
- ^{3.} M. A. Nielsen and I. L. Chuang, *Quantum Computation and Quantum Information* (Cambridge Univ. Press, Cambridge, 2000).
- ^{4.} I. L. Chuang, L. M. K. Vandersypen, X. Zhou, D. W. Leung, and S. Lloyd, *Nature* (London) **393**, 143 (1998).
- ^{5.} J. M. Kikkawa and D. D. Awschalom, *Science* **287**, 473 (2000).
- ^{6.} G. Salis, D. D. Awschalom, Y. Ohno, and H. Ohno, *Phys. Rev. B*, **64**, 195304 (2001).
- ^{7.} R. Kaji, S. Adachi, H. Sasakura, and S. Muto, *Phys. Rev. B* **77**, 115345 (2008).
- ^{8.} T. Machida, T. Yamazaki, K. Ikushima, and S. Komiyama, *Appl. Phys. Lett.* **82**, 409 (2003).
- ^{9.} H. Sanada, Y. Kondo, S. Matsuzaka, K. Morita, C. Y. Hu, Y. Ohno, and H. Ohno, *Phys. Rev. Lett.* **96**, 067602 (2006).
- ^{10.} X. Lou, C. Adelman, S. A. Crooker, E. S. Garlid, J. Zhang, K. S. M. Reddy, S. D. Flexner, C. J. Palmstrøm, and P. A. Crowell, *Nat. Phys.* **3**, 197 (2007).
- ^{11.} G. Salis, A. Fuhrer, R. R. Schlitter, L. Gross, and S. F. Alvarado, *Phys. Rev. B* **81**, 205323 (2010).
- ^{12.} T. Uemura, T. Akiho, M. Harada, K.-i. Matsuda, and M. Yamamoto, *Appl. Phys. Lett.* **99**, 082108 (2011).
- ^{13.} T. Sasaki, T. Oikawa, T. Suzuki, M. Shiraishi, Y. Suzuki, and K. Noguchi, *IEEE Trans. Magn.* **46**, 1436 (2010).
- ^{14.} Y. Zhou, W. Han, L.-T. Chang, F. Xiu, M. Wang, M. Oehme, I. A. Fischer, J. Schulze, R. K. Kawakami, and K. L. Wang, *Phys. Rev. B* **84**, 125323 (2011).
- ^{15.} T. Maassen, I. J. Vera-Marun, M. H. D. Guimarães, and B. J. van Wees, *Phys. Rev. B* **86**, 235408 (2012).
- ^{16.} M. K. Chan, Q. O. Hu, J. Zhang, T. Kondo, C. J. Palmstrøm, and P. A. Crowell, *Phys. Rev. B* **80**, 161206(R) (2009).
- ^{17.} G. Salis, A. Fuhrer, and S. F. Alvarado, *Phys. Rev. B* **80**, 115332(R) (2009).
- ^{18.} J. Shiogai, M. Ciorga, M. Utz, D. Schuh, T. Arakawa, M. Kohda, K. Kobayashi, T. Ono, W. Wegscheider, D. Weiss, and J. Nitta, *Appl. Phys. Lett.* **101**, 212402 (2012).

19. S. Ishida, S. Fujii, S. Kashiwagi, and S. Asano, *J. Phys. Soc. Jpn.* **64**, 2152 (1995).
20. S. Picozzi, A. Continenza, and A. J. Freeman, *Phys. Rev. B* **66**, 094421 (2002).
21. H. Liu, Y. Honda, T. Taira, K. Matsuda, M. Arita, T. Uemura, M. Yamamoto, *Appl. Phys. Lett.* **101**, 132418 (2012).
22. V. R. Singh, V. K. Verma, K. Ishigami, G. Shibata, T. Kadono, A. Fujimori, D. Asakura, T. Koide, Y. Miura, M. Shirai, G.-f. Li, T. Taira, and M. Yamamoto, *Phys. Rev. B* **86**, 144412 (2012)
23. G.-f. Li, Y. Honda, H.-x. Liu, K.-i. Matsuda, M. Arita, T. Uemura, M. Yamamoto, Y. Miura, M. Shirai, T. Saito, F. Shi, and P. M. Voyles, *Phys. Rev. B* **89**, 014428 (2014).
24. X. Y. Dong, C. Adelmann, J. Q. Xie, C. J. Palmstrøm, X. Lou, J. Strand, P. A. Crowell, J.-P. Barnes and A. K. Petford-Long, *Appl. Phys. Lett.* **86**, 102107 (2005).
25. M. C. Hickey, C. D. Damsgaard, I. Farrer, S. N. Holmes A. Husmann, J. B. Hansen, C. S. Jacobsen, D. A. Ritchie, R. F. Lee, G. A. C. Jones, and M. Pepper, *Appl. Phys. Lett.* **86**, 252106 (2005).
26. W. H. Butler, X.-G. Zhang, and T. C. Schulthess, *Phys. Rev. B* **63**, 054416 (2001).
27. S. Yuasa, A. Fukushima, T. Ngahama, K. Ando, and Y. Suzuki, *Jpn. J. Appl. Phys.* **43**, 588 (2004).
28. R. Wang, X. Jiang, R. M. Shelby, R. M. Macfarlane, and S. S. P. Parkin, *Appl. Phys. Lett.* **86**, 052901 (2005).
29. S. Datta and B. Das, *Appl. Phys. Lett.* **56**, 665 (1990).
30. E. I. Rashba, *Sov. Phys. Solid State* **2**, 1109 (1960).
31. P. D. Dresslhaus, C. M. A. Papavassiliou, R. G. Wheeler, and R. N. Sacks, *Phys. Rev. Lett.* **68**, 106 (1992).
32. J. Nitta, T. Akazaki, H. Takayanagi, and T. Enoki, *Phys. Rev. Lett.* **78**, 1335 (1997).
33. S. Faniel, T. Matsuura, S. Mineshige, Y. Sekine, and T. Koga, *Phys. Rev. B* **83**, 115309 (2011).
34. M. P. Walsesr, C. Reichl, W. Wegscheider, and G. Salis, *Nature Phys.* **8**, 757, (2012).
35. H. Sanada, T. Sogawa, H. Gotoh, K. Onomitsu, M. Kohda, J. Nitta, and P. V. Santos, *Phys. Rev. Lett.* **106**, 216602 (2011).
36. Y. Kato, R. C. Myers, A. C. Gossard, and D. D. Awschalom, *Nature (London)*, **427**, 50 (2004).

- ^{37.} T. Akiho, J. Shan, H.-x. Liu, K.-i. Matsuda, M. Yamamoto, and T. Uemura, *Phys Rev. B*, **87**, 235205 (2013).
- ^{38.} Y. Ebina, T. Akiho, H.-x. Liu, M. Yamamoto, and T. Uemura, *Appl. Phys. Lett.* **104**, 172405 (2014).

Chapter 2

Principle of spin injection/detection of electron spins and nuclear spins

In this chapter, principles of detection for polarized electron spins and nuclear spins in semiconductors are briefly described. First, the conductivity mismatch problem which prohibits spin injection from a ferromagnet into a semiconductor is briefly derived. To solve the conductivity mismatch problem, an insertion of a tunnel barrier is effective. Second, a nonlocal geometry which is widely used for the electrical detection of spin injection is described comparing with other measurement configuration. Then, expected spin signals of spin-valve effect and Hanle effect observed in the nonlocal geometry are explained. Explanation of these two is meaningful to read this dissertation, because experimentally obtained both signals are investigated throughout this dissertation. Spin orbit interaction which affects to electron spins as an effective magnetic field is also briefly described. Finally, an electrical detection method of nuclear magnetic field due to polarized nuclear spins and nuclear magnetic resonance are described.

2.1 Conductance mismatch problem

Schmidt et al., pointed out that the fundamental obstacle to spin injection across a ferromagnetic metal and a semiconductor interface is their conductivity mismatch.¹ Figure 2.1 shows a resistor model with an up-spin channel and a down-spin channel in a parallel magnetization configuration. Conductance for the ferromagnet layers is given by

$$\sigma_{FM\uparrow(\downarrow)} = \frac{\sigma_{FM}(1 \pm \beta)}{2} \quad (2.1)$$

where $\sigma_{FM\uparrow(\downarrow)}$ is the conductance for the up (down) spin path of a ferromagnetic layer, σ_{FM} is the total conductance of the ferromagnet layer, the + (–) sign refers to the up (down) spin path on the ferromagnet layer, and β is the spin polarization of the ferromagnetic layer. The same parameter values are assumed for the two ferromagnet layers. Both spin channels exhibit half the total conductivity of the semiconductor layer:

$$\frac{\sigma_{SC\uparrow}}{2} = \frac{\sigma_{SC\downarrow}}{2} = \sigma_{SC} \quad (2.2)$$

Spin polarization (α) of the circuit is obtained using an equivalent circuit model, as shown in figure 2.1.

$$\alpha = \frac{j_{\uparrow} - j_{\downarrow}}{j_{\uparrow} + j_{\downarrow}} = \frac{2(R_{FM\downarrow} - R_{FM\uparrow})}{2(R_{FM\downarrow} + R_{FM\uparrow}) + R_{SC}} \quad (2.3)$$

where $j_{\uparrow(\downarrow)}$ is the current density for the up (down) spin path, $R_{FM\uparrow(\downarrow)}$ is the resistance of the ferromagnet layers for the up (down) spin path, and R_{SC} is the resistance of the semiconductor layer. Using Eq. (2.1), (2.2), and (2.3), one can obtain α .

$$\alpha = \frac{2\beta(\sigma_{SC}/\sigma_{FM})}{2(\sigma_{SC}/\sigma_{FM}) + 1 - \beta^2} \quad (2.4)$$

According to Eq. 2.4, the value of α under typical conditions ($\beta = 60\%$, and $\sigma_{FM} = 10^4\sigma_{SC}$) is 0.007%. Thus, the difference in resistance between parallel and antiparallel magnetization of the contacts is impossible to detect. To solve this conductivity mismatch problem, Rashba,² and Fert and Jaffres³ proposed introducing of a tunneling barrier between the ferromagnetic metal and the semiconductor. The introduction of a tunneling barrier corresponds to effectively enhancing of R_{FM} .

In 2007, Lou et al., first demonstrated electrical detection of spin injection into GaAs

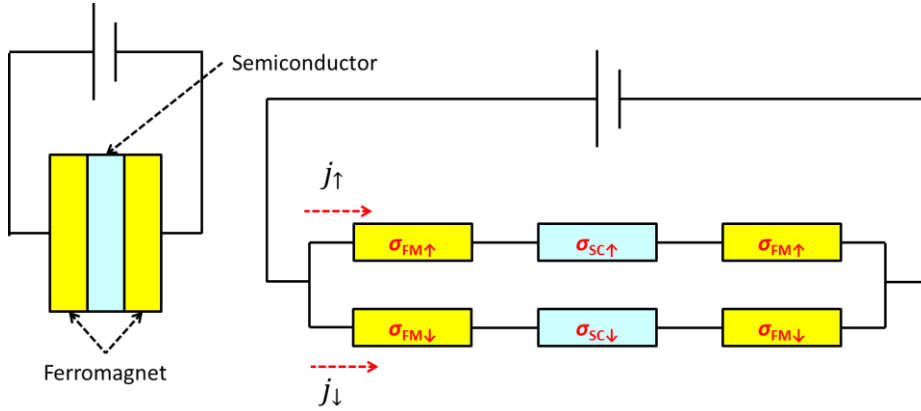


Figure 2.1. Simplified resistor model for device consisting of semiconductor with two ferromagnetic contacts. Two independent spin paths are represented by resistors.

using a lateral spin transport device with Fe electrodes.⁴ To introduce a tunnel barrier, a heavily doped GaAs layer between the Fe electrodes and GaAs channel was prepared, thereby forming a Schottky tunnel barrier. They measured spin signals in a nonlocal geometry⁵ into which spin-polarized currents were injected from an Fe electrode and detected spin currents by using another Fe electrode located a few μm from the other ones.

2.2 Nonlocal, local, and three-terminal geometry

Figure 2.2(a) shows a schematic nonlocal geometry. In the nonlocal geometry, injected electron spins diffuse a distance, $l_{sf} = \sqrt{D\tau}$, where D is the electron diffusion constant, and before losing memory of their initial polarization via spin relaxation event characterized by the time τ . The population of polarized spins is detected by a nonlocal contact-3 as a voltage. In this geometry, the amplitude of spin signal as a function of distance between the injector and detector contacts (d) gives the direct information of l_{sf} . For GaAs, around 3~5 μm of l_{sf} was reported.^{4,6,7} For the detection of spin signals in the nonlocal geometry, micro-fabrication techniques are necessary to prepare narrow junctions within a few μm space. Fabrication procedures for spin injection devices with electron beam lithography is usually complicated, however, this method is applicable for all conducting materials including metals and semiconductors.

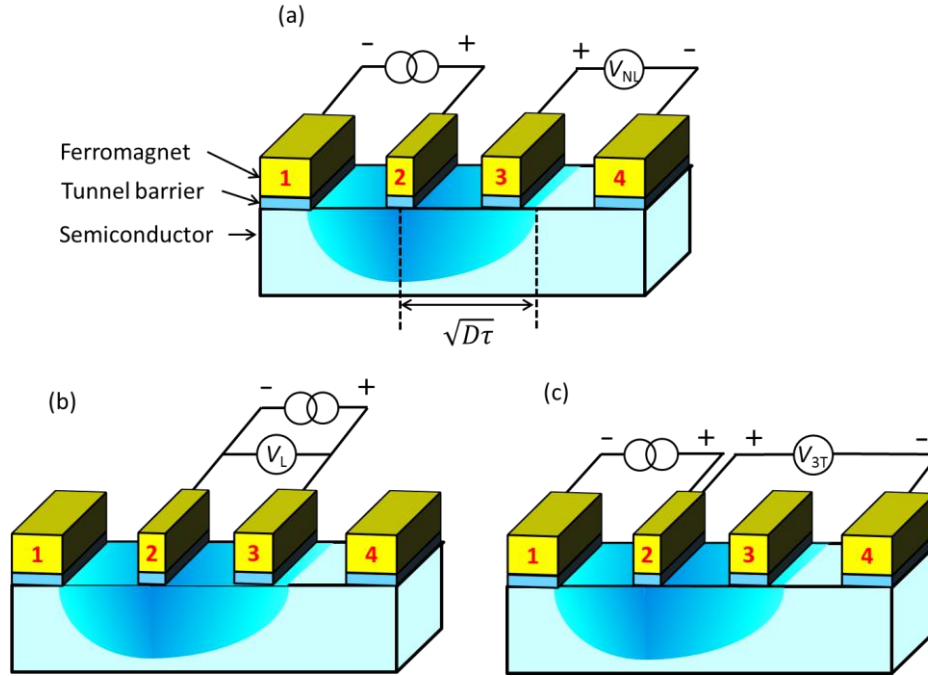


Figure 2.2. Circuit configurations of (a) a four-terminal nonlocal geometry, (b) a local geometry, and (c) three-terminal geometry.

Electrical detection of polarized electrons in a local geometry as shown in figure 2.2(b) is important for the device application of spin transistors,^{8,9} because the injector and detector contacts can be recognized as source and drain contacts of spin transistor. However, magnetoresistance characteristics in the local geometry may contain the influence of (local) Hall effects and tunneling anisotropic magnetoresistance (TAMR) effects.¹⁰ These MR effects are not originating from transported electron spins, but magnetization switching of the single ferromagnet/semiconductor heterojunctions. For the evidence of spin injection, observation of spin-valve signal and Hanle signal in the nonlocal geometry are rigorous.

Figure 2.2(c) shows a circuit configuration of three-terminal geometry or DC four probe method. In this geometry, one can measure I - V characteristics for junctions and TAMR characteristics. In the TAMR effect, the tunneling resistance depends on the magnetization direction. Therefore, from the observation of TAMR signal, one can obtain the magnetization characteristics such as easy (hard) magnetization direction and a coercive

force.

S. P. Dash reported Hanle-like MR signal in the three-terminal geometry by applying magnetic field perpendicular to the sample plane in Ferromagnet/tunnel barrier/Si structures.¹¹ However, based on a standard model described in the next section, spin polarization for the Ferromagnet/tunnel barrier/Si junctions were beyond 100%. Moreover, we reported Hanle-like MR signals in the three-terminal geometry proportional to the junction resistance,¹² although the spin signals are not proportional to the junction resistance in the standard model. Thus, Hanle-like MR signals in the three-terminal geometry should be carefully treated.

2.3 Spin signals

2.3.1 Spin-valve effect

To obtain spin-valve signals, applying an injection current between the contact-1 and -2, measure nonlocal voltage between the contact-3 and -4 (nonlocal geometry) and sweep in-plane magnetic field ($B_{||}$). Consider a ferromagnet electrode on a nonmagnetic material at $x = 0$ and injected electron spins diffuse along x direction. Figure 2.3(a) shows a splitting of electro chemical potential for up and down spins. Due to diffusion currents, electron spins flow to the right side direction ($x > 0$). In a parallel magnetization configuration for the detector and injector contact, the detector contact sense the down-spin state. On the other hand, in the anti-parallel configuration, the detector contact senses the up-spin state. Therefore, by applying in-plane magnetic field and switching magnetization configuration, the level of nonlocal voltage changes. That is spin-valve effect. Figure 2.3(b) shows a schematic spin-valve signal. P and AP in the Fig. 2.3(b) represent the parallel and anti-parallel configuration. The amplitude of spin-valve signal is given by,

$$\Delta V_{NL} = P_{inj}P_{det} \frac{\rho l_{sf}}{A} \exp\left(-\frac{d}{l_{sf}}\right) I \quad (2.5)$$

where, $P_{inj(det)}$ is spin polarization of the injector (detector) contact, ρ is resistivity of the channel, A is the area of the channel cross-section, and d is the distance between injector and detector contacts. From the amplitude of spin signals, one can estimate values of spin polarization.

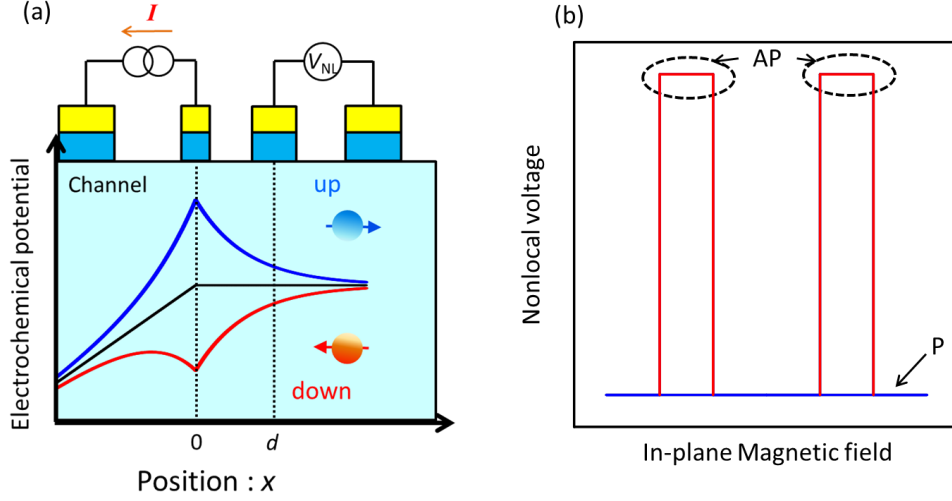


Figure 2.3. (a) Splitting of electro chemical potential for up and down spins. Due to diffusion currents, electron spins flow to the right side direction. (b) Schematic spin-valve signal. P and AP indicate parallel and anti-parallel magnetization configuration for the injector and detector contact.

2.3.1 Hanle effect

Injected electron spins from a ferromagnetic electrode into semiconductor channels precess when out-of-plane magnetic field (B_z) is applied as shown in Fig. 2.4(a). That is Hanle effect. Hanle effect is described using a drift-diffusion model given by,¹³

$$\frac{\partial \mathbf{S}}{\partial t} = \mathbf{S} \times \boldsymbol{\omega} + D \nabla^2 \mathbf{S} - \mu E \nabla \mathbf{S} - \frac{\mathbf{S}}{\tau}, \quad (2.6)$$

$$\omega_L = \frac{g \mu_B B_z}{\hbar}, \quad (2.7)$$

where S is a density of injected electron spins, μ is a mobility of electron, \mathbf{E} is an electric field, ω_L is the Larmor frequency, g is an electron g factor (-0.44 for GaAs), μ_B is the Bohr magneton, and \hbar is the reduced Planck's constant. The first term on the right-hand side describes spin precession, while the rest describe spin diffusion, spin drift, and spin

relaxation, respectively. Figure 2.4(b) shows a schematic Hanle signal using steady state solution of Eq. 2.6 with different the magnetization configuration of the parallel and antiparallel, respectively. These behaviors are explained as follows. In the parallel (antiparallel) configuration, the detector contact sense the down (up) spin state. By applying B_z , electron spins start precessing. In that case, the number of down (up) spin decreases (increases) as B_z increased. Thus, V_{NL} for the parallel and antiparallel configuration become same for large B_z . Note that the difference between parallel and antiparallel configuration with $B_z = 0$ condition is the same amplitude with the ΔV_{NL} of spin valve signal. Importantly, one can obtain spin parameters such as τ , l_{sf} and $P_{inj(det)}$. These parameters are important factors for characterization of spin injection, detection and transport properties.

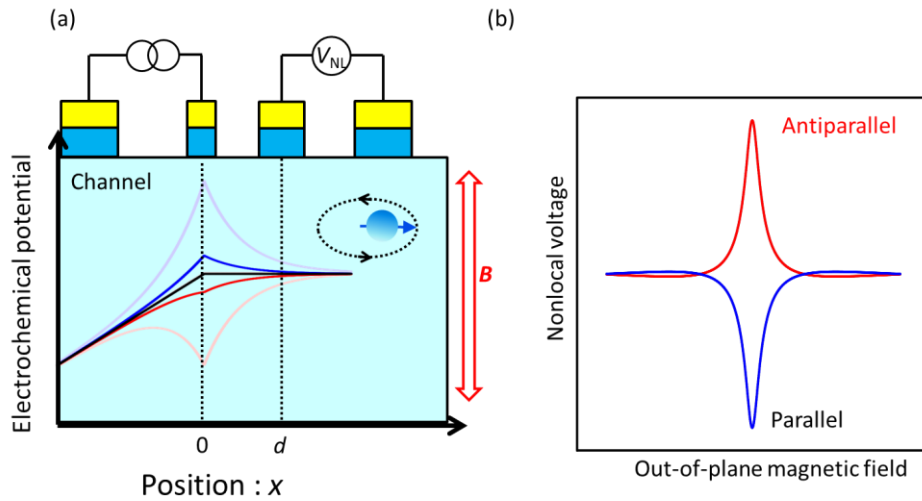


Figure 2.4. (a) Splitting of electro chemical potential for up and down spins. Due to out-of-plane magnetic field, electron spins precess, resulting in reduction of the splitting. (b) Schematic Hanle signals with parallel, antiparallel.

2.4 Spin orbit interaction

The Hamiltonian for Rashba-type SOI¹⁴ originating from structural inversion asymmetry and Dresselhaus-type SOI¹⁵ originating from bulk inversion asymmetry are given by

$$H_R = \alpha(k_y\sigma_x - k_x\sigma_y), \quad (2.8)$$

$$H_D = \beta(k_x\sigma_x - k_y\sigma_y), \quad (2.9)$$

respectively, where α and β are the effective Rashba and Dresselhaus parameters, σ_x and σ_y are Pauli spin matrices, and k_x and k_y are the electron wave vectors. Figure 2.5 shows schematics of the Rashba and Dresselhaus spin-orbit magnetic field in the k -space. Arrows in the figure corresponds to the direction and magnitude of effective SOI fields. These SOI fields are known to a spin relaxation mechanism. For example, in the Rashba SOI, electron spins with a $k = k_x$ (k_y) affects to a SOI field parallel to the k_y (k_x) direction. In a semiconductor channel, electrons move to random direction. Thus, each electron with a different k feel random effective magnetic field, resulting in the spin relaxation. Strain due to pseudomorphic growth also induces SOI given by¹⁶

$$H_{SIA} = \frac{1}{2}C_3\varepsilon_{xy}(k_y\sigma_x - k_x\sigma_y), \quad (2.10)$$

$$H_{BIA} = D(\varepsilon_{zz} - \varepsilon_{xx})(k_x\sigma_x - k_y\sigma_y), \quad (2.11)$$

where, ε_{ij} , ($i, j = x, y, z$) are the components of the strain tensor, H_{SIA} and H_{BIA} are Hamiltonian of structural-inversion-asymmetry (SIA) type strain-induced SOI and that of bulk-inversion-asymmetry (BIA) type strain-induced SOI, respectively. C_3 and D are material constants. H_{SIA} and H_{BIA} have the same form with the H_R and H_D for the k and σ , respectively.

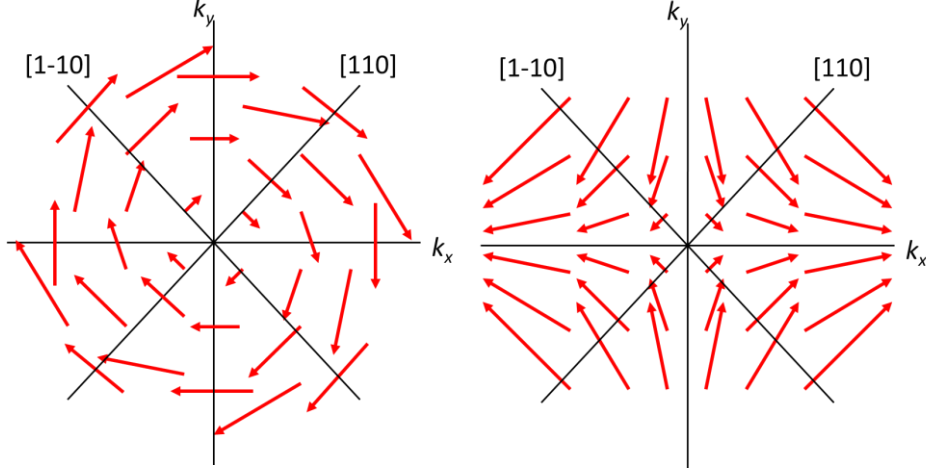


Figure 2.5. Schematics of the effective magnetic field (a) Rashba SOI and (b) Dresselhaus SOI. Thin arrows represent a vector plot of the spin orbit effective field.

SOI also affects to electron spins during the tunneling in a GaAs Schottky tunnel barrier. According to the WKB approximation, the tunneling probability T for electrons having Fermi energy E_F is given by

$$T = \exp \left[-2t \sqrt{\frac{2m}{\hbar^2} (V - E_F + \mathbf{w} \cdot \mathbf{n}) + k_x^2 + k_y^2} \right], \quad (2.12)$$

where t is tunneling barrier width, m is electron mass, V is an effective barrier height of the tunneling barrier, and \mathbf{n} is the unit vector of spin direction. $\mathbf{w} = (\alpha k_y + \beta k_x, -\alpha k_x - \beta k_y, 0)$ is the effective magnetic field induced by both Rashba SOI and Dresselhaus SOI. By expanding Eq. 2.11 as a perturbative series of $\mathbf{w} \cdot \mathbf{n}$, and integrating over \mathbf{k}_{\parallel} , the anisotropic tunnel resistance given by¹⁰

$$R(\theta) = (R_{1-10} - R_{110}) \sin^2 \theta + R_{110}, \quad (2.13)$$

is obtained. Where θ is the angle of the magnetization direction of ferromagnetic electrode with respect to the [110] direction, and R_{110} and R_{1-10} are tunnel resistances for magnetization parallel to [110] and [1-10] direction, respectively.

2.5 Electrical detection of nuclear magnetic field

2.5.1 Oblique Hanle effect

To evaluate Overhauser field, oblique Hanle effect measurements are widely used. Overhauser field in the steady state is given by¹⁷

$$\mathbf{B}_n = f_1 b_n \frac{\mathbf{B} \cdot \mathbf{S}}{\mathbf{B}^2 + \xi B_l^2} \mathbf{B}, \quad (2.14)$$

where f_1 (≤ 1) is the leakage factor, b_n is the effective field due to the polarization of nuclear spins, which takes the negative value of -17 T in GaAs for the theoretical ideal case, \mathbf{S} is the average electron spin ($|\mathbf{S}| = 1/2$ corresponds to $P_{\text{GaAs}} = 100\%$), \mathbf{B} is the external magnetic field, B_l is the local dipolar field experienced by the nuclei, and ξ is a numerical coefficient on the order of unity. Since electron spins experience the total magnetic fields of $\mathbf{B} + \mathbf{B}_n$, the condition to induce spin precession is given by $(\mathbf{B} + \mathbf{B}_n) \times \mathbf{S} \neq \mathbf{0}$. If the $\mathbf{B} \cdot \mathbf{S} = 0$ is satisfied, $\mathbf{B}_n = 0$, resulting in a conventional Hanle curve. Figure 2.6(b) shows a schematic steady-state oblique Hanle signal. \mathbf{S} is set to $\mathbf{S} = (S, 0, 0)$ and applied magnetic field is set to $\mathbf{B} = (B \sin \varphi, 0, B \cos \varphi)$, here, φ is an oblique angle with respect to the spin direction \mathbf{S} . Compared to the conventional Hanle signal, an additional side peak appears. The origin of the side peak is cancellation of external and Overhauser fields; i.e., at $B > 0$, \mathbf{B} and \mathbf{B}_n are antiparallel, and electron spins experience a smaller effective magnetic field than $|\mathbf{B}|$. When \mathbf{B}_n and \mathbf{B} cancel each other, precession of electron spins suppress and the nonlocal voltage shows a satellite peak. At $B < 0$, on the other hand, no satellite peak appears, because \mathbf{B}_n and \mathbf{B} are parallel, and no cancellation occurs. The time evolution of Overhauser field is given by

$$\mathbf{B}_n(t) = [\mathbf{B}_n(\infty) - \mathbf{B}_n(0)] \exp(-t/T_C) + \mathbf{B}_n(\infty), \quad (2.15)$$

where $\mathbf{B}_n(\infty)$ is a steady-state Overhauser field, which is given by Eq. 2.14, Since the characteristics time of T_C is several seconds or more, very slow sweeping of the external magnetic field is necessary for the steady-state oblique Hanle effect measurement.

In the transient state, the behavior of nuclear spins is different from the steady state. Figure 2.7(a) shows a schematic transient-state oblique Hanle signal. Conditions of $\mathbf{B} \cdot \mathbf{S} > 0$ for the initial state and a sweep of the magnetic field from the positive to negative

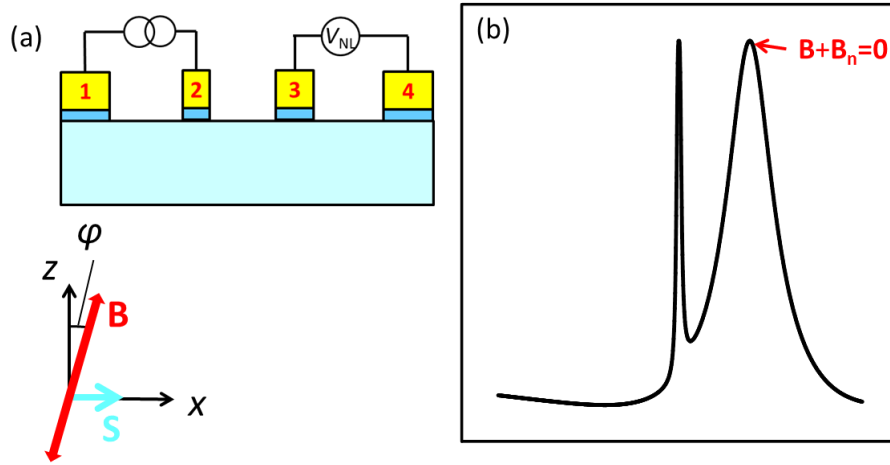


Figure 2.6. Schematics of (a) the measurement configuration for the oblique Hanle effect (b) an steady-state oblique Hanle signal. At the side peak, total magnetic field for electron is zero, resulting in no spin precession.

with a faster sweep rate than the time scale of T_C are assumed. Compared to the steady-state one, an additional side peak appears. This feature is explained as follows. Considering a two-level nuclear spin system due to the Zeeman splitting as shown in figure 2.7(b), the majority of nuclear spins is parallel to the electron spin direction due to DNP (initial state). In this case, nuclear magnetic field is antiparallel to the applied magnetic field because of negative b_n . When the sign of external magnetic field is changed, nuclear magnetic moments change their direction by 180 degree. However, the number of nuclear spins for upper and lower Zeeman energy state is unchanged immediately after the sign change of the external magnetic field (transient state). This is because the nuclear spin system has long spin-lattice relaxation time (~ 100 sec).¹⁸ After that, nuclear spins become parallel to the electron spin direction due to DNP again (steady state).

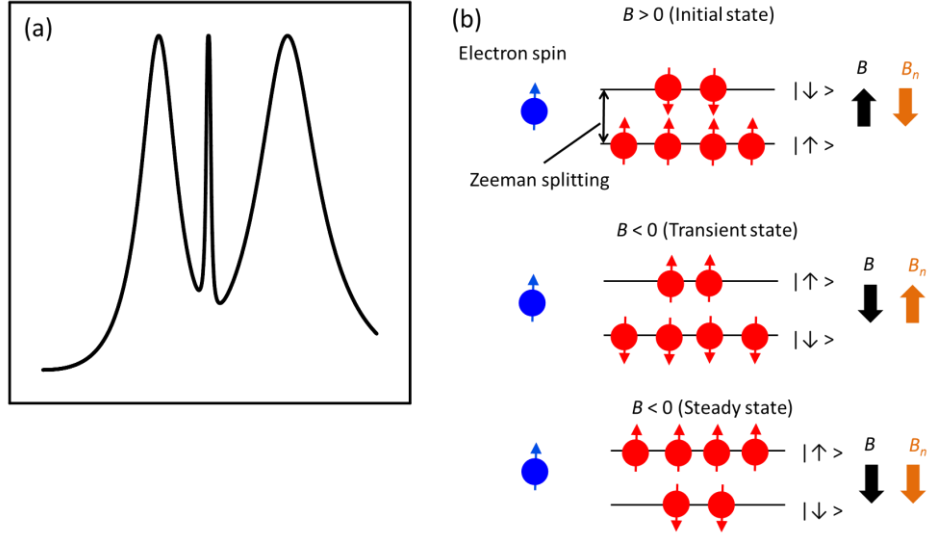


Figure 2.7. Schematic of (a) a transient-state oblique Hanle signal and (b) diagram of nuclear spin moments.

2.5.2 NMR induced oblique Hanle effect

When a Zeeman energy of nuclear spins due to a static magnetic field and an energy of irradiated rf-magnetic field are equivalent, nuclear magnetic resonance (NMR) occur. This condition is described as

$$\gamma \mathbf{B} = \omega. \quad (2.16)$$

Here, \mathbf{B} is a static magnetic field, and γ is a gyromagnetic ratio of nuclei and ω is an angular frequency of the irradiated rf-magnetic field. In GaAs, there are three kinds of nuclei ^{69}Ga , ^{71}Ga , and ^{75}As , corresponding γ values of 6.45, 8.19, and 4.60×10^7 [rad/T·sec], respectively.¹⁸ When NMR occurs, energies are absorbed and emitted between the nuclear spin system and the applied rf magnetic field. Then, reach to the thermal equilibrium state, indicating the nuclear spin polarization decreases. Figure 2.8(a) and (b) shows schematic steady-state and transient-state oblique Hanle signals with an rf magnetic field. In the case of the steady state, shape of the oblique Hanle signal is the same with the case without rf magnetic field, however, three sharp dips originating from ^{69}Ga , ^{71}Ga , and ^{75}As appear. This is because nuclear spin polarization and Overhauser field are decreased due to NMR. In the case of the transient state, three dips also appear, and the left side peak

disappears. Similar to the steady state, the origin of the three dips is due to NMR of ^{69}Ga , ^{71}Ga , and ^{75}As . The disappearance of the left side peak is also reduction of nuclear polarization due to NMR. Compare to the steady state, the effect of NMR on the transient-state oblique Hanle signal clearly can be seen.

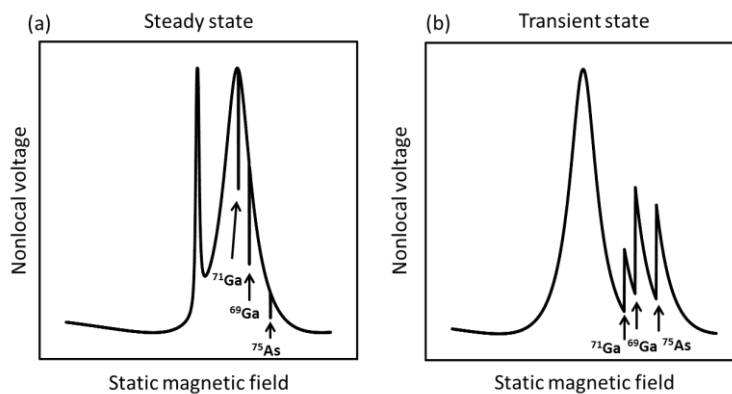


Figure 2.8. Schematics of NMR induced oblique Hanle signals (a) transient state and (b) steady state.

References

1. G. Schmidt, D. Ferrand, L. W. Molenkamp, A. T. Filip and B. J. van Wees, *Phys. Rev. B* **62**, 4790(R) (2000).
2. E. I. Rashba, *Phys. Rev. B* **62**, 16267(R) (2000).
3. A. Fert and H. Jaffrès, *Phys. Rev. B* **64**, 184420 (2001).
4. X. Lou, C. Adelman, S. A. Crooker, E. S. Garlid, J. Zhang, K. S. M. Reddy, S. D. Flexner, C. J. Palmstrøm, and P. A. Crowell, *Nat. Phys.* **3**, 197 (2007).
5. M. Johnson and R. H. Silsbee, *Phys. Rev. Lett* **55**, 1790, (1985).
6. T. Uemura, T. Akiho, M. Harada, K.-i. Matsuda, and M. Yamamoto, *Appl. Phys. Lett.* **99**, 082108 (2011).
7. T. Akiho, J. Shan, H.-x. Liu, K.-i. Matsuda, M. Yamamoto, and T. Uemura, *Phys. Rev. B*, **87**, 235205 (2013).
8. S. Datta and B. Das, *Appl. Phys. Lett.* **56**, 665 (1990).
9. S. Sugahara, M. Tanaka, *Appl. Phys. Lett.* **84**, 2307 (2004).
10. A. Matos-Abiague and J. Fabian, *Phys. Rev. B* **79**, 155303 (2009).
11. S. P. Dash, S. Sharma, R. S. Patel, M. P. de Jong, and R. Jansen, *Nature (London)* **462**, 491 (2009).
12. T. Uemura, K. Kondo, J. Fujisawa, K.-i. Matsuda, and M. Yamamoto, *Appl. Phys. Lett.* **101**, 132411 (2011).
13. J. Fabian, A. Matos-Abiague, C. Ertler, P. Stano, I. Žutić, *acta Phys. Slov.* **57**, 565 (2007).
14. E. I. Rashba, *Sov. Phys. Solid State* **2**, 1109 (1960).
15. P. D. Dresslhaus, C. M. A. Papavassiliou, R. G. Wheeler, and R. N. Sacks, *Phys. Rev. Lett.* **68**, 106 (1992).
16. B. A. Bernevig and S.-C. Zhang, *Phys. Rev. B*, **72**, 115204 (2005).
17. D. Paget, G. Lampel, B. Sapoval, and V. I. Safarov, *Phys. Rev. B* **15**, 5780 (1977).
18. J. Shiogai, M. Ciorga, M. Utz, D. Schuh, T. Arakawa, M. Kohda, K. Kobayashi, T. Ono, W. Wegscheider, D. Weiss, and J. Nitta, *Appl. Phys. Lett.* **101**, 212402 (2012).

Chapter 3

Spin injection into GaAs and development of a highly polarized spin source

Effective spin injection from a ferromagnetic electrode into a semiconductor channel is important issues for developing semiconductor-based spintronics devices such as spin transistors and nuclear spin quantum bits. In this chapter, effect of an insertion of a MgO tunnel barrier and effect of a Heusler alloy Co_2MnSi spin source on spin injection properties were investigated to demonstrate efficient spin injection. In both cases, spin injection efficiency increased compared to reference samples. In addition, tunneling anisotropic magnetoresistance (TAMR) effect on a single ferromagnet/semiconductor heterojunction was investigated, because the magnetoresistance produced by the TAMR effect might affect the spin-valve effect. A highly polarized spin source demonstrated in this chapter enables an efficient polarization of nuclear spins.

3.1 Introduction

Effective spin injection from a ferromagnet (F) into a semiconductor (SC) is of great importance for creating viable semiconductor-based spintronics devices.^{1,2} The fundamental obstacle to spin injection across an F/SC interface is the conductivity mismatch³ between a ferromagnetic metal and a SC. To solve the conductivity mismatch problem, introduction of a tunneling barrier between the F and SC has been proposed.^{4,5} One approach to introducing a tunneling barrier is to form a Schottky tunnel barrier between F and heavily doped SC. Spin injection from Fe or CoFe into GaAs through a Schottky tunnel barrier has been demonstrated using both optical⁶⁻⁸ and electrical detection.⁹⁻¹² Lou et al., demonstrated electrical spin injection in Fe/GaAs Schottky tunnel junctions through the observation of spin-valve signals and Hanle signals in a non-local configuration.⁹ The observation of both signals provides direct evidence of spin injection and transport. Salis et al., investigated the temperature dependence of the spin signal in Fe/GaAs, and reported spin injection at room temperature.¹⁰ We also achieved spin injection in Co₅₀Fe₅₀ (CoFe)/n-GaAs Schottky tunnel junctions with an improved temperature dependence.¹²

Highly spin polarized ferromagnetic material is indispensable for creating highly spin polarized states in semiconductors. Co-based Heusler alloys are one candidate for a highly-polarized spin source because of the half-metallic ferromagnetic nature theoretically predicted for many of these alloys,^{13, 14} and because of their high Curie temperatures, which are well above room temperature. There have been several reports on spin injection through spin light emitting diodes (LEDs) with Co-based Heusler alloy electrodes.^{15, 16} The reported spin injection efficiency of these devices, however, has been less than that with an Fe electrode. Moreover, there has been no report on the electrical detection of spin injection using a lateral spin transport device with a Heusler alloy electrode. Thus, the applicability of the Co-based Heusler alloy to spin injection has not been fully clarified.

Another approach to introducing a tunnel barrier is insertion of a thin insulator, such as AlO_x, GaO_x, or MgO, between the F and SC¹⁷⁻²⁴. In particular, a MgO barrier is promising because of the coherent tunneling effect.^{25, 26} Wang *et al.* achieved relatively high spin injection efficiency even at RT in a CoFe/MgO/GaAs spin-LED.²⁴ Although there are

several reports on spin injection using F/MgO/SC tunnel junctions,²¹⁻²⁴ no systematic investigation on the effect of inserting a MgO barrier by comparing identically fabricated junctions with or without a MgO barrier has been done.

The purpose of this study is to demonstrate effective spin injection into GaAs. For that purpose, first, the effect of an insertion of an epitaxial MgO tunnel barrier between a ferromagnetic layer and a semiconductor, i.e., we investigated the spin dependent injection properties of CoFe/MgO/n-GaAs junctions. Second, spin injection properties with a Heusler alloy Co₂MnSi in Co₂MnSi/CoFe/n-GaAs junctions. This chapter is organized as follows. Section 3.2 describes experimental method. Section 3.3 describes investigation of the effect of MgO barrier insertion on the non-local spin-valve effect for CoFe/n-GaAs samples with and without MgO barrier for the same semiconductor structures. In addition to the non-local spin-valve effect, we investigated the tunneling anisotropic magnetoresistance (TAMR) effect,^{27,28} because the magnetoresistance produced by the TAMR effect might affect the spin-valve effect. In section 3.4, we discuss the effect of MgO barrier insertion on spin-valve signals and TAMR signal. In section 3.5, using a Heusler alloy Co₂MnSi spin source, we demonstrate all electrical injection and detection of spin-polarized electrons through the observation of spin-valve signals and Hanle signals in a four-terminal nonlocal geometry. In Section 3.6, we discuss the spin-injection efficiency of the Co₂MnSi electrode from a comparison of the bias voltage-dependent spin polarization between Co₂MnSi/CoFe/n-GaAs and CoFe/n-GaAs samples. In Section 3.7, the summary of this chapter is described.

3.2 Experimental methods

Layer structures consisting of (from the substrate side) a 250-nm-thick undoped GaAs buffer layer, a 2500-nm-thick n⁻-GaAs channel layer, a 15-nm-thick n⁻→n⁺-GaAs transition layer, and a 15-nm-thick n⁺-GaAs layer were grown by molecular beam epitaxy at 590 °C on GaAs (001) substrates. The doping concentration of the n⁻-GaAs channel was chosen to be $3 \times 10^{16} \text{ cm}^{-3}$, and the doping concentration of the n⁺-GaAs was $5 \times 10^{18} \text{ cm}^{-3}$ to form a narrow Schottky barrier. The samples were then capped with an arsenic protective layer and transported in air to an ultrahigh vacuum chamber capable of combined magnetron sputtering and electron beam evaporation with a base pressure of

about 6×10^{-8} Pa. The arsenic cap was removed by heating the samples to 300–400°C in a preparation chamber. Four different kinds of spin source layers were deposited on the GaAs samples as shown in figure 3.1(a) and (b). First, a 0.8-nm-thick MgO layer was grown by electron-beam evaporation at 350°C with a deposition rate of 0.01 nm/s. Then, a 5-nm-thick CoFe layer was deposited by magnetron sputtering at RT. No post-deposition annealing was carried out. Second, a 1.1-nm-thick CoFe layer and a 5-nm-thick Co₂MnSi layer were deposited on the GaAs substrate by magnetron sputtering at room temperature and successively annealed *in situ* at 350°C. The film composition of the Co₂MnSi film was chosen to be Co₂Mn_{1.3}Si_{0.9} to suppress harmful Co_{Mn} antisites.^{29, 30} Third and fourth, samples with a 5-nm-thick CoFe single layer were prepared as a reference. The third sample was not annealed for the comparison with the CoFe/MgO/n-GaAs sample, and the fourth sample was annealed *in situ* at 350°C for the comparison with the Co₂MnSi/CoFe/n-GaAs sample.

Using electron beam (EB) lithography and Ar ion milling techniques, lateral spin transport devices as shown in Fig. 3.1(c) were fabricated. The size of the injector contact (contact-2) and detector contact (contact-3) were $0.5 \times 10 \mu\text{m}$ and $1.0 \times 10 \mu\text{m}$, respectively, and the spacing (d) between them was 0.5 or 4.0 μm . We defined the longer (shorter) direction of the junction as the y -axis which (x -axis) direction. The bias voltage was defined with respect to the n-GaAs.

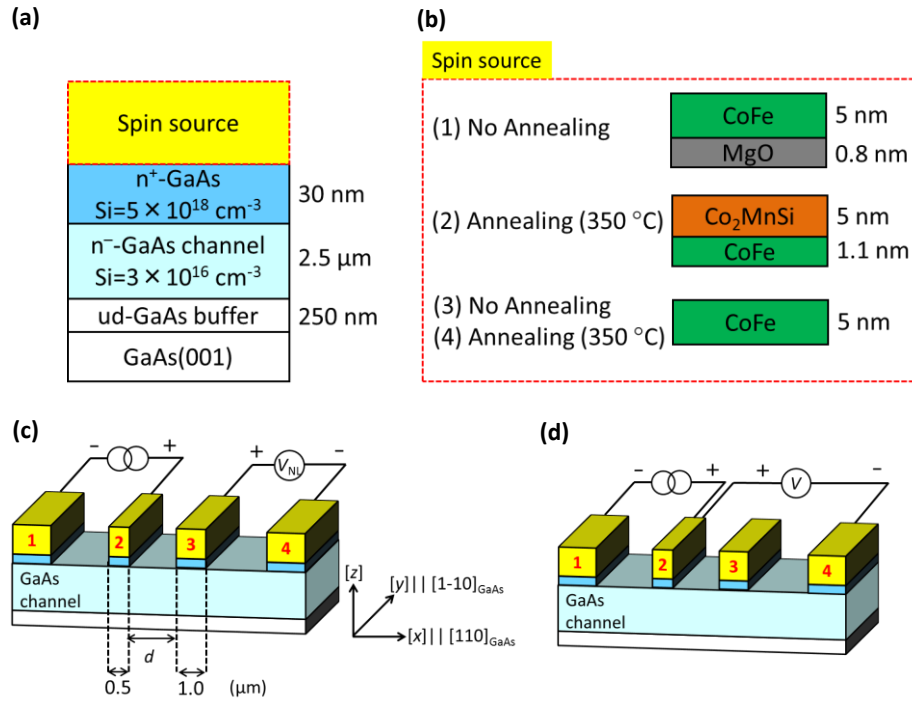


Fig. 3.1. (a) Sample layer structures and (b) Layer structure of spin source. GaAs layers were grown by MBE at 580-600 °C. Four kinds of spin sources were deposited on the same semiconductor structures. (1) CoFe/MgO/n-GaAs without annealing, (2) Co₂MnSi/CoFe/n-GaAs annealed at 350 °C, (3) CoFe/n-GaAs without annealing to compare with (1), and CoFe/n-GaAs annealed at 350 °C to compare with (2). (c) Schematic device structure of a four-terminal lateral spin-transport device and circuit configuration for nonlocal measurements. (d) Circuit configuration for measuring the TAMR effect.

3.3 Experimental results

3.3.1 Structural properties of CoFe/MgO/n-GaAs

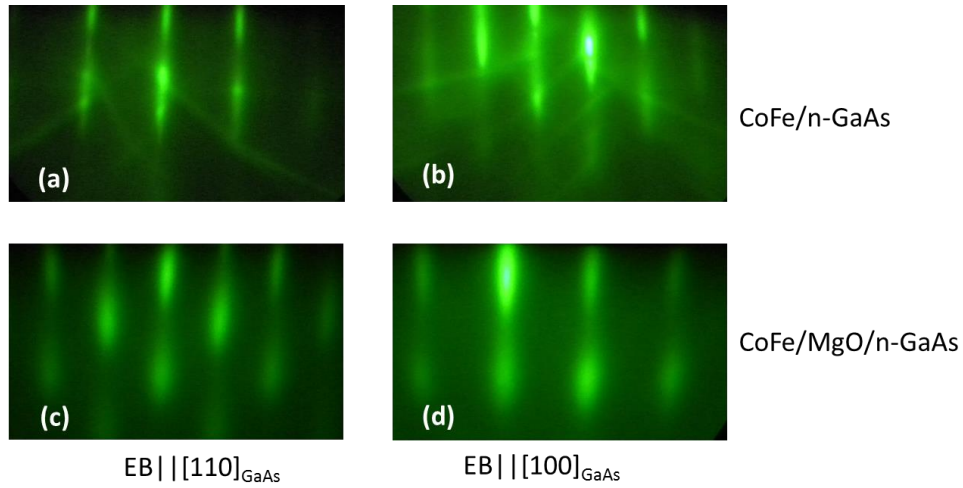


Fig. 3.2. RHEED patterns along the azimuths of $[110]_{\text{GaAs}}$ and $[100]_{\text{GaAs}}$ for CoFe/GaAs and CoFe/MgO/GaAs. (a) CoFe/GaAs with EB|| $[110]_{\text{GaAs}}$, (b) CoFe/GaAs with EB|| $[100]_{\text{GaAs}}$, (c) CoFe/MgO/GaAs with EB|| $[110]_{\text{GaAs}}$, and (d) CoFe/MgO/GaAs with EB|| $[100]_{\text{GaAs}}$.

Figures 3.2(a)-(d) show reflection high-energy electron diffraction (RHEED) patterns of the CoFe layers along two different azimuths $[110]_{\text{GaAs}}$ and $[100]_{\text{GaAs}}$ for CoFe/n-GaAs and CoFe/MgO/n-GaAs. The streak RHEED patterns indicate that the CoFe layers grew epitaxially on the n-GaAs or on the MgO/n-GaAs, although slightly spotty patterns which indicate a three-dimensional growth were observed for the CoFe layer on the MgO/n-GaAs. Note that the RHEED patterns shown in Figs. 3.2(a) and (d) are identical to that observed for CoFe along an azimuth of $[110]_{\text{CoFe}}$, and those shown in Figs. 3.2(b) and (c) are identical to that along an azimuth of $[100]_{\text{CoFe}}$. Thus, the crystallographic relationship was $\text{CoFe}(001)[110] \parallel \text{GaAs}(001)[110]$ (CoFe and GaAs were cube-on-cube) for CoFe/n-GaAs, and $\text{CoFe}(001)[110] \parallel \text{MgO}(001)[100] \parallel \text{GaAs}(001)[100]$ (the CoFe film was rotated by 45° in the (001) plane with respect to GaAs and MgO) for CoFe/MgO/n-GaAs.

3.3.2 Effect of MgO barrier insertion on junction resistance and TAMR characteristics

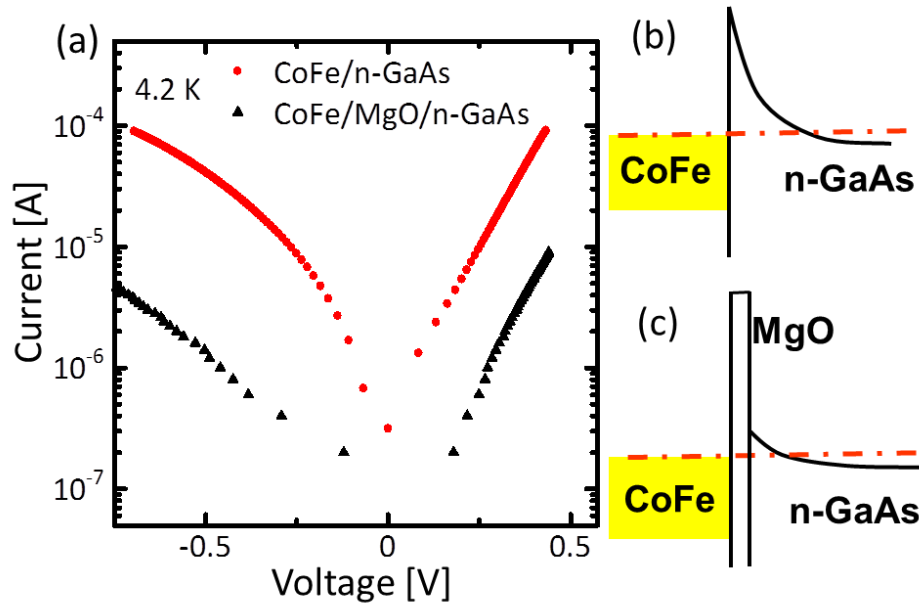


Fig. 3.3. (a) I - V characteristics measured at 4.2K for CoFe/n-GaAs single junctions with and without a MgO barrier. Both curves show non-linear and almost symmetric behavior with respect to the bias voltage polarity due to electron tunneling through a Schottky barrier for the CoFe/n-GaAs and a MgO barrier for the CoFe/MgO/n-GaAs junction. (b), (c) Schematic band diagrams for (b) CoFe/n-GaAs Schottky tunnel junction and (c) CoFe/MgO/n-GaAs tunnel junction.

Figure 3.3(a) shows the I - V characteristics for CoFe/n-GaAs single junctions measured at 4.2 K with and without a MgO barrier. The curves for both samples exhibited non-linear characteristics and were almost symmetric with respect to the bias polarity due to the tunneling of electrons through a Schottky barrier for the CoFe/n-GaAs (Fig. 3.3(b)) and through a MgO barrier for CoFe/MgO/n-GaAs samples (Fig. 3.3(c)). The junction resistance of the CoFe/MgO/n-GaAs was more than one order of magnitude larger than that of the CoFe/n-GaAs sample.

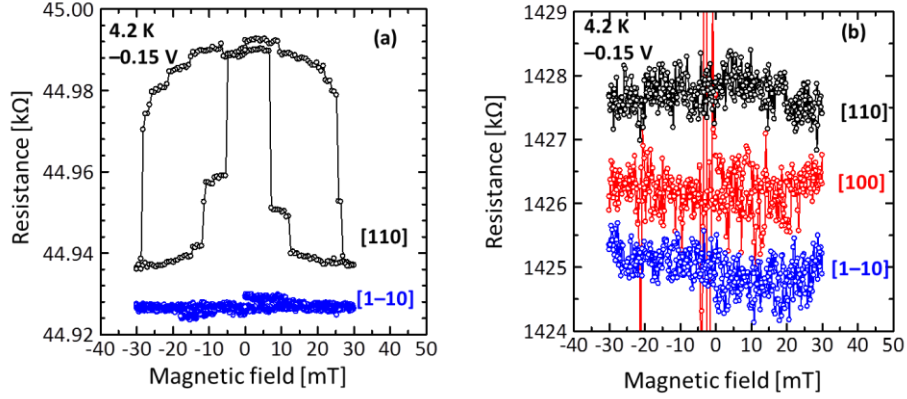


Fig. 3.4. MR curves measured at 4.2K for CoFe/n-GaAs single junctions (a) without a MgO barrier and (b) with a MgO barrier. An in-plane magnetic field was applied along (a) $[110]_{\text{GaAs}}$ and $[1-10]_{\text{GaAs}}$, and (b) $[110]_{\text{GaAs}}$, $[100]_{\text{GaAs}}$, and $[1-10]_{\text{GaAs}}$, respectively. The curve for $[1-10]_{\text{GaAs}}$ has an offset of -320Ω in (a) and curves for $[110]_{\text{GaAs}}$ and $[1-10]_{\text{GaAs}}$ have offsets of 2 and $-2 \text{ k}\Omega$ in (b), respectively.

Figures 3.4(a) and 3.4(b) show magnetoresistance (MR) curves measured at 4.2 K for CoFe/n-GaAs single junctions with and without a MgO barrier (MgO-inserted CoFe/MgO/n-GaAs junction and CoFe/n-GaAs junction). The voltage drop across the junction was -0.15 V , and the in-plane magnetic field (B) was applied along the $[110]_{\text{GaAs}}$ and $[1-10]_{\text{GaAs}}$ directions for CoFe/n-GaAs (Fig. 3.4(a)), and along the $[110]_{\text{GaAs}}$, $[100]_{\text{GaAs}}$, and $[1-10]_{\text{GaAs}}$ directions for CoFe/MgO/n-GaAs (Fig. 3.4(b)). The curve for $[1-10]_{\text{GaAs}}$ has an offset of -320Ω in Fig. 3.4(a) and curves for $[110]_{\text{GaAs}}$ and $[1-10]_{\text{GaAs}}$ have offsets of 2 and $-2 \text{ k}\Omega$ in Fig. 3.4(b), respectively. The samples without a MgO barrier showed clear MR when B was swept along the $[110]_{\text{GaAs}}$ direction, which corresponds to the hard axis direction for the shape anisotropy. We previously observed a TAMR effect in CoFe/n-GaAs^{31, 32} and $\text{Co}_2\text{MnSi/n-GaAs}$ ³³ Schottky tunnel junctions, and found that the TAMR effect produced a resistance difference between R_{110} and R_{1-10} , where R_{110} and R_{1-10} stand for the tunnel resistances when the magnetization (M) of CoFe is oriented along $[110]_{\text{GaAs}}$ and $[1-10]$, respectively. The angular dependence of the tunnel resistance was given by³¹⁻³³

$$R(\theta) = (R_{1-10} - R_{110}) \sin^2 \theta + R_{110}, \quad (3.1)$$

where θ is the angle of the magnetization direction of the CoFe electrode with respect to the $[110]_{\text{GaAs}}$ direction. The MR curves shown in Fig. 3.5(a) can be explained with the TAMR effect as follows. For $B \parallel [110]_{\text{GaAs}}$, the magnetization (M) of CoFe would have oriented to the $[1-10]_{\text{GaAs}}$ direction at small $|B|$ since the $[110]_{\text{GaAs}}$ direction corresponds to the hard axis direction for the shape anisotropy of the junction, resulting in the junction resistance of R_{1-10} ; however, it would have oriented to the $[110]_{\text{GaAs}}$ direction at large $|B|$, resulting in the junction resistance of R_{110} . For $B \parallel [1-10]_{\text{GaAs}}$, on the other hand, since the $[1-10]_{\text{GaAs}}$ direction is an easy axis, there was no state for $M \parallel [110]$ when the magnetic field was swept along the $[1-10]$ direction, resulting in almost constant junction resistance corresponding to R_{1-10} for all values of B investigated. This anisotropic tunnel resistance produced a spin-valve-like MR, as shown in Fig. 3.5(a), even in a single junction. Thus, TAMR may affect the electrical detection of spin injection when F/SC heterojunctions are used.

In the case of CoFe/MgO/n-GaAs, no significant MR was observed for any of the three directions ($[110]$, $[100]$, and $[1-10]$) of the magnetic field. This result indicates that the insertion of a MgO barrier between CoFe and GaAs suppressed the TAMR effect. A possible mechanism of the suppression will be discussed in section 3.4.1.

3.3.3 Effect of MgO barrier insertion on non-local spin valve effect

Figure 3.5 plots non-local voltage (V_{NL}) measured at 4.2 K as a function of the magnetic field along the $[1-10]$ direction in a four-terminal device consisting of (a) CoFe/n-GaAs Schottky tunnel junctions and (b) CoFe/MgO/n-GaAs tunnel junctions. The non-local voltage was measured between contact-3 and contact-4, while constant current (I) of $-30 \mu\text{A}$ (Fig. 3.5(a)) or $-1 \mu\text{A}$ (Fig. 3.5(b)) was supplied between contact-1 and contact-2. Under this bias condition, electrons tunnel from CoFe into GaAs. The voltage drop across the junction under injector contact-2 was -0.44 V for both samples. Both samples showed

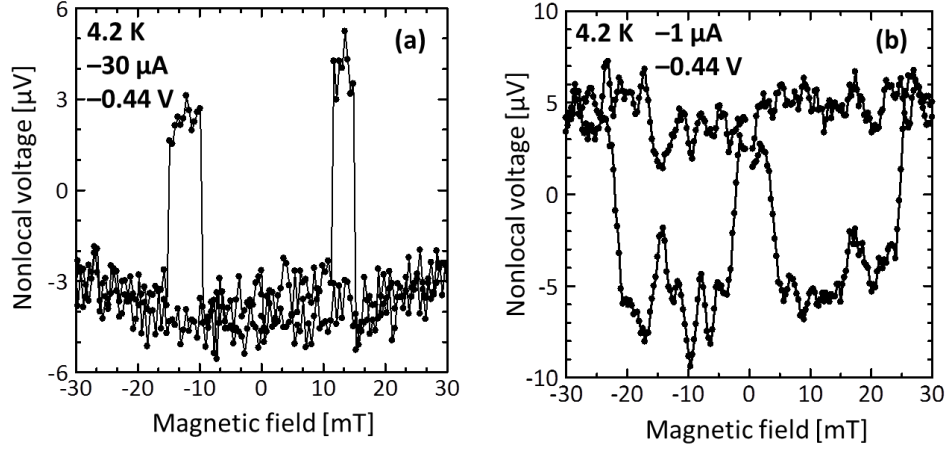


Fig. 3.5. Plots of non-local voltage at 4.2 K as a function of the in-plane magnetic field ($B||[1-10]$) (a) CoFe/n-GaAs Schottky tunnel junctions and (b) CoFe/MgO/n-GaAs tunnel junctions.

a clear spin-valve-like signal. As shown in Figs. 3.4(a) and (b), no significant MR was observed for a CoFe/n-GaAs single junction or a CoFe/MgO/n-GaAs single junction when the magnetic field was swept along the $[1-10]$ direction. Thus, the observed non-local spin-valve-like signal was due to the parallel (P)/anti-parallel (AP) switching in magnetization configuration between the injector contact and the detector contact, indicating the injection, transport, and detection of spin-polarized electrons for both samples.

The non-local voltage change (ΔV_{NL}) was approximately $8 \mu\text{V}$ for CoFe/n-GaAs and $-10 \mu\text{V}$ for CoFe/MgO/n-GaAs. Here, ΔV_{NL} was defined by $V_{NL}^{AP} - V_{NL}^P$, where V_{NL}^{AP} and V_{NL}^P are non-local voltages for AP and P configurations, respectively, between injector contact-2 and detector contact-3. Interestingly, the magnitude of $\Delta V_{NL}/I$ for CoFe/MgO/n-GaAs increased by a factor of 38 compared with that of CoFe/n-GaAs. Moreover, the sign of the ΔV_{NL} was opposite between the samples with and without a MgO barrier.

3.4. Discussion

3.4.1 Effect of MgO barrier insertion on TAMR characteristics

We will first discuss suppression of the TAMR effect through the insertion of a MgO barrier. Recently, Matos and Fabian proposed a theoretical model³⁴ based on the Rashba-type spin orbit interaction (SOI) at the F/SC heterointerface and the Dresselhaus-type SOI inside the GaAs Schottky tunnel barrier to explain the effect of TAMR observed in Fe/i-GaAs/Au.²⁸ Our previous experimental results on the bias voltage dependence and the influence of the GaAs surface structure on TAMR observed in CoFe/n-GaAs and Co₂MnSi/n-GaAs Schottky tunnel junctions support their SOI-based model.³¹⁻³³ We will briefly summarize the consequences of Rashba and Dresselhaus terms on the tunneling probability at a ferromagnet/n-GaAs junction. The Hamiltonian for both Rashba and Dresselhaus SOIs is given by

$$H_{\text{SO}} = \alpha(\sigma_x k_y - \sigma_y k_x) + \beta(\sigma_x k_x - \sigma_y k_y) \equiv \mathbf{w}(\mathbf{k}_{\parallel}) \cdot \boldsymbol{\sigma}, \quad (3.2)$$

where α and β are the effective Rashba and Dresselhaus parameters, $\boldsymbol{\sigma} = (\sigma_x, \sigma_y, \sigma_z)$ is the Pauli spin matrix, $\mathbf{k}_{\parallel} = (k_x, k_y)$ is the in-plane wave vector, and \mathbf{w} is the SOI-induced effective magnetic field. Here, the x -axis and y -axis are respectively set to the [100] and [010] directions, and the z -axis is set to the tunneling direction. Rashba-type SOI results from the structural inversion asymmetry at the interface,³⁵ and Dresselhaus-type SOI results from the bulk inversion asymmetry in GaAs.³⁶ For simplicity, we approximate the Schottky barrier formed at the ferromagnet/n-GaAs interface as a single tunneling barrier with an effective barrier height of V_0 . Then, according to the WKB approximation the tunneling probability for electrons having Fermi energy (E_F) is given by

$$T = \exp \left[-2t \sqrt{\frac{2m}{\hbar^2} (V_0 - E_F + \mathbf{w} \cdot \mathbf{n}) + (k_x^2 + k_y^2)} \right], \quad (3.3)$$

where t is tunneling barrier thickness, m is electron mass, \hbar is the Plank constant divided by 2π , and \mathbf{n} is the unit vector of spin direction. Because of the anisotropy of \mathbf{w} in the (k_x, k_y) space, the tunneling probability of an electron depends on its initial spin orientation, \mathbf{n} . By expanding Eq. (3.3) as a perturbative series of $\mathbf{w} \cdot \mathbf{n}$, and integrating over \mathbf{k}_{\parallel} to get the tunnel resistance, the anisotropic tunnel resistance given by Eq. (3.1) is obtained. Since

$R_{110} - R_{1-10}$ is proportional to the product of α and β , the TAMR is eliminated when either α or β becomes zero. In the case of the CoFe/n-GaAs junction, the Schottky barrier is formed because of Fermi level pinning at the interface, and electrons tunnel through the Schottky barrier of GaAs, as shown in Fig. 3.3(b). These electrons feel both Rashba-type and Dresselhaus-type SOI fields during tunneling, resulting in the appearance of TAMR. In the case of a CoFe/MgO/n-GaAs junction, on the other hand, the GaAs Schottky barrier height would be lowered due to depinning of the Fermi level,³⁷ and electrons do not tunnel through the Schottky barrier of GaAs, but tunnel through only the MgO barrier, as shown in Fig. 3.3(c). Since the effective Dresselhaus parameter of β becomes zero inside a MgO barrier, the TMAR would be suppressed. This Fermi level depinning model is supported by our previous experimental findings on the MgO thickness dependence of the junction resistance in Co₂MnSi/MgO/n-GaAs.³⁸

3.4.2 Effect of MgO barrier insertion on non-local spin-valve effect

In the section 3.3.3, we experimentally observed the enhancement and sign reversal of $\Delta V_{NL}/I$ when a MgO barrier was inserted. The theoretical expression of $\Delta V_{NL}/I$ in the case of tunnel contact is given by³⁹

$$\frac{\Delta V_{NL}}{I} = -P_{inj} P_{det} \left(\rho \frac{l_{sf}}{S} \right) \exp \left(-\frac{d}{l_{sf}} \right), \quad (3.4)$$

where $P_{inj(det)}$ is spin polarization of the injector (detector) contact, ρ is resistivity of the GaAs channel, S is the area of the channel cross-section, l_{sf} is the spin-diffusion length, and d is the distance between contact-2 and contact-3. Since the channel structure of GaAs was the same for both samples, ρ , S , l_{sf} , and d were the same. Therefore, the difference in $\Delta V_{NL}/I$ between CoFe/n-GaAs and CoFe/MgO/n-GaAs samples comes from the difference in $P_{inj} P_{det}$.

First, we will discuss the sign change of $P_{inj} P_{det}$ when a MgO barrier was inserted. The sign of $P_{inj} \cdot P_{det}$ was positive for CoFe/n-GaAs samples and negative for CoFe/MgO/n-GaAs samples at $V_{inj} = -0.44$ V for both samples, where V_{inj} is the voltage

drop across the injector contact. Recently, change in the sign of $P_{\text{inj}}P_{\text{det}}$ depending on the bias voltage was reported for Fe/n-GaAs^{9, 10} and CoFe/n-GaAs junctions.^{11, 12} To explain the negative spin polarization observed in Fe/n-GaAs junctions, several models have been proposed: Dery and Sham suggested that the reversal of spin polarization is due to localized states in the semiconductor formed by inhomogeneous doping.⁴⁰ Chantis *et al.* predicted by first-principle calculations that negative polarization under the spin extraction mode could be explained by enhancement of the transmission coefficient of a minority-spin state through a resonant state at the Fe/GaAs interface.⁴¹ Furthermore, Honda *et al.* theoretically investigated the influence of the Schottky barrier height on spin polarization of an Fe/n-GaAs interface, and showed that the spin polarization can be negative for a wide bias voltage range, depending on the Schottky barrier height.⁴² We observed the sign change of $P_{\text{inj}}P_{\text{det}}$ in spite that the bias voltage condition was the same for both samples. This indicates that the spin-dependent electronic states for CoFe/MgO/n-GaAs samples were quite different from those for CoFe/n-GaAs samples. The spin polarization at the CoFe/MgO interface in CoFe/MgO/n-GaAs heterojunctions should be positive when we take into account the tunnel magnetoresistance characteristics of CoFe/MgO/CoFe magnetic tunnel junctions.⁴³ Thus, the spin polarization at the MgO/n-GaAs interface in CoFe/MgO/n-GaAs heterojunctions probably plays a critical role for determining the sign of $P_{\text{inj}}P_{\text{det}}$.

Next, we will discuss the enhancement of $|\Delta V_{\text{NL}}/I|$ or $P_{\text{inj}}P_{\text{det}}$ by a factor of 38 upon MgO barrier insertion. There are several possibilities regarding spin polarization enhancement. One is an increase in the junction resistance compared with CoFe/n-GaAs. Fert and Jaffrès showed that the junction resistance (R_{b}) should be much higher than $\rho l_{\text{sf}}/S$ to solve the conductivity-mismatch problem.⁵ However, this condition was satisfied even for the CoFe/n-GaAs sample.¹² Thus, the increase in R_{b} cannot explain the enhancement of $\Delta V_{\text{NL}}/I$.

A second possibility is the effect of coherent tunneling.^{26, 27} In this model, highly spin polarized Δ_1 band electrons selectively tunnel through a MgO barrier. A third possibility is that enhancement of the spin signal is due to tunneling through a localized state formed in the vicinity of the MgO/GaAs interface. Tran *et al.* observed an increase in the spin accumulation signal, well above theoretical predictions, using Co/Al₂O₃/GaAs junctions in a three-terminal Hanle geometry, and proposed a two-step tunneling model in which a sequential tunneling process via localized states located in the vicinity of the Al₂O₃/GaAs

interface enhanced the spin accumulation.¹⁹ A similar mechanism might appear in CoFe/MgO/n-GaAs samples. However, both the coherent tunneling model and the two-step tunneling model cannot explain the negative spin polarization. To clarify the origin of the sign change and enhanced spin polarization consistently, further experimental and theoretical investigations are therefore necessary.

3.5 Experimental results for Co₂MnSi/CoFe/n-GaAs

3.5.1 Structural properties of Co₂MnSi/CoFe/n-GaAs

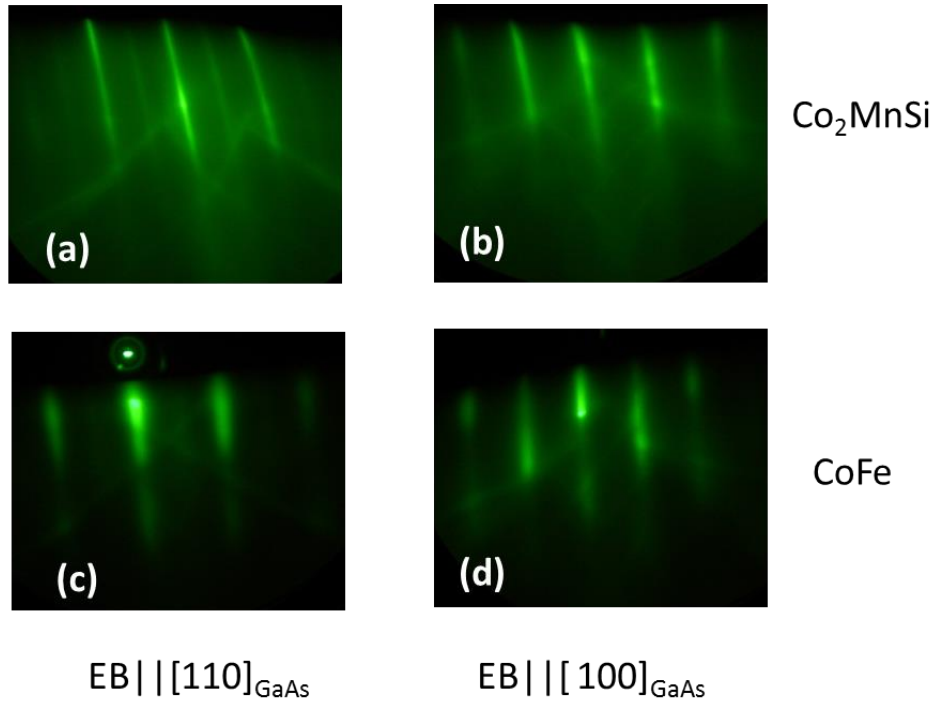


Fig. 3.6. RHEED patterns along the azimuths of $[110]_{\text{GaAs}}$ and $[100]_{\text{GaAs}}$ for the Co₂MnSi layer and the CoFe insertion layer. (a) Co₂MnSi with EB|| $[110]_{\text{GaAs}}$, (b) Co₂MnSi with EB|| $[100]_{\text{GaAs}}$, (c) CoFe with EB|| $[110]_{\text{GaAs}}$, and (d) CoFe with EB|| $[100]_{\text{GaAs}}$.

Figures 3.6(a)-(d) shows reflection high energy electron diffraction (RHEED) patterns observed *in situ* for each layer during preparation indicated that both a 1.1-nm-thick CoFe and a 5-nm-thick Co₂MnSi layers grew on GaAs. Sharp streak patterns dependent on the electron injection direction, parallel to $[110]_{\text{GaAs}}$ or $[100]_{\text{GaAs}}$, were obtained for each successive layer. Furthermore, the spacing of the observed streak patterns of the Co₂MnSi and CoFe layers agreed well with each other, indicating that the Co₂MnSi and CoFe layers grew epitaxially on GaAs. The crystallographic relationship was $\text{Co}_2\text{MnSi}(001)[110] \parallel$

CoFe(001)[110] || GaAs(001)[110] (Co₂MnSi, CoFe and GaAs were cube-on-cube) for relation.

3.5.2 TAMR effect for Co₂MnSi/CoFe/n-GaAs

Figure 3.7 shows results of TAMR effect for the Co₂MnSi/CoFe/GaAs injector contact. We found that the easy axis of the magnetization of the Co₂MnSi/CoFe bilayer was along the shorter direction of the junction (the x -axis direction or [110]_{GaAs}). This is because strong uniaxial-type magnetocrystalline anisotropy along the x -axis direction and relatively weak shape anisotropy along the y -axis direction were induced in the Co₂MnSi/CoFe bilayer. There have been several reports that ferromagnetic thin films, including Co-based Heusler alloys, epitaxially grown on GaAs(001) substrates have an uniaxial-type anisotropy with an easy axis of either the [110]_{GaAs} or [1-10]_{GaAs} direction and whose strength and direction depend on the surface reconstruction superstructures of GaAs and/or ferromagnet materials.^{44, 45} In this study, the fabricated Co₂MnSi/CoFe/n-GaAs junction had an easy axis of the [110]_{GaAs} direction, which corresponded to the x -axis direction. On the other hand, the annealed CoFe/n-GaAs junction of the reference sample had an easy axis of the [1-10]_{GaAs} direction, which corresponded to the y -axis direction.

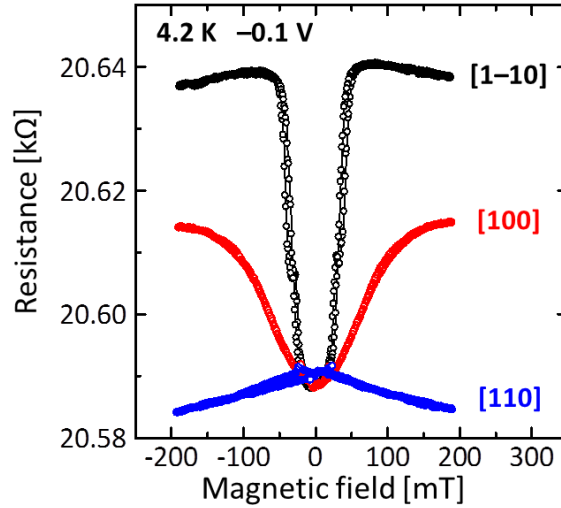


Fig. 3.7. MR curves measured at 4.2K for $\text{Co}_2\text{MnSi}/\text{CoFe}/\text{n-GaAs}$ single junctions. An in-plane magnetic field was applied along [110], [100], and [1-10] of GaAs, respectively.

3.5.3 All electrical injection and detection of spin-polarized electrons through the observation of spin-valve signals and Hanle signals

Figure 3.8 shows a plot of non-local voltage as a function of the in-plane magnetic field (B_x) for a lateral spin transport device with $\text{Co}_2\text{MnSi}/\text{CoFe}/\text{n-GaAs}$ Schottky tunnel junctions. The magnetic field was applied along the x -axis direction, which corresponded to the easy axis for the magnetization of the $\text{Co}_2\text{MnSi}/\text{CoFe}$ bilayer. A bias current (I) of $-40 \mu\text{A}$ was supplied, where electron spins were injected from the Co_2MnSi to n-GaAs . We subtracted a background signal consisting of a constant term and linear and quadratic terms of B_x so that the non-local voltage at $B_x = 0$ was set to 0 V because electron spins are completely depolarized at $B_x = 0$ due to precession by the Overhauser field.^{46, 47} Although a similar background signal was observed in the same experiment,^{9, 12} its origin is still not

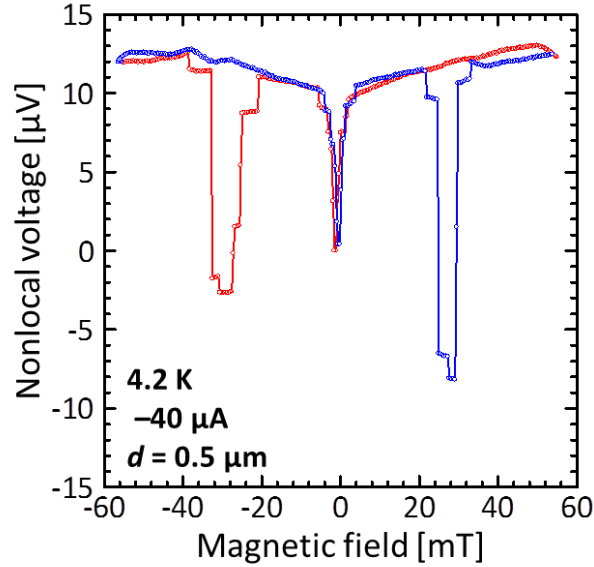


Fig. 3.8. Plot of non-local voltage as a function of in-plane magnetic field (B_x) for a lateral spin transport device with $\text{Co}_2\text{MnSi}/\text{CoFe}/\text{n-GaAs}$ junctions. A background signal consisting of a constant term and linear and quadratic terms of B_x has been subtracted.

well understood. A clear spin-valve-like change of the non-local voltage was observed at $B_x \cong +25$ mT and -30 mT due to switching between the parallel (P) and anti-parallel (AP) states for the magnetization configuration between the injector and detector contacts. However, a number of small steps were seen in the observed spin-valve signal. Furthermore, the magnetic field range for the AP state was relatively narrow, and $|V_{\text{AP}}|$ was smaller than $|V_{\text{P}}|$, suggesting an imperfect formation of the AP state. A possible origin of the small steps in the spin-valve signal and the imperfect formation of the AP state is a complex magnetization reversal arising from a conflict in the magnetic anisotropy between the shape anisotropy having the easy axis along the y -axis direction and the magnetocrystalline anisotropy having the easy axis along the x -axis direction.

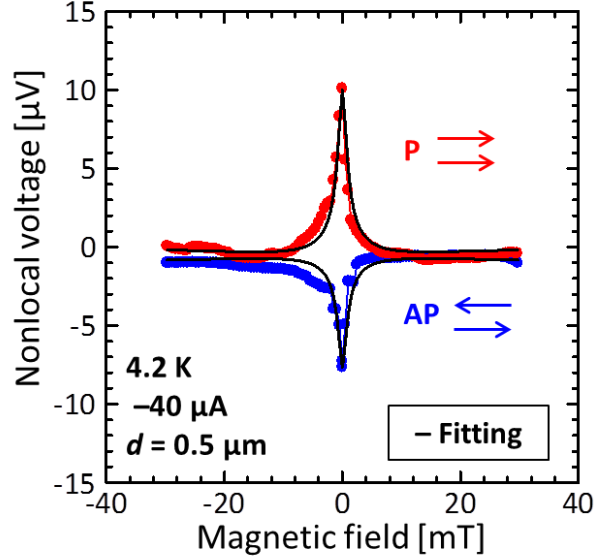


Fig. 3.9. Plot of non-local voltage as a function of out-of-plane magnetic field (B_z) for a $\text{Co}_2\text{MnSi}/\text{CoFe}/\text{n-GaAs}$ sample for both P (upper curve) and AP (lower curve) configurations. The solid lines are the result of the fitting using Eq. 3.5.

Figure 3.9 shows a plot of non-local voltage as a function of out-of-plane magnetic field (B_z) for both the P and AP configurations. The non-local voltage for the P (AP) configuration gradually decreased (increased) as $|B_z|$ increased and the two curves merged at a large B_z . These results clearly indicate the Hanle effect. In the Hanle effect, the non-local voltage as a function of B_z can be expressed by³⁹

$$V_{NL}(B_z) = \pm P_{inj} \cdot P_{det} \left(\frac{\rho l_{SF}}{S} \right) \left(\frac{l_{SF}}{\tau_{SF}} \right) I \int_0^{\infty} \frac{1}{\sqrt{4\pi Dt}} \exp\left(-\frac{d^2}{4Dt}\right) \cos(\omega_L t) \exp\left(-\frac{t}{\tau_{SF}}\right) dt, \quad (3.5)$$

where $P_{inj(det)}$ is the spin polarization of the injector (detector) contact, ρ is the resistivity of the GaAs channel, S is the area of the channel cross-section, l_{SF} is the spin-diffusion length, d is the distance between contact-2 and contact-3, τ_{SF} is the spin lifetime, I is the injected current, $D = l_{SF}^2 / \tau_{SF}$ is the diffusion constant, $\omega_L = g\mu_B B / \hbar$ is the Larmor frequency, g ($= -0.44$) is an electron g factor for GaAs, μ_B is the Bohr magneton, and \hbar is the reduced Planck's constant. The $+$ ($-$) sign on the right-hand side of Eq. 3.5 corresponds to the P (AP) configuration. The observed Hanle curves can be fitted well with Eq. 3.5. The

estimated spin lifetime τ_{SF} was 50 ns. This value of the spin lifetime is comparable to those obtained for GaAs with a doping concentration of 10^{16}cm^{-3} ,⁴⁷ suggesting that spins were injected into the GaAs channel. The estimated spin diffusion length l_{SF} was 5 μm . The Hanle signal for the P state was approximately 10 μV , and that for the AP state was approximately 8 μV , so the total of both signals was approximately 18 μV . This value agrees with the result of the spin-valve effect. The smaller amplitude of the Hanle curve for the AP state was due to the imperfect formation of the AP state, as previously described. The observation of the spin-valve signal and Hanle signal in the four-terminal non-local geometry provides direct evidence of the spin injection, detection and transport in GaAs.

3.6 Comparison of spin polarization between Co_2MnSi and CoFe

In this section, we compare the magnitude of the spin signal ($|V_P|$) and spin polarization between the sample with a Co_2MnSi electrode and that with a CoFe electrode. Figure 3.10 shows the bias-current dependence of $|V_P|$ for both a $\text{Co}_2\text{MnSi}/\text{CoFe}/\text{n-GaAs}$ sample and an annealed CoFe/n-GaAs sample. The negative (positive) bias region corresponds to the spin injection (extraction), where spin-polarized electrons tunnel from ferromagnet (semiconductor) to semiconductor (ferromagnet). Here, the spacing (d) between the injector and detector contacts was 4.0 μm for both samples. The bias-current dependence of $|V_P|$ clearly differed between the $\text{Co}_2\text{MnSi}/\text{CoFe}/\text{n-GaAs}$ sample and the CoFe/n-GaAs sample. For the $\text{Co}_2\text{MnSi}/\text{CoFe}/\text{n-GaAs}$ sample, $|V_P|$ increased monotonically as $|I|$ increased in the negative bias region, while no clear spin signal was observed in the positive bias region. On the other hand, for the CoFe/n-GaAs sample, $|V_P|$ increased with increasing $|I|$, reached a peak value at $I = -25 \mu\text{A}$, and then decreased with increasing $|I|$ in the negative bias region, while it increased monotonically with increasing $|I|$ in the positive

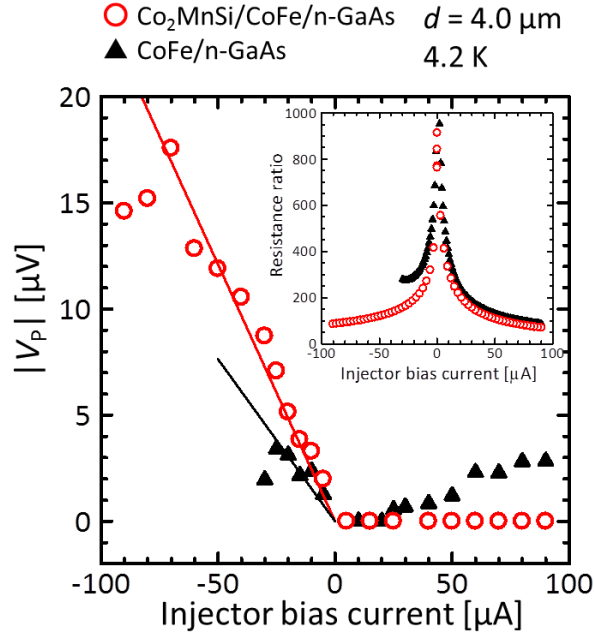


Fig. 3.10. Bias current dependence of V_p measured for a $\text{Co}_2\text{MnSi}/\text{CoFe}/n\text{-GaAs}$ sample and a $\text{CoFe}/n\text{-GaAs}$ reference sample. The solid lines indicate linear least-squares fitting in the low negative-bias region. Inset shows the bias current dependence of the injector junction resistance for both $\text{Co}_2\text{MnSi}/\text{CoFe}/n\text{-GaAs}$

bias region. From the Eq. 3.4, $|V_p|$ depends on I , $P_{\text{inj}}P_{\text{det}}$, ρ , S , l_{sf} , and d . The Eq. 3.4 is valid when the junction resistance is much larger than the spin resistance of the channel, which condition is satisfied in our devices, as shown later. Since the channel structure of GaAs is the same for both samples, the values of ρ , S , l_{sf} , and d are the same. Therefore, the difference in the $|V_p|$ vs. I characteristics between the two samples comes from the difference in the $P_{\text{inj}}P_{\text{det}}$ products. This result indicates that the spin polarization at the 1.1-nm-thick CoFe/GaAs interface of $\text{Co}_2\text{MnSi}/\text{CoFe}(1.1 \text{ nm})/\text{GaAs}$ heterojunction differs from that at the 5-nm-thick CoFe/GaAs interface, which means that Co_2MnSi works as a spin source in the $\text{Co}_2\text{MnSi}/\text{CoFe}/n\text{-GaAs}$ sample even though 1.1-nm-thick CoFe was inserted between the Co_2MnSi and GaAs . This is reasonable because the thickness of the inserted CoFe (1.1 nm) layer was less than the spin diffusion length of CoFe ($\sim 10 \text{ nm}$).⁴⁹

The non-linear relations between $|V_p|$ and I shown in Fig. 3.10 indicate that the value of $|P_{\text{inj}}P_{\text{det}}|^{1/2}$ is not constant against the bias voltage. There have been several experimental^{9, 10, 12} and theoretical³⁹⁻⁴¹ investigations into whether the magnitude and sign of spin

Sample structure	Annealing temperature [°C]	$ P_{\text{inj}} \cdot P_{\text{det}} ^{1/2}$ [%]
Co ₂ MnSi/CoFe/n-GaAs	350	4.4
CoFe/n-GaAs	350	3.5
CoFe/n-GaAs ¹²	–	3.0

Table I. Summary of $|P_{\text{inj}} \cdot P_{\text{det}}|^{1/2}$ in the low negative bias region for a Co₂MnSi/CoFe/n-GaAs sample and CoFe/n-GaAs reference samples with and without annealing.

polarization for the ferromagnet/GaAs heterointerface are affected by a bias condition. Although the junction resistance also affects the spin injection efficiency, the effect was negligible in our devices. The inset in Fig. 3.10 shows the junction resistance of the injector contacts of both CoFe and Co₂MnSi/CoFe as a function of the bias current. The junction resistance was normalized by the spin resistance of the GaAs channel, $\rho l_{\text{sf}}/S$. As shown in the inset, the junction resistance is at least two orders of magnitude larger than the spin resistance for almost all bias regions investigated in this study. Thus, the impedance mismatch problem³ is negligible, and the nonlinear relations between $|V_P|$ and I result from the change in the $P_{\text{inj}} \cdot P_{\text{det}}$ value by the bias voltage rather than from the change in the junction resistance. Table I summarizes the values of $|P_{\text{inj}} \cdot P_{\text{det}}|^{1/2}$ in a low negative bias current region, in which the values of $|P_{\text{inj}} \cdot P_{\text{det}}|^{1/2}$ are almost constant. The value for a sample without post-deposition annealing¹² is also shown for comparison. Importantly, the value of $|P_{\text{inj}} \cdot P_{\text{det}}|^{1/2}$ for the Co₂MnSi/CoFe/n-GaAs sample is larger than those for the CoFe/n-GaAs samples. The larger value of $P_{\text{inj}} \cdot P_{\text{det}}$ obtained for the Co₂MnSi/CoFe/n-GaAs sample cannot be explained by the effect of the impedance mismatch, because the junction resistance of the Co₂MnSi/CoFe/GaAs sample was smaller than that of the CoFe/GaAs one. These results indicate that Co₂MnSi has higher spin polarization and that a Heusler alloy is a promising spin source for efficient spin injection into a semiconductor. Considering that the TMR ratios in MTJs with Co₂MnSi electrodes increase with increasing annealing temperature around 550 °C,⁵¹ there is much room to improve the spin injection efficiency with our sample. It should be noted, however, that high-temperature annealing may lead to interdiffusion of atomic species at a ferromagnet/GaAs interface, resulting in the degradation of spin injection properties. Thus,

the annealing temperature of the Co_2MnSi layer must be optimized to simultaneously obtain high spin polarization and prevent interdiffusion.

3.7 Summary

First, we experimentally found that the TAMR effect was suppressed by inserting a MgO barrier between CoFe and n-GaAs, indicating Fermi-level depinning and lowering of the Schottky barrier height of GaAs. We also found that the non-local spin-valve signal was enhanced by a factor of 38 and the sign was reversed when a MgO barrier was inserted, suggesting that the effective spin polarization increased.

Second, we achieved efficient spin injection and a resultant efficient DNP by using a Co_2MnSi spin source. The maximum electron spin polarization in the GaAs channel observed in the sample with Co_2MnSi electrodes was larger than that observed in the reference sample with CoFe electrodes; this was due to higher spin polarization of Co_2MnSi . This results indicate that the Heusler alloy is a promising spin source for spin injection into a semiconductor.

References

1. S. Datta and B. Das, Appl. Phys. Lett. **56**, 665 (1990).
2. S. Sugahara, M. Tanaka, Appl. Phys. Lett. **84**, 2307 (2004).
3. G. Schmidt, D. Ferrand, L. W. Molenkamp, A. T. Filip and B. J. van Wees, Phys. Rev. B **62**, 4790(R) (2000).
4. E. I. Rashba, Phys. Rev. B **62**, 16267(R) (2000).
5. A. Fert and H. Jaffrès, Phys. Rev. B **64**, 184420 (2001).
6. H. J. Zhu, M. Ramsteiner, H. Kostial, M. Wassermeier, H.-P. Schönherr, and K. H. Ploog, Phys. Rev. Lett. **87**, 016601 (2001).
7. M. Yasar, R. Mallory, A. Petrou, A. T. Hanbicki, G. Kioseoglou, C. H. Li, O. M. J. van't Erve, and B. T. Jonker, Appl. Phys. Lett. **94**, 032102 (2009).
8. B. D. Schultz, N. Marom, D. Naveh, X. Lou, C. Adelman, J. Strand, P. A. Crowell, L. Kronik, and C. J. Palmstrøm, Phys. Rev. B **80**, 201309(R) (2009).
9. X. Lou, C. Adelman, S. A. Crooker, E. S. Garlid, J. Zhang, K. S. M. Reddy, S. D. Flexner, C. J. Palmstrøm, and P. A. Crowell, Nat. Phys. **3**, 197 (2007).
10. G. Salis, A. Fuhrer, R. R. Schlitter, L. Gross, and S. F. Alvarado, Phys. Rev. B **81**, 205323 (2010).
11. G. Salis, S. F. Alvarado, and A. Fuhrer, Phys. Rev. B **84**, 041307 (2011).
12. T. Uemura, T. Akiho, M. Harada, K.-i. Matsuda, and M. Yamamoto, Appl. Phys. Lett. **99**, 082108 (2011).
13. S. Ishida, S. Fujii, S. Kashiwagi, and S. Asano, J. Phys. Soc. Jpn. **64**, 2152 (1995).
14. S. Picozzi, A. Continenza, and A. J. Freeman, Phys. Rev. B **66**, 094421 (2002).
15. X. Y. Dong, C. Adelman, J. Q. Xie, C. J. Palmstrøm, X. Lou, J. Strand, P. A. Crowell, J.-P. Barnes and A. K. Petford-Long, Appl. Phys. Lett. **86**, 102107 (2005).
16. M. C. Hickey, C. D. Damsgaard, I. Farrer, S. N. Holmes A. Husmann, J. B. Hansen, C. S. Jacobsen, D. A. Ritchie, R. F. Lee, G. A. C. Jones, and M. Pepper, Appl. Phys. Lett. **86**, 252106 (2005).
17. O. M. J. van't Erve, A. T. Hanbicki, M. Holub, C. H. Li, C. Awo-Affouda, P. E. Thompson, and B. T. Jonker, Appl. Phys. Lett. **91**, 212109 (2007).
18. S. J. Dash, S. Sharma, R. S. Patel, M. P. de Jong, and R. Jansen, Nature **462**, 491 (2009).

19. M. Tran, H. Jaffrès, C. Deranlot, J.-M. George, A. Fert, A. Miard, and A. Lemaître, *Phys. Rev. Lett.* **102**, 036601 (2009).
20. H. Saito, J. C. Le Breton, V. Zayets, Y. Mineno, S. Yuasa, and K. Ando, *Appl. Phys. Lett.* **96**, 012501 (2010).
21. T. Sasaki, T. Oikawa, T. Suzuki, M. Shiraishi, Y. Suzuki, and K. Noguchi, *IEEE Trans. Magn.* **46**, 1436 (2010).
22. T. Inokuchi, T. Marukame, M. Ishikawa, H. Sugiyama, and Y. Saito, *Appl. Phys. Express* **2**, 023006 (2009).
23. V. G. Truong, P.-H. Binh, P. Renucci, M. Tran, Y. Lu, H. Jaffrès, J.-M. George, C. Deranlot, A. Lemaître, T. Amand, and X. Marie, *Appl. Phys. Lett.* **94**, 141109 (2009).
24. R. Wang, X. Jiang, R. M. Shelby, R. M. Macfarlane, and S. S. P. Parkin, *Appl. Phys. Lett.* **86**, 052901 (2005).
25. W. H. Butler, X.-G. Zhang, and T. C. Schulthess, *Phys. Rev. B* **63**, 054416 (2001).
26. S. Yuasa, A. Fukushima, T. Ngahama, K. Ando, and Y. Suzuki, *Jpn. J. Appl. Phys.* **43**, 588 (2004).
27. C. Gould, C. Rüster, T. Jungwirth, E. Girgis, G. M. Schott, R. Giraud, K. Brunner, G. Schmidt, and L. W. Molenkamp, *Phys. Rev. Lett.* **93**, 117203 (2004).
28. J. Moser, A. Matos-Abiague, D. Schuh, W. Wegscheider, J. Fabian, and D. Weiss, *Phys. Rev. Lett.* **99**, 056601 (2007).
29. M. Yamamoto, T. Ishikawa, T. Taira, G.-f. Li, K.-i. Matsuda, and T. Uemura, *J. Phys.: Condens. Matter* **22**, 164212 (2010).
30. G.-f. Li, Y. Honda, H.-x. Liu, K.-i. Matsuda, M. Arita, T. Uemura, M. Yamamoto, Y. Miura, M. Shirai, T. Saito, F. Shi, and P. M. Voyles, *Phys. Rev. B* **89**, 014428 (2014).
31. T. Uemura, Y. Imai, M. Harada, K.-i. Matsuda, and M. Yamamoto, *Appl. Phys. Lett.* **94**, 182502 (2009).
32. T. Uemura, M. Harada, T. Akiho, K.-i. Matsuda, and M. Yamamoto, *Appl. Phys. Lett.* **98**, 102503 (2011).
33. T. Uemura, M. Harada, K.-i. Matsuda, and M. Yamamoto, *Appl. Phys. Lett.* **96**, 252106 (2010).
34. E. I. Rashba, *Sov. Phys. Solid State* **2**, 1109 (1960).
35. P. D. Dresslhaus, C. M. A. Papavassiliou, R. G. Wheeler, and R. N. Sacks, *Phys. Rev. Lett.* **68**, 106 (1992).

36. Y. Lu, J. C. Le Breton, P. Turban, B. Lépine, P. Schieffer, and G. Jézéquel, *Appl. Phys. Lett.* **89**, 152106 (2006).
37. T. Akiho, T. Uemura, M. Harada, K.-i. Matsuda, and M. Yamamoto, *Appl. Phys. Lett.* **98**, 232109 (2011).
38. J. Fabian, A. Matos-Abiaguea, C. Ertler, P. Stano, I. Žutić, *acta Phys. Slov.* **57**, 565 (2007).
39. H. Dery and L. J. Sham, *Phys. Rev. Lett.* **98**, 046602 (2007).
40. A. N. Chantis, K. D. Belashchenko, D. L. Smith, E. Y. Tsybal, M. van Schilfgaarde, and R. C. Albers, *Phys. Rev. Lett.* **99**, 196603 (2007).
41. S. Honda, H. Itoh, and J. Inoue, *J. Phys. D* **43** 135002 (2010).
42. T. Marukame and M. Yamamoto, *J. Appl. Phys.* **101** 083906 (2007).
43. S. Kawagishi, T. Uemura, Y. Imai, K.-i. Matsuda, and M. Yamamoto, *J. Appl. Phys.* **103**, 07A703 (2008).
44. T. Yano, T. Uemura, K.-i. Matsuda, and M. Yamamoto, *J. Appl. Phys.* **101**, 063904 (2007).
45. G. Salis, A. Fuhrer, and S. F. Alvarado, *Phys. Rev. B*, **80**, 115332 (2009).
46. J. Shiogai, M. Ciorga, M. Utz, D. Schuh, T. Arakawa, M. Kohda, K. Kobayashi, T. Ono, W. Wegscheider, D. Weiss, and J. Nitta, *Appl. Phys. Lett.*, **101**, 212402 (2012).
47. R. I. Dzhioev, K. V. Kavokin, V. L. Korenev, M. V. Lazarev, B. Ya. Meltser, M. N. Stepanova, B. P. Zakharchenya, D. Gammon, and D. S. Katzer, *Phys. Rev. B* **66**, 245204 (2002).
48. H.-x. Liu, Y. Honda, T. Taira, T. Uemura, and M. Yamamoto (unpublished).
49. T. Ishikawa, N. Itabashi, T. Taira, K.-i. Matsuda, T. Uemura, and M. Yamamoto, *J. Appl. Phys.* **105**, 07B110 (2009).

Chapter 4

All electrical investigation of spin dependent transport properties in strained InGaAs channels

In this chapter, spin transport properties of strained InGaAs channels using spin injection from a ferromagnet electrode are described. From observation of Hanle signals, spin lifetime in strained InGaAs channels and GaAs channels were estimated. Strained InGaAs channels exhibited much shorter spin lifetime than that of GaAs channels, indicating that strain induced spin orbit interaction strongly affects to electron spins in strained InGaAs channels. The control of spin orbit interaction is a key role for realization of spin transistors. All electrical investigation of spin dependent transport properties of semiconductor channels with a strong spin orbit interaction opens a path to develop spin transistors.

4.1 Introduction

The injection and detection of spin-polarized electrons using ferromagnet/semiconductor heterojunctions have attracted much interest for creating viable spintronics devices such as spin transistor.^{1, 2} To demonstrate efficient spin injection (detection) and to clarify spin dependent transport properties of semiconductor channels are indispensable for realization of spin transistors. Recently, we demonstrated spin injection into a GaAs channel using CoFe/GaAs heterojunctions³ from the observation of spin-valve signals and Hanle signals in a nonlocal geometry. Co-based Heusler alloys are one candidate for a highly polarized spin source, because we demonstrated giant tunneling magnetoresistance ratios of 1995% at 4.2 K and 354% at 290 K in Co₂MnSi based magnetic tunnel junctions using Mn-rich Co₂MnSi electrodes.⁴ We investigated the applicability of Co-based Heusler alloys to spin injection using Co₂MnSi/CoFe/GaAs heterojunctions and found that the spin injection efficiency with Co₂MnSi/CoFe/GaAs heterojunctions was one order of magnitude larger than that for the CoFe/GaAs heterojunctions.⁵ Moreover, using Co₂MnSi/CoFe/GaAs heterojunctions, we observed the transient behavior of a nuclear magnetic field originating from dynamically polarized nuclear spins of GaAs due to the hyperfine interaction.⁶

To realize the spin transistor, it is also important to clarify spin transport properties of semiconductor channels. In particular, the effect of spin-orbit-interaction (SOI) in III-V semiconductors is a key role for the operation of the spin transistor;¹ that is, injected electron spins from a ferromagnetic source contact are controlled by SOI and collected at a ferromagnetic drain contact. SOI is also known as a major spin relaxation mechanism because an effective SOI magnetic field is momentum dependent. As the velocity of the electron changes by a scattering due to phonon or impurity, the magnitude and direction of the SOI field change, resulting in spin relaxation. The influence of SOI on spin dependent transport properties were investigated through both electrical methods in InGaAs/InAlAs quantum wells^{7, 8} and optical methods in GaAs/AlGaAs quantum wells.^{9, 10} Recently, Kato et al., observed a SOI field in strained In_xGa_{1-x}As channels grown on GaAs by using optical methods and found that the strain plays a crucial role in producing a SOI field.¹¹ Andrei and Zhang analyzed their experimental results using a strain-induced SOI model.¹² Then, the purpose in this chapter is to clarify the spin-dependent transport properties of strained InGaAs channels using ferromagnet/semiconductor heterojunctions. The injection

and detection of spin-polarized electrons using ferromagnet/semiconductor heterojunctions, and characterization of spin dependent transport properties of semiconductors where SOI strongly affects to electron spins are prerequisite for development of spin transistor.

4.2 Experimental methods

Layer structures consisting of (from the substrate side) a 250-nm-thick undoped GaAs buffer layer, a 700-nm-thick n^- - $\text{In}_x\text{Ga}_{1-x}\text{As}$ channel layer, a 15-nm-thick n^- - $\text{In}_x\text{Ga}_{1-x}\text{As} \rightarrow n^+$ -GaAs transition layer, and a 15-nm-thick n^+ -GaAs layer were grown by molecular beam epitaxy on semi-insulating GaAs(001) substrates. The indium composition x was chosen to be 0, 4, and 7%. The doping concentration of n^- - $\text{In}_x\text{Ga}_{1-x}\text{As}$ channel layer was $3 \times 10^{16} \text{ cm}^{-3}$ and that of the n^+ -GaAs layer was $5 \times 10^{18} \text{ cm}^{-3}$ to form a narrow Schottky barrier. Samples were transfer to the second MBE chamber without exposure to air, and a 10-nm-thick Fe spin source layer and a 10-nm-thick Al cap layer were grown at room temperature. Strains in these samples were characterized by two-dimensional reciprocal space mapping (RSM) of high-resolution X-ray diffraction (XRD) around GaAs (224) and (2-24) at room temperature. Samples were processed into lateral spin transport devices using electron beam lithography and Ar ion milling techniques. The size of the injector contact and detector contact were $0.5 \times 10 \mu\text{m}$ and $1.0 \times 10 \mu\text{m}$, respectively, and the spacing between them was 4.0 or 8.0 μm . Spin-dependent transport properties for lateral spin transport devices were evaluated in a four-terminal nonlocal geometry at 4.2 K.

4.3 Experimental results

4.3.1 Structural properties of strained InGaAs channels

Figure 4.1 shows a typical result from X-ray RSM of the sample with $x = 4\%$ around (224). A clear 224_{GaAs} peak from the GaAs substrate and a 224_{InGaAs} peak were observed. The vertical dotted line marks the location where the reciprocal lattice points of a fully-strained layer would appear, whereas the inclined dotted line corresponds to a completely relaxed layer. The observation of the 224_{InGaAs} peak between those lines indicates the InGaAs film fabricated in this study was partially strained. A similar result

was obtained for the sample with $x = 7\%$. It is reasonable for our samples to be partially strained state because the critical thickness of around 300 nm for a GaAs/In_{0.05}Ga_{0.95}As heterostructures grown on a GaAs substrate was reported.¹³ Table I summarizes the indium composition, relaxation rate, and strain values for the InGaAs films. The strain for the In_{0.07}Ga_{0.93}As film was approximately 20% larger than that for the In_{0.04}Ga_{0.96}As film.

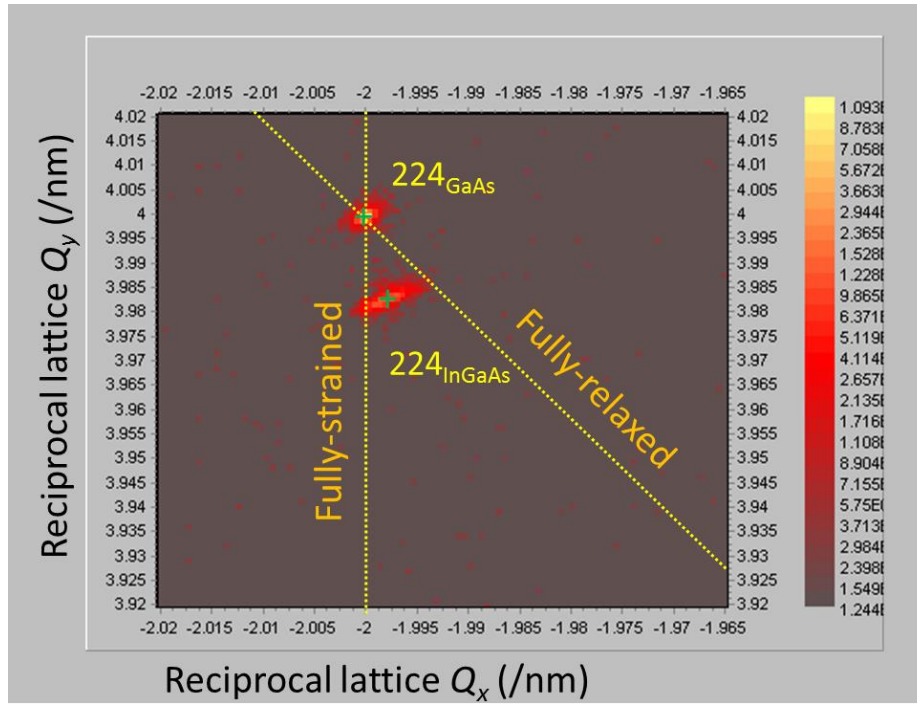


Fig. 4.1. A typical result from X-ray reciprocal mapping (RSM) of the sample with $x = 4\%$ around (224).

Table I. Summary of strain values and relaxation rate for In_{*x*}Ga_{1-*x*}As films with different indium composition x .

x (%)	Relaxation rate (%)	ϵ_{zz} (%)	ϵ_{xx} (%)	ϵ_{xy} (%)
4	44	0.146	-0.161	-0.022
7	58	0.181	-0.198	-0.126

4.3.2 Electrical detection of spin injection

Figure 4.2(a) shows a plot of nonlocal voltage (V_{NL}) divided by injection current (I) as a function of in-plane magnetic field for a lateral spin transport device with $x = 4\%$. The magnetic field was applied along the $[110]_{\text{GaAs}}$ axis direction (the shorter direction of the junction), which corresponded to the easy axis for the magnetization of Fe electrodes. Similar magnetization anisotropy has been observed in a sample with $x = 0$ and 7% , and $\text{Co}_2\text{MnSi}/\text{CoFe}$ electrodes.⁶ A bias current (I) of $-20 \mu\text{A}$ was supplied, where electron spins were injected from the Fe to the InGaAs channel. We also observed spin-valve signals for devices with $x = 0$ and 7% .

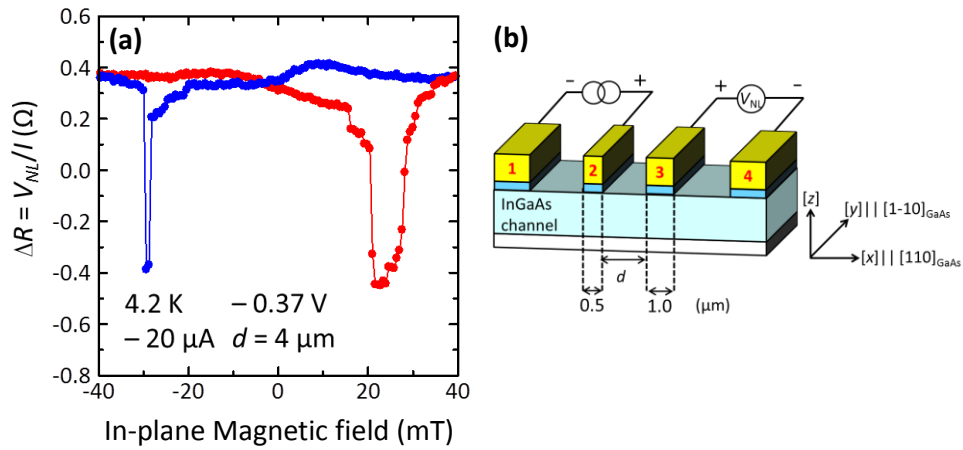


Fig. 4.2. (a) Plot of non-local voltage (V_{NL}) divided by injection current (I) as a function of in-plane magnetic field for a lateral spin transport device with indium composition $x = 4\%$. (b) Schematic device structure of a four-terminal lateral spin transport device and circuit configuration for the nonlocal measurement.

Figure 4.3(a)-(c) plot V_{NL}/I as a function of out-of-plane magnetic field (B_z) in the parallel magnetization configuration for lateral spin transport devices with different indium compositions of 0, 4 and 7%, respectively. We observed clear Hanle signals, and confirmed spin injection from the Fe electrode into the GaAs channel and strained InGaAs channels. The solid lines in the figures are results of a fitting using the spin drift-diffusion model, in which V_{NL}/I as a function of B_z can be expressed by²⁰

$$\frac{V_{NL}(B_z)}{I} \propto \int_0^{\infty} \frac{1}{\sqrt{4\pi Dt}} \exp\left(-\frac{d^2}{4Dt}\right) \cos(\omega_L t) \exp\left(-\frac{t}{\tau}\right) dt, \quad (4.1)$$

$$\omega_L = \frac{g\mu_B B_z}{\hbar}$$

where d is the distance between the injector and the detector contacts, τ is the spin lifetime, $D = l_{SF}^2 / \tau$ is the diffusion constant, l_{SF} is the spin diffusion length, ω_L is the Larmor frequency, g is an electron g factor (-0.44 for GaAs, -0.56 for $\text{In}_{0.04}\text{Ga}_{0.96}\text{As}$ and -0.66 for $\text{In}_{0.07}\text{Ga}_{0.93}\text{As}$ ²¹), μ_B is the Bohr magneton, and \hbar is the reduced Planck's constant. From the fitting, τ was estimated to be 16 ns for the GaAs channel. This value of the spin lifetime is comparable to those obtained for GaAs with a doping concentration of in the order of 10^{16} cm^{-3} .²² On the other hand, the spin lifetime was estimated to be 2 ns for the $\text{In}_{0.04}\text{Ga}_{0.96}\text{As}$ channel and 1.4 ns for the $\text{In}_{0.07}\text{Ga}_{0.93}\text{As}$ channel. Interestingly, the values of spin lifetime for strained InGaAs channels were much shorter than that for the GaAs channel. Figure 4.3(d) shows a comparison of the bias-voltage dependence of the spin lifetime for different indium compositions. Although spin lifetime was decreased as the bias voltage across the junction increased for all samples, the spin lifetime for the GaAs channel was much larger than those for strained InGaAs channels in all bias regions. And the sample with $x = 4\%$ showed longer spin lifetime than the sample with $x = 7\%$. These results indicated that a spin relaxation mechanism enhanced or introduced in strained InGaAs channels compared by the GaAs channel.

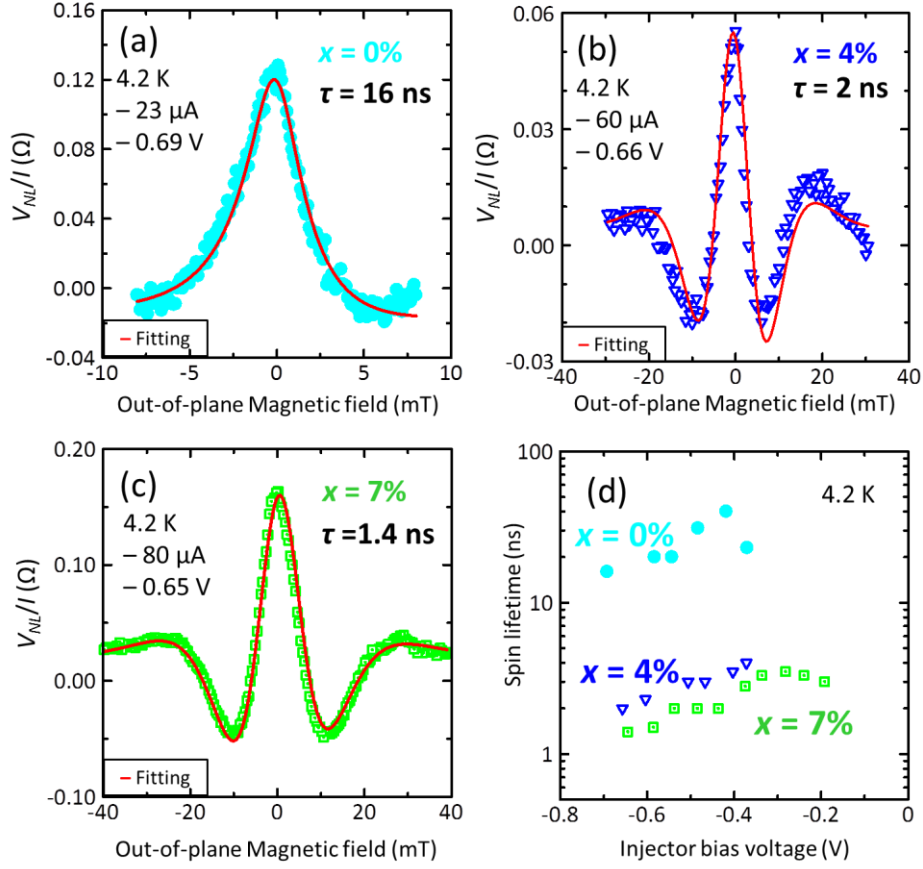


Fig 4.3. (a)-(c) Plots of V_{NL}/I for devices with $d = 8.0 \mu\text{m}$ as a function of out-of-plane magnetic field (B_z) for samples with $x = 0, 4, 7\%$, respectively. The solid lines are the result of the fitting using Eq. 4.1. (d) Comparison of bias voltage dependence of spin lifetime with different indium composition.

4.4. Discussion on the possible origin of the reduction of spin lifetime in strained InGaAs

Then, we discuss the strong reduction of the spin lifetime in strained InGaAs channels. Generally, spin relaxation mechanism in semiconductors is dominated by the D'yakanov-Perel' (DP) mechanism,¹⁷ Elliot-Yaffet (EY) mechanism,¹⁸ Bir-Aronov-Pikus (BAP) mechanism,¹⁹ and hyperfine interaction. First, the hyperfine interaction is the interplay between electron spins and nuclear spins. Through the hyperfine interaction, dynamically polarized nuclear spins affects electron spins as a nuclear magnetic field. In GaAs samples, clear nuclear magnetic field was observed in oblique Hanle effect measurements, however, in strained InGaAs samples, clear nuclear magnetic field was not observed. Thus, the hyperfine interaction was not responsible for the reduction of spin lifetime in strained InGaAs channels. Second, the BAP mechanism is a process involving the recombination of an electron-hole pair. Therefore, the BAP mechanism would not affects electron spins in our n-type strained InGaAs channels. Finally, in the EY and DP mechanism, spins can relax via momentum scattering and spin-orbit interaction. Thus, modulation of mobility and/or SOI in strained InGaAs channels were considered. Table 2 summarizes the mobility and resistivity for the GaAs channel and InGaAs channels obtained from identically fabricated Hall bars. Although the mobility value decreased as the indium composition increased, the decrease ratio (defined by $\mu(x)/\mu(0)$ where $\mu(x)$ is a mobility with indium composition x) of the mobility value was 91% for the sample with $x = 4\%$ and 70% for the sample with $x = 7\%$ with respect to the GaAs channel. These values were not comparable with the decrease ratio of spin lifetime.

Next, we discuss the influence of strain-induced SOI on strained InGaAs channels. The Hamiltonian of the strain-induced SOI is given by¹²

$$H_{SOI} = H_{SIA} + H_{BIA}, \quad (4.2)$$

$$H_{SIA} = \frac{1}{2} C_3 \varepsilon_{xy} (k_y \sigma_x - k_x \sigma_y), \quad (4.3)$$

$$H_{BIA} = D (\varepsilon_{zz} - \varepsilon_{xx}) (k_x \sigma_x - k_y \sigma_y), \quad (4.4)$$

where, H_{SIA} and H_{BIA} are Hamiltonian of structural-inversion-asymmetry (SIA) type strain-induced SOI and that of bulk-inversion-asymmetry (BIA) type strain-induced SOI, respectively. C_3 and D are material constants, $\sigma_{x,y,z}$ are the 3 spin-Pauli matrices, ε_{ij} , ($i, j =$

Table II. Summary of strain values and relaxation rate for $\text{In}_x\text{Ga}_{1-x}\text{As}$ films with different indium composition x .

x (%)	Mobility (cm^2/Vs)	Resistivity (Ωcm)
0	2300	4.1×10^{-2}
4	2100	7.6×10^{-2}
7	1600	9.7×10^{-2}

x, y, z) are the components of the strain tensor, and k_x and k_y are the wave vector components. Based on the strain induced SOI model, electron spins in strained InGaAs channels are affected by the effective magnetic field (B_{SOI}). When electrons experience a momentum scattering, wave vector components randomly change, resulting in the strength and direction of B_{SOI} randomly change. That is the origin of dephasing for electron spins and reduction of spin lifetime compared with the non-strained GaAs channel. Using $C_3/\hbar = 2.0 \times 10^5$ m/s and $D/\hbar = 2.1 \times 10^4$ m/s from ref. 12, typical values of SOI field with $k_{[110]}$ electrons were 0.69 mT for the $x = 4\%$ sample, and 0.88 mT for the $x = 7\%$ sample. Those effective magnetic fields would affect to electron spin lifetime.

Finally, we investigated a device with different channel direction because B_{SOI} depend on k . Figure 4.4(a) shows a typical Hanle signal for the device with the $[1-10]_{\text{GaAs}}$ channel and indium composition $x = 4\%$. The estimated spin lifetime of 4.5 ns was longer than the device with $[110]_{\text{GaAs}}$ channel as shown in Fig. 4.3(b). Figure 4.4(b) shows a comparison of a bias voltage dependence of the spin lifetime for devices with the $[1-10]_{\text{GaAs}}$ channel and the $[110]_{\text{GaAs}}$ channel. For all bias region, spin lifetime for the $[110]_{\text{GaAs}}$ channel were shorter than the $[1-10]_{\text{GaAs}}$ channel. These results were understood using the strain induced SOI model as follows. From spin-valve measurements, spin direction S was parallel to $[110]_{\text{GaAs}}$ direction. According to Eq 4.3 and 4.4, for electrons with k_{110} , B_{SOI} is parallel to the $[1-10]_{\text{GaAs}}$ direction. Thus, S and B_{SOI} are orthogonal for the device with $[110]_{\text{GaAs}}$ channel ($S \perp B_{SOI}$). On the other hand, S and B_{SOI} are parallel for the device with $[1-10]_{\text{GaAs}}$ channel ($S \parallel B_{SOI}$) because B_{SOI} is parallel to the $[110]_{\text{GaAs}}$ direction for electrons with k_{1-10} . In the $S \perp B_{SOI}$ configuration, Hanle precession occurs due to both external magnetic field and SOI field, resulting in the shorter spin lifetime than the $S \parallel B_{SOI}$ configuration. These results indicate that the major effect for the reduction of spin lifetime was strain-induced spin orbit interaction.

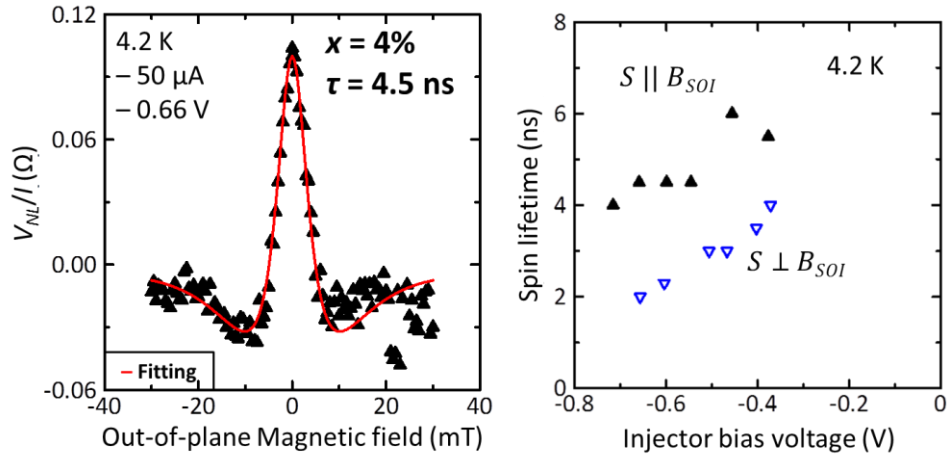


Figure 4.4. (a) Plot of V_{NL}/I as a function of B_z for a device which has the effective magnetic field (B_{SOI}) and electron spins (S) are parallel configuration ($S \parallel B_{SOI}$). (b) Comparison of bias voltage dependence of spin lifetime for devices with the $S \parallel B_{SOI}$ and the $S \perp B_{SOI}$ configuration.

4.5. Summary

In summary, we confirmed spin injection into a GaAs channel and strained InGaAs channels from observation of spin-valve signals and Hanle signals using Fe electrodes. Obtained spin lifetime were much shorter for strained InGaAs channels compared to the GaAs channel. Possible origins of the reduction of spin lifetime in strained InGaAs were discussed and strain-induced spin orbit interaction can explain those results. We clarified spin dependent transport properties of strained InGaAs channels by all-electrical method. This method can be a tool for probing the effect of spin relaxation mechanism as well as realizing future semiconductor based spintronics devices.

References

1. S. Datta and B. Das, *Appl. Phys. Lett.* **56**, 665 (1990).
2. S. Sugahara and M. Tanaka, *Appl. Phys. Lett.* **84**, 2307 (2004).
3. T. Uemuta, T. Akiho, M. Harada, K.-i. Matsuda, and M. Yamamoto, *Appl. Phys. Lett.* **99**, 082108 (2011).
4. H.-x. Liu, Y. Honda, T. Taira, K.-i. Matsuda, M. Arita, T. Uemura, and M. Yamamoto, *Appl. Phys. Lett.* **101**, 132418 (2012).
5. Y. Ebina, T. Akiho, H.-x. Liu, M. Yamamoto, and T. Uemura, *Appl. Phys. Lett.* **104**, 172405 (2014).
6. T. Akiho, J. Shan, H.-x. Liu, K.-i. Matsuda, M. Yamamoto, and T. Uemura, *Phys. Rev. B* **87**, 235205 (2013).
7. J. Nitta, T. Akazaki, H. Takayanagi, and T. Enoki, *Phys. Rev. Lett.* **78**, 1335 (1997).
8. S. Faniel, T. Matsuura, S. Mineshige, Y. Sekine, and T. Koga, *Phys. Rev. B* **83**, 115309 (2011).
9. M. P. Walsesr, C. Reichl, W. Wegscheider, and G. Salis, *Nature Phys.* **8**, 757, (2012).
10. H. Sanada, T. Sogawa, H. Gotoh, K. Onomitsu, M. Kohda, J. Nitta, and P. V. Santos, *Phys. Rev. Lett.* **106**, 216602 (2011).
11. Y. Kato, R. C. Myers, A. C. Gossard, and D. D. Awschalom, *Nature (London)*, **427**, 50 (2004).
12. B. A. Bernevig and S.-C. Zhang, *Phys. Rev. B*, **72**, 115204 (2005).
13. Y. C. Chen and P. K. Bhattacharya, *J. Appl. Phys.* **73**, 7389 (1993).
14. J. Fabian, A. Matos-Abiaguea, C. Ertlera, P. Stano, and I. I. Zutic, *Acta. Phys. Slovaca*, **57**, 565 (2007).
15. C. Weisbuch and C. Hermann, *Phys. Rev. B*, **15**, 816 (1977).
16. R. I. Dzhioev, K. V. Kavokin, V. L. Korenev, M. V. Lazarev, B. Ya. Meltser, M. N. Stepanova, B. P. Zakharchenya, D. Gammon, and D. S. Katzer, *Phys. Rev. B* **66**, 245204 (2002).
17. M. I. D'yakonov and V. I. Perel', *Zh. Eksp. Teor. Fiz.* **65**, 362 (1973).
18. R. J. Elliott, *Phys. Rev.* **96**, 266 (1954).
19. G. L. Sir, A. G. Aronov, and G. E. Pikus *Zh. Eksp. Teor. Fiz.* **69**, 1382 (1975).

Chapter 5

Electrical detection of dynamically polarized nuclear spins and coherent control of nuclear spins through nuclear magnetic resonance

In this chapter, the electrical detection of dynamically polarized nuclear spins, nuclear magnetic resonance, and coherent control of nuclear spins using $\text{Co}_2\text{MnSi}/\text{CoFe}/\text{GaAs}$ spin injection devices is described. Dynamic nuclear polarization (DNP) due to spin injection significantly enhances nuclear spin polarization by a factor of 1000 compared to a case without DNP. DNP also enhances signal-to-noise ratios on nuclear magnetic resonance (NMR). In this chapter, electrical detection of DNP and NMR in spin injection devices are described for the first step to developing a novel semiconductor-based NMR system. Next, using pulsed NMR techniques, the Rabi oscillation which is an evidence of coherent control of nuclear spins is observed. These results provide a fundamental technology for semiconductor-based nuclear spin quantum bits.

5.1 Introduction

Nuclear spins are an ideal system for implementing quantum bits because of an extremely long coherence time. Demonstration of quantum algorithm using ^1H and ^{13}C nuclei in a liquid was realized by nuclear magnetic resonance (NMR) techniques.¹ However, coherent control of nuclear spins in a solid state device are important for development of scalable quantum information devices.² Nuclear spins in semiconductors have attracted much interest for the solid state quantum bit because, efficient nuclear spin polarization is obtained through the dynamic nuclear polarization (DNP),³⁻⁵ and small size and integrated devices can be fabricated using micro fabrication methods. DNP referred as an effective polarization of nuclear spins due to the transfer of angular momentum from polarized electron spins to nuclei through the hyperfine interaction.⁶ In the case without DNP, nuclear spin polarization is in the order of 10^{-6} for ^{69}Ga at 4.2 K and 0.1 T from the Boltzmann distribution. We recently demonstrated highly efficient DNP in GaAs using spin injection from a Co_2MnSi spin source and obtained nuclear spin polarization of around 10^{-2} .⁷ This value is four orders of magnitude larger than the case without DNP.

Polarized nuclear spins, on the contrary, affect electron spins as an effective magnetic field or Overhauser field. One can evaluate the degree of nuclear spin polarization through the strength of the Overhauser field. Oblique Hanle effect measurements have been widely used for the detection of Overhauser field, and both optical detection through a spin-LED with an MnSb electrode⁸ and with an Fe electrode,⁹ and recently electrical detection through a lateral spin-transport device with an Fe^{10, 11} or (Ga,Mn)As¹² electrode have been demonstrated.

There are several reports on the coherent control of nuclear spins in semiconductors. Electrical detection of the coherent control of nuclear spins in GaAs were demonstrated in quantum Hall systems using a Hall bar¹³ and a point contact device¹⁴ formed on a GaAs/AlGaAs two dimensional electron system. Optical detection of the coherent control of nuclear spins were also demonstrated, and the intrinsic phase coherence time were evaluated in GaAs/AlGaAs quantum wells.¹⁵ However, quantum Hall systems works only under quantum Hall states with extremely large magnetic (> 5 T) field and low temperature (< 1 K). The device size for optical polarization and detection of nuclear spins is limited by a few tens μm due to diameter of incident lights.

Then, we propose a novel NMR system using a spin injection device for quantum bit application. Figure 5.1 shows the schematic image of the quantum bit. The quantum bit operation is as follows. (1) Electron spin injection from Co_2MnSi into GaAs, (2) nuclear spin polarization through DNP, (3) quantum operation of the nuclear spin quantum bit through NMR, (4) and finally, detection of the nuclear spin state through detection of the nuclear field acting on electron spins.

To realize such a device, the purpose of this study is twofold. The first purpose is to understand the transient behavior of nuclear spins in GaAs channels using all electrical polarization and detection. The transient oblique Hanle signals were investigated and discussed the model for the Overhauser field in a transient state. While the electrical detection of oblique Hanle signals has been done only in a steady state,¹⁰ we observe oblique Hanle signals in a transient state, in which the magnetic field is swept faster than the relaxation time of the nuclear spins. This gives us an important insight towards an understanding of nuclear spin dynamics, especially, the transient response of nuclear spins to a change in the magnetic field, and the characteristic time needed for the nuclear spins to reach a steady state through the DNP which directly related to an initialization process of nuclear spins in spin injection devices. The second purpose is to demonstrate coherent control nuclear spin states through the NMR technique in spin injection devices using Co_2MnSi spin source. The demonstration of the coherent control of nuclear spins in spin injection devices provides the proposed solid-state quantum bit.

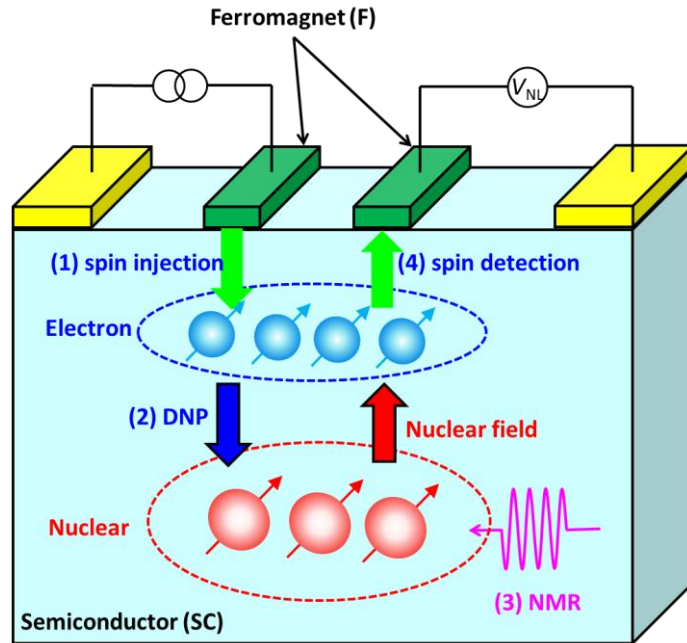


Figure 5.1. A novel NMR system using spin injection device for quantum bit application. (1) Electron spin injection from Co_2MnSi into GaAs, (2) nuclear spin polarization through DNP, (3) quantum operation of the nuclear spin quantum bit through NMR, (4) and finally, detection of the nuclear spin state through detection of the nuclear field acting on electron spins.

5.2 Experimental methods

We prepared two samples. Both samples have a similar layer structure which consist of $\text{Co}_2\text{MnSi}/\text{CoFe}$ bilayer spin source and GaAs layers. The difference between two samples was thickness of the CoFe insertion layer (t_{CoFe}) with $t_{\text{CoFe}} = 1.1$ nm for the first sample and $t_{\text{CoFe}} = 1.3$ nm for the second sample, as shown in figure 5.2(a). Layer structures

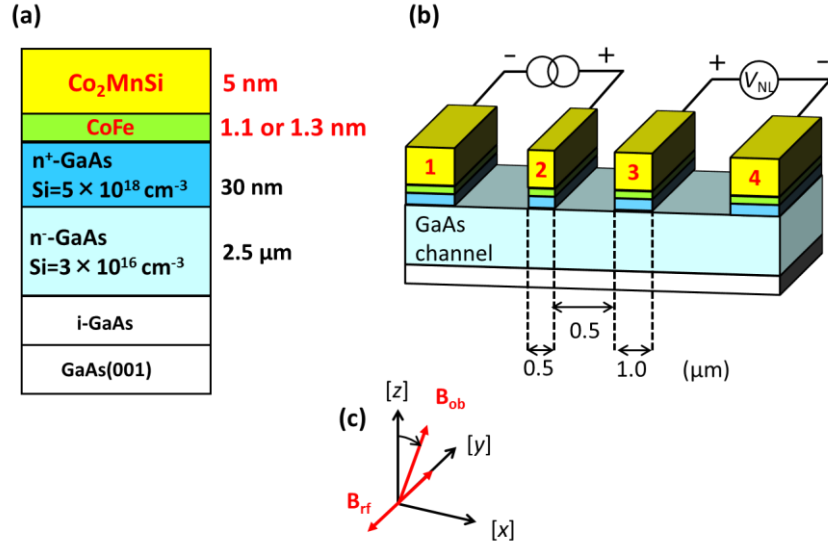


Figure 5.2. (a) Schematic layer structure. (b) Schematic device structure and measurement circuit in the nonlocal geometry. (c) Magnetic field set up for the electrical detection of NMR in spin injection devices.

consisting of (from the substrate side) a 250-nm-thick undoped GaAs buffer layer, a 2.5- μm -thick n^- -GaAs ($\text{Si} = 3 \times 10^{16} \text{ cm}^{-3}$) channel layer, a 15-nm-thick n^- -GaAs \rightarrow n^+ -GaAs transition layer, and a 15-nm-thick n^+ -GaAs ($\text{Si} = 5 \times 10^{18} \text{ cm}^{-3}$) layer were grown by MBE. An ultra-thin CoFe insertion layer and a 5-nm-thick $\text{Co}_2\text{Mn}_{1.30}\text{Si}$ spin source layer (Fig. 5.2(a)) were deposited by magnetron sputtering at room temperature. A Mn-rich Co_2MnSi film was used to suppress the harmful Co_{Mn} antisite to improve the half-metallicity.^{17, 18} Finally, a 5-nm-thick Ru cap layer was deposited using magnetron sputtering at room temperature. We recently investigated the effect of the CoFe insertion thickness on spin injection properties. And we found that CoFe insertion thickness significantly affects spin injection efficiency and a device with $t_{\text{CoFe}} = 1.3 \text{ nm}$ exhibited highest spin injection efficiency among various t_{CoFe} from 0 to 4.1 nm.¹⁶ Using electron beam (EB) lithography and Ar ion milling techniques, lateral spin transport devices as shown in Fig. 5.2(b) were fabricated. The size of the injector contact (contact-2) and detector contact (contact-3) were $0.5 \times 10 \mu\text{m}$ and $1.0 \times 10 \mu\text{m}$, respectively, and the spacing between them was 0.5 μm .

We defined the longer direction of the junction as the y -axis direction. The sample was evaluated in a four-terminal non-local geometry in which the nonlocal voltage (V_{NL})

between contact-3 and contact-4 was measured under a constant current (I) supplied between contact-2 and contact-1 at 4.2 K. For the detection of Overhauser magnetic field, we conducted oblique Hanle effect measurements, in which oblique magnetic field (\mathbf{B}_{ob}) is applied obliquely with respect to spin direction \mathbf{S} so that electron spins make precession with nuclear field (\mathbf{B}_{n}) and \mathbf{B}_{ob} . For the detection of NMR, we applied oblique magnetic field and rf-magnetic field parallel to the y -axis direction using a 11 turns coil putting into the cryostat with the sample.

5.3 Experimental results and discussion

5.3.1 Electrical detection of Overhauser field in a lateral spin transport device using $\text{Co}_2\text{MnSi}/\text{CoFe}/\text{n-GaAs}$ junctions

In this section, we describe the electrical detection of the Overhauser field through the observation of oblique Hanle signals using the $\text{Co}_2\text{MnSi}/\text{CoFe}/\text{n-GaAs}$ spin injection device with $t_{\text{CoFe}} = 1.1$ nm. The steady-state Overhauser field (\mathbf{B}_{n}) induced by the DNP can be expressed by⁶

$$\mathbf{B}_{\text{n}} = fb_n \frac{\mathbf{B}_{\text{ob}} \cdot \mathbf{S}}{B_{\text{ob}}^2 + \xi B_l^2} \mathbf{B}_{\text{ob}}, \quad (5.1)$$

where f (≤ 1) is the leakage factor and b_n is the effective field due to the polarization of nuclear spins, which takes the negative value of -17 T in GaAs for the theoretical ideal case.¹⁹ \mathbf{S} is the average electron spin ($|\mathbf{S}| = 1/2$ corresponds to $P_{\text{GaAs}} = 100\%$), \mathbf{B}_{ob} is the external magnetic field, B_l is the local dipolar field experienced by the nuclei, and ξ is a numerical coefficient on the order of unity, which depends on the nature of the spin-spin interactions.^{10,19} In the oblique Hanle effect measurement, \mathbf{B}_{ob} is applied obliquely with respect to \mathbf{S} so that electron spins make precession with \mathbf{B}_{n} and \mathbf{B}_{ob} . Note that in the conventional Hanle effect measurement, in which \mathbf{S} and \mathbf{B}_{ob} are orthogonal, no nuclear field is generated because $\mathbf{B}_{\text{ob}} \cdot \mathbf{S} = 0$. Figure 5.3(a) shows a simulated non-local voltage using Eq. 5.1 and 3.5 as a function of B_{ob} . Here, we set $\mathbf{S} = S\mathbf{x}$ and $\mathbf{B}_{\text{ob}} = B_{\text{ob}}(\mathbf{x}\sin\theta + \mathbf{z}\cos\theta)$, where \mathbf{x} and \mathbf{z} are unit vectors along the x -axis and z -axis directions, respectively.

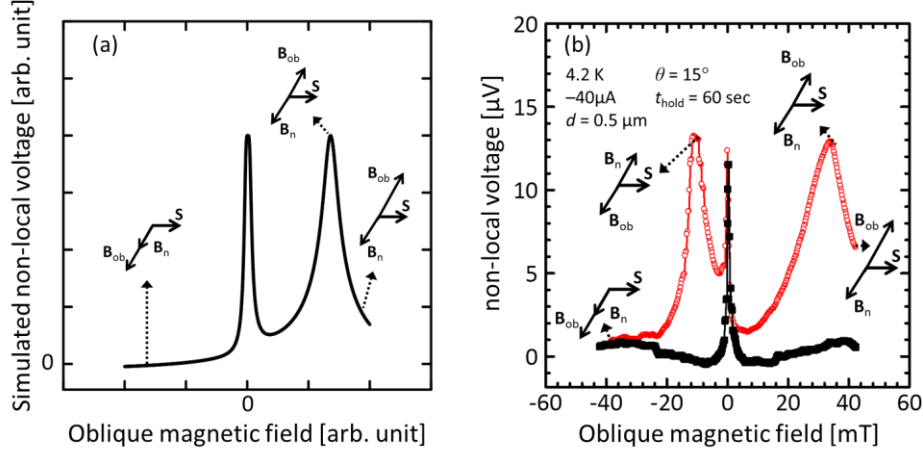


Fig 5.3. (a) Simulated nonlocal voltage in the oblique Hanle effect using as a function of oblique magnetic field (B_{ob}). The vector diagrams show the relative orientation of the average electron spin \mathbf{S} , the oblique magnetic field \mathbf{B}_{ob} , and the nuclear field \mathbf{B}_n . (b) B_{ob} dependence of the nonlocal voltage for the $\text{Co}_2\text{MnSi}/\text{CoFe}/n\text{-GaAs}$ sample in the P magnetization configuration. The magnetic field was swept from +42 to -42 mT (open circle) and was swept back from -42 to +42 mT (black square) with a sweep rate of 0.18 mT/s.

Considering that electron spins experience the total magnetic field of $\mathbf{B}_{ob} + \mathbf{B}_n$, and b_n is negative, the behavior of the nonlocal voltage shown in Fig. 5.3(a) can be explained as follows. At $B_{ob} > 0$, \mathbf{B}_n and \mathbf{B}_{ob} are anti-parallel, and electron spins experience a smaller effective magnetic field than $|\mathbf{B}_{ob}|$. When \mathbf{B}_n and \mathbf{B}_{ob} cancel each other, electron spins get polarized and the non-local voltage shows a satellite peak. At $B_{ob} < 0$, on the other hand, no satellite peak appears, because \mathbf{B}_n and \mathbf{B}_{ob} are parallel and no cancelation occurs. Since it takes several seconds or more for the nuclear field to reach the steady state,⁷⁻¹² very slow sweeping of the external magnetic field is necessary for the steady-state measurement.

Figure 5.3(b) shows the B_{ob} dependence of the nonlocal voltage for a $\text{Co}_2\text{MnSi}/\text{CoFe}/n\text{-GaAs}$ sample in the parallel magnetization configuration. Since \mathbf{S} is parallel to the x -axis direction in the $\text{Co}_2\text{MnSi}/\text{CoFe}/n\text{-GaAs}$ sample, we applied \mathbf{B}_{ob} along the direction oblique by 15 degree from the z -axis in the x - z plane so that electron spins were affected by \mathbf{B}_{ob} and \mathbf{B}_n . The device was first initialized at $B_{ob} = +42$ mT for a hold

time (t_{hold}) of 60 s at an injection current of $-40 \mu\text{A}$, so that nuclear spins became dynamically polarized. The magnetic field was then swept from $+42 \text{ mT}$ to -42 mT (negative sweep direction) and was swept back from -42 mT to $+42 \text{ mT}$ (positive sweep direction) with a sweep rate of 0.18 mT/s . This sweep rate was too fast for the nuclear field to reach the steady state. Compared to the steady-state signal, the observed transient oblique Hanle signal has two features: (1) An additional satellite peak is observed at -10 mT in the negative sweep direction, and (2) no satellite peak is observed in the positive sweep direction, showing a clear hysteretic nature depending on the sweep direction.

5.3.2 Transient behavior of nuclear spins through the electrical detection of oblique Hanle signals

To explain the observed oblique Hanle signal, we discuss the behavior of the nuclear spin in the transient state. In the negative sweep direction, the behavior of the nuclear field for $B_{\text{ob}} > 0$ is qualitatively similar to that for the steady-state nuclear field; i.e., the nuclear field is generated along the anti-parallel direction to \mathbf{B}_{ob} during an initial holding time at $B_{\text{ob}} = +42 \text{ mT}$, and then \mathbf{B}_{ob} and \mathbf{B}_{n} cancel each other at $B_{\text{ob}} = +33 \text{ mT}$. In a similar way, the observation of the satellite peak at $B_{\text{ob}} = -10 \text{ mT}$ indicates that electron spins are repolarized due to the cancellation of \mathbf{B}_{ob} and \mathbf{B}_{n} . However, this anti-parallel state for \mathbf{B}_{n} with respect to \mathbf{B}_{ob} is the transient state because \mathbf{B}_{n} and \mathbf{B}_{ob} are in a parallel configuration at $B_{\text{ob}} < 0$ in the steady state, as indicated by Eq. 5.1. Then, \mathbf{B}_{n} gradually goes to the steady state, and it reaches almost the steady state at $B_{\text{ob}} = -42 \text{ mT}$, resulting in being parallel to \mathbf{B}_{ob} . In the positive sweep direction, \mathbf{B}_{ob} and \mathbf{B}_{n} are parallel at $B_{\text{ob}} < 0$, and this parallel configuration is transiently kept just after \mathbf{B}_{ob} is reversed from the negative direction to the positive one. Thus, no cancellation occurs between \mathbf{B}_{ob} and \mathbf{B}_{n} , resulting in the disappearance of the satellite peak at $B_{\text{ob}} > 0$ for the positive sweep direction.

As discussed above, the transient oblique Hanle signals observed in the $\text{Co}_2\text{MnSi/CoFe/n-GaAs}$ sample can be qualitatively explained by adiabatic nuclear spin reversal; that is, the nuclear spins adiabatically rotate by 180 degrees when the magnetic field crosses zero. A similar adiabatic nuclear spin reversal has been reported in the electrical detection of spin-valve signals for lateral spin transport devices with Fe/GaAs

Schottky tunnel junctions,¹¹ and in the optical detection of oblique Hanle signals for a spin-LED with a MnSb ferromagnet electrode.⁹ However, there has been no report on the transient behavior of the nuclear spins through the electrical detection of oblique Hanle signals. In this study, we have shown that adiabatic nuclear spin reversal with the magnetic field is an important factor in understanding transient oblique Hanle signals.

In the spin-valve signal measurement for the Co₂MnSi/CoFe/n-GaAs sample, the dip structure was observed at $B_x \cong 0$, as shown in Fig. 5.4(a), indicating that electron spins were depolarized. This contrasted with the result for the CoFe/n-GaAs sample as shown in figure 5.4(b), in which the dip structure was not clearly observed in CoFe/n-GaAs samples¹⁸ and the spin-valve signal was almost unchanged from V_p at a zero in-plane magnetic field. For the Co₂MnSi/CoFe/n-GaAs sample, the Overhauser field with its direction parallel or anti-parallel to \mathbf{B}_x was generated at a sufficiently large $|\mathbf{B}_x|$. Since the magnetization of the Co₂MnSi/CoFe electrode oriented to the x -axis direction, the stray field from the Co₂MnSi/CoFe electrode penetrated almost vertically into the GaAs channel. Thus, the Overhauser field dynamically rotated and oriented to the direction of the stray field at $B_x = 0$, causing electron spins to be completely depolarized. Note that since the stray field is comparable to or smaller than B_i , the strength of the steady-state Overhauser field generated by the stray field as well as that of the stray field itself is too small for electron spins to be completely depolarized. On the other hand, for the CoFe/n-GaAs sample, the stray field penetrated along the y -axis direction, since the magnetization of the CoFe/n-GaAs electrode oriented to the y -axis direction. Thus, the direction of the Overhauser field oriented parallel or anti-parallel to the y -axis direction, resulting in no electron spin precession occurring.

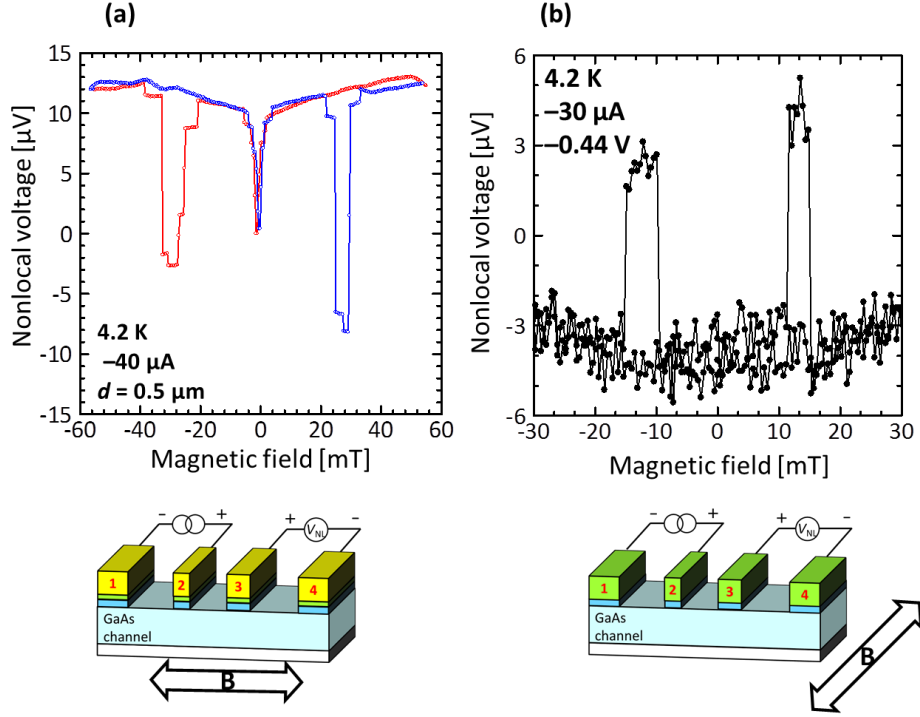


Figure 5.4. (a) Spin-valve signal in the $\text{Co}_2\text{MnSi}/\text{CoFe}/\text{n-GaAs}$ sample. In-plane magnetic field was applied parallel to the x -axis direction. (b) Spin-valve signal in the $\text{CoFe}/\text{n-GaAs}$ sample. In-plane magnetic field was applied parallel to the y -axis direction.

5.3.3 Estimation of nuclear field strength

One can estimate the strength of the nuclear field from the oblique Hanle signal because $\mathbf{B}_{\text{ob}} + \mathbf{B}_{\text{n}} = 0$ is satisfied at the satellite peak position. Furthermore, one can estimate through transient analysis the time scale needed for the nuclear spins to reach a steady state. Figure 5.5(a) and 5.5(b) shows the t_{hold} dependence of the observed satellite peak position for $B_{\text{ob}} > 0$. The circles and triangles in the Fig. 5.5(b) indicate the data for the $\text{Co}_2\text{MnSi}/\text{CoFe}/\text{n-GaAs}$ sample and those for the non-annealed $\text{CoFe}/\text{n-GaAs}$ sample, respectively. For both samples, the satellite peak position shows almost exponential dependence. From the rate equation for the DNP, the time evolution of the nuclear field is given by⁸

$$B_N(t) = B_N(\infty) \left\{ 1 - \exp \left[-t \left(\frac{1}{T_P} + \frac{1}{T_1} \right) \right] \right\} \quad (5.2)$$

where $B_N(\infty)$ is the steady-state Overhauser field, which is given by Eq. 5.1, T_P^{-1} and T_1^{-1} are a rate for nuclear polarization through DNP and that for nuclear spin relaxation to lattice, respectively. Importantly, the saturation value of the satellite peak position of 37 mT for the $\text{Co}_2\text{MnSi}/\text{CoFe}/\text{n-GaAs}$ sample is larger than that of 16 mT for the $\text{CoFe}/\text{n-GaAs}$ sample, suggesting a greater Overhauser magnetic field due to the higher spin polarization of the Co_2MnSi . The Overhauser magnetic field of 37 mT for the $\text{Co}_2\text{MnSi}/\text{CoFe}/\text{n-GaAs}$ sample is larger than that of 16 mT for the $\text{CoFe}/\text{n-GaAs}$ sample,²⁰ suggesting a greater Overhauser magnetic field due to the higher spin polarization of Co_2MnSi . The characteristic time, $(1/T_P + 1/T_1)^{-1}$, estimated from the exponential dependence of the satellite peak positions on t_{hold} is approximately 77 s for the $\text{Co}_2\text{MnSi}/\text{CoFe}/\text{n-GaAs}$ sample and 213 s for the $\text{CoFe}/\text{n-GaAs}$ sample, respectively. These values are reasonable for the time scale needed for the nuclear spins to reach the steady state through the DNP.⁷⁻¹² The value of $|2\mathbf{S}|$, which corresponds to the spin polarization in the channel, estimated from the saturation value of the Overhauser field, was 5.4% for the $\text{Co}_2\text{MnSi}/\text{CoFe}/\text{n-GaAs}$ sample and 2.3% for the $\text{CoFe}/\text{n-GaAs}$ sample, respectively. These values are comparable to the effective spin polarizations of $|P_{\text{inj}} \cdot P_{\text{det}}|^{1/2}$, estimated from the $|V_P|$ for both samples (see Table I).

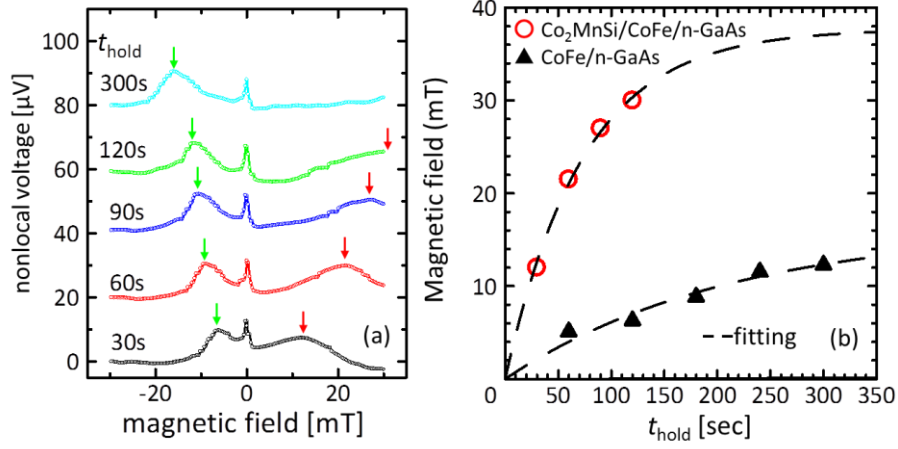


Figure 5.5. (a) t_{hold} dependence oblique Hanle signals. t_{hold} ranging from 30 to 300 seconds (b) The t_{hold} dependence of the observed satellite peak position at $B_{\text{ob}} > 0$ for a $\text{Co}_2\text{MnSi/CoFe/n-GaAs}$ sample and a CoFe/n-GaAs sample. The satellite peak position shows almost exponential dependence (dash line).

Sample structure	Annealing temperature [°C]	$ P_{\text{inj}} \cdot P_{\text{det}} ^{1/2}$ [%]
$\text{Co}_2\text{MnSi/CoFe/n-GaAs}$	350	4.4
CoFe/n-GaAs	350	3.5
CoFe/n-GaAs^{20}	—	3.0

Table I. Summary of $|P_{\text{inj}} \cdot P_{\text{det}}|^{1/2}$ in the low negative bias region for a $\text{Co}_2\text{MnSi/CoFe/n-GaAs}$ sample and CoFe/n-GaAs reference samples with and without annealing.

5.4 Coherent control of nuclear spins in GaAs

5.4.1 Electrical detection of NMR in GaAs using Co₂MnSi

In this section, we describe the electrical detection of the nuclear magnetic resonance in the Co₂MnSi/CoFe/n-GaAs sample with $t_{\text{CoFe}} = 1.3$ nm. Figure 5.6(a) shows results of oblique Hanle signals. We applied an injection current of $I = 90$ uA, where electron spins were extracted from the GaAs channel to the Co₂MnSi spin source, and \mathbf{B}_{ob} along the direction oblique by approximately 5 degree from the z -axis in the x - z plane. The device was first initialized at $B_{\text{ob}} = 200$ mT for a hold time (t_{hold}) of 180-900 seconds, so that nuclear spins became dynamically polarized. Then, the magnetic field was then swept from 200 mT. As shown in figure 5.6(a), the position of the side peaks, which indicate the magnitude of nuclear magnetic field, shifted as t_{hold} increased. Figure 5.6(c) shows oblique Hanle signals with subtracting liner component on the oblique magnetic field. We found the peak position increased, the peak height decreased, and full width at half maximum (FWHM) increased as the t_{hold} increased. Figure 5.6(d) shows the t_{hold} dependence of the peak position. As discussed in the Sec. 5.3, the peak position, or Overhauser field exponentially increased with respect to t_{hold} . From the fitting using Eq. 5.2, we obtained a saturation value of the satellite peak position of 124 mT and a characteristic time of 325 seconds. The obtained saturation value of the satellite peak position for the Co₂MnSi/CoFe/n-GaAs sample with $t_{\text{CoFe}} = 1.3$ nm was larger than the Co₂MnSi/CoFe/n-GaAs sample with $t_{\text{CoFe}} = 1.1$ nm. One reason was the higher spin polarization of the sample with $t_{\text{CoFe}} = 1.3$ nm than the sample with $t_{\text{CoFe}} = 1.1$ nm because the Overhauser field depends on the spin polarization in the GaAs channel. Another possible reason was different initialize magnetic field between two samples (30 mT for the sample with $t_{\text{CoFe}} = 1.1$ nm, and 200 mT for the sample with $t_{\text{CoFe}} = 1.3$ nm). Further investigations for the relation among characteristics time, initialize magnetic field, and spin polarization are required. From the Fig. 5.6(c), we found the peak height decreased and FWHM increased as the t_{hold} increased. These results suggested that the polarized nuclear spins had a distribution and its distribution increased with increasing the magnitude of nuclear magnetic field.²¹ To reduce the distribution, we choose oblique angle

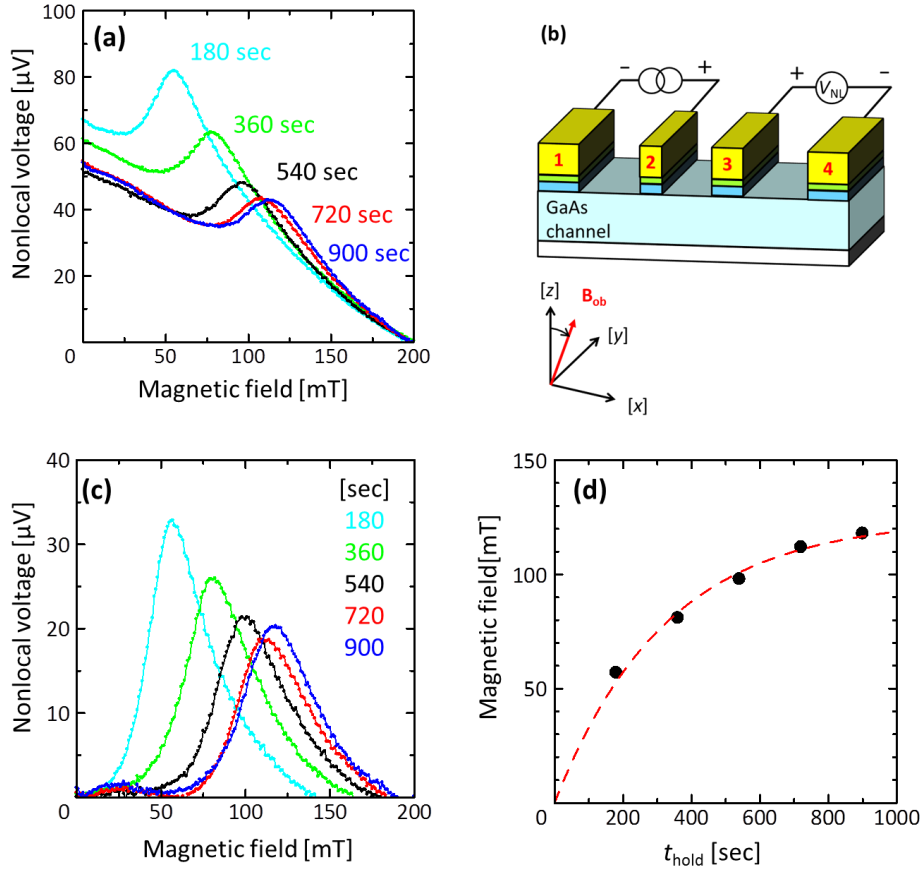


Figure 5.6. (a) Oblique Hanle signals with different t_{hold} . Injection current of $90 \mu\text{A}$ was applied with initializing magnetic field of 200 mT for t_{hold} seconds at 4.2 K. Due to the anti-parallel configuration between nuclear field and external field, electron spins stop precession at the side peak. (b) Schematic geometry of the oblique Hanle measurements. The magnetic field was applied along the direction oblique by approximately 5 degree from the z -axis in the x - z plane. (c) Oblique Hanle signals with subtracting linear component from Fig. 5.6(a). The peak height decreased and the full width at half maximum increased as the t_{hold} increased, suggesting the distribution of the nuclear spins increased. (d) t_{hold} dependence of the peak position. Exponential dependence was obtained as discussed in the Sec. 5.3.

θ to be approximately 5 degree because the magnitude of nuclear field increase as the θ increased according to Eq. 5.1.

Figure 5.7(a) shows results of oblique Hanle measurements with rf-magnetic field of 400-800 kHz applied for $t_{\text{hold}} = 180$ seconds. Application of the rf-magnetic field parallel to the y-axis direction induced the change in nonlocal voltage, and the dip positions in the oblique Hanle signals shifted as the frequency increased. From the derivative of the oblique Hanle signals with rf-magnetic field as shown in figure 5.7(c), clear three dip positions were extracted, suggesting NMR for ^{75}As , ^{69}Ga , and ^{71}Ga nuclei. Figure 5.7(d) shows applied frequency dependence of the dip positions. Linear dependences were obtained between the applied frequency and the dip positions. The obtained gyromagnetic ratios (γ) from those slopes of 4.76, 6.61, 8.27×10^7 rad/Ts for ^{75}As , ^{69}Ga , and ^{71}Ga , are close to the reported values corresponding to 4.596, 6.450, 8.196 rad/Ts.¹² These results indicated electrical detection of NMR in the spin injection device. Note that possible origins of the small difference between experimentally obtained γ values and reported ones were stray magnetic field due to ferromagnet electrodes, and Knight field originating from polarized electron spins.

The reduction of the nonlocal voltage due to NMR is explained as follows. When the NMR condition ($\gamma B_{\text{ob}} = 2\pi f_{\text{rf}}$) is satisfied where f_{rf} is a frequency of the applied rf-magnetic field, nuclear spins precess and reduces their polarization. Due to the reduction of the nuclear spin polarization, Overhauser field decreased. Thus, the total magnetic field for electron spins change from $\mathbf{B}_n + \mathbf{B}_{\text{ob}}$ to \mathbf{B}_{ob} . Here, the precession frequency of electron spins was enhanced because Overhauser field and oblique field are anti-parallel configuration for the oblique Hanle effect measurement. An enhancement of precession frequency and resultant depolarization state for electron spins indicate the reduction of nonlocal voltage.

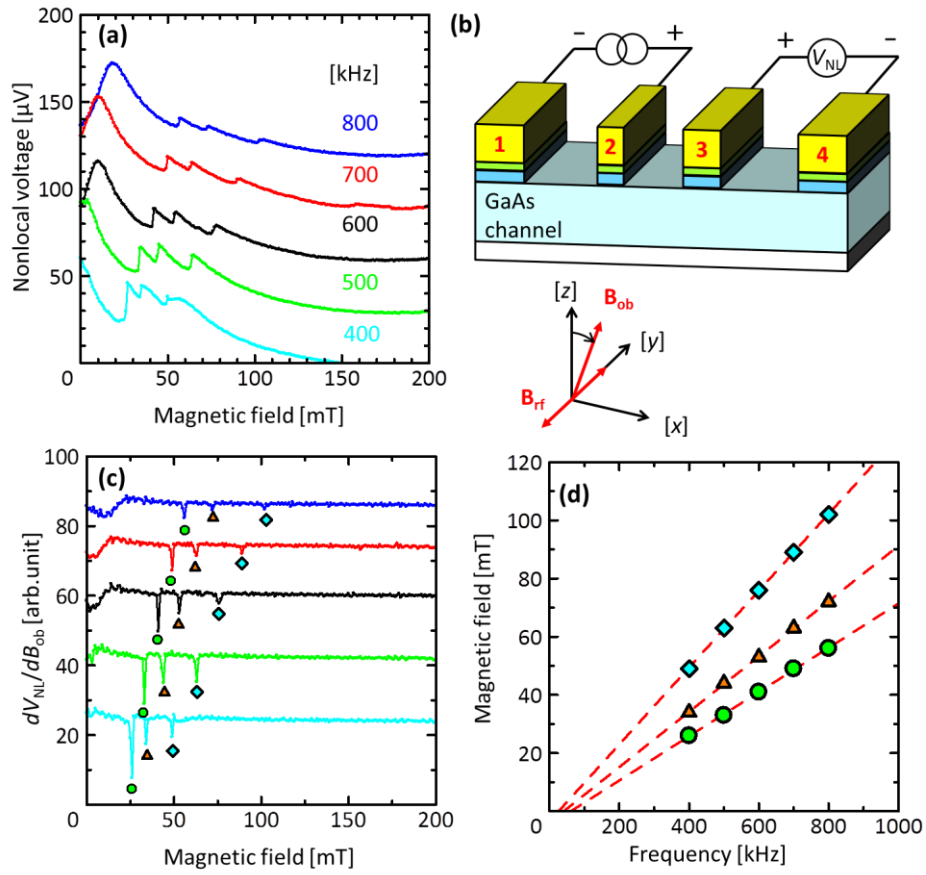


Figure 5.7. (a) Oblique Hanle signals for $t_{\text{hold}} = 180$ seconds with rf-magnetic field of 400-800 kHz applied. (b) Schematic geometry of the oblique Hanle measurements. The rf-magnetic field was applied parallel to the y -axis direction. (c) The derivative of oblique Hanle signals with rf-magnetic field. Clear three resonant positions were extracted. (d) Applied frequency dependence of the dip positions. Linear dependences were obtained between the applied frequency and the dip positions. The slopes of the curves for the dip positions vs. frequency were close to respective gyromagnetic ratio values of ^{71}Ga , ^{69}Ga , and ^{75}As , indicating that the origin of the dips was NMR.

5.4.2 Coherent control of nuclear spins using pulsed NMR

In the following, we focused on ^{69}Ga . Figure 5.8 shows f_{rf} dependence of the nonlocal voltage with a static magnetic field of 113 mT. The rf-magnetic field was continuously applied during the measurement and f_{rf} was swept from higher (lower) to lower (higher) frequency with a sweep rate of 200 Hz/sec corresponding to the red (black) curve. As explained in 5.4.1, when NMR occurred, electron spins precessed because the cancellation condition between Overhauser field and static magnetic field was not satisfied, resulting in reduction of nonlocal voltage. Because the sweep rate of the frequency was faster than the time scale for nuclear spins to be the steady state, nuclear spins kept depolarized states during the single scan. Thus, electron spins also kept precessing and dip structure as observed in conventional NMR measurements was not obtained in nonlocal voltage. From a cross point of these curves, we determined resonance frequency of 1170 kHz. Although ^{69}Ga , ^{71}Ga and ^{75}As have nuclear spin moments of 3/2, the evidence of a four-level state

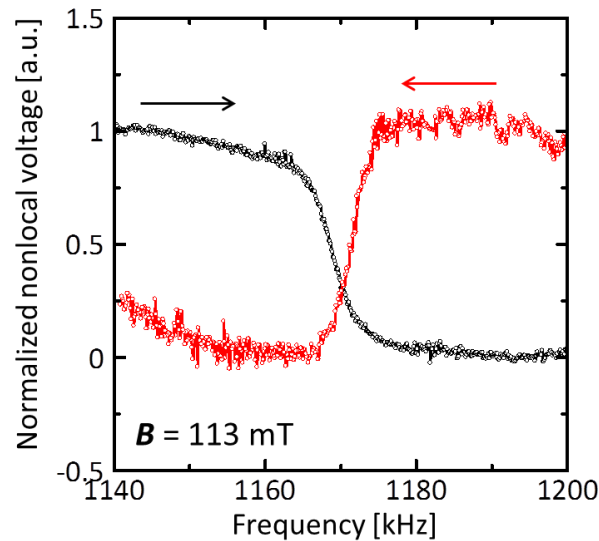


Figure 5.8. Frequency dependence of the nonlocal voltage with a static magnetic field of 113 mT. The rf-magnetic field was continuously applied and the frequency of the rf-magnetic field was swept from higher (lower) to lower (higher) frequency, corresponding to the red (black) curve.

due to the quadpolar splitting was not observed in this measurement.

We prepared the initial nuclear spin state by applying injection current of 90 μA and the static magnetic field of 113 mT for 300 seconds. Then, superposition of the up-spin and down-spin states, $|0\rangle$ and $|1\rangle$, was generated by applying pulsed rf-magnetic field with a frequency of 1170 kHz and width of t_{rf} ranging from 8 to 600 μsec . Figure 5.9(a) shows a typical time (t) evolution of nonlocal voltage with $t_{\text{rf}} = 96 \mu\text{sec}$ applied at $t = 0$. Nuclear spins coherently rotate between $|0\rangle$ and $|1\rangle$ states during the rf-magnetic field radiation, and back to the initial state with spending the 300 sec after the rf-magnetic field radiation. Thus, the nonlocal voltage change, defined by $\Delta V_{\text{NL}} = V_{\text{NL}}(t = 0) - V_{\text{NL}}(t = 300)$, indicates final states of nuclear spins immediately after the rf-magnetic field pulse radiation.

Similar measurements were carried out with different rf-magnetic field width t_{rf} . Figure 5.9(b) shows a color scale plot of V_{NL} as a function of t_{rf} and t . A clear oscillatory behavior of V_{NL} as a function of τ_p , indicating the first demonstration of Rabi oscillation in spin injection devices was observed. Figure 5.9(c) shows t_{rf} dependence of ΔV_{NL} with different ac-voltage for the coil to apply rf-magnetic field. We observed Rabi oscillation, indicating coherent control of nuclear spins. Red lines in the Fig. 5.9(c) are described by¹⁵

$$V_{\text{NL}}(t_{\text{rf}}) = \frac{A_1}{1 + (g\mu_B B(t_{\text{rf}})\tau/\hbar)^2} + A_2, \quad (5.3)$$

$$B(t_{\text{rf}}) = A_3 \{1 - \cos(2\pi f_{\text{Rabi}} t_{\text{rf}}) \exp(-t_{\text{rf}}/T_{\text{Rabi}})\}, \quad (5.4)$$

where A_1 , A_2 , and A_3 is a constant, g is an electron g-factor ($g = -0.44$ for GaAs), μ_B is the Bohr magneton, τ is an electron spin lifetime, \hbar is the reduced Plank's constant, T_{Rabi} is an effective dephasing time of Rabi oscillation, and f_{Rabi} is a Rabi frequency. This approximation is valid in the case for spin diffusion length is much larger than the space between the injector and detector contacts, which condition is satisfied in our device. Although there is a small discrepancy, the plot of ΔV_{NL} vs. τ_{rf} can be fitted well with Eqs. (5.3) and (5.4). The possible origin of the discrepancy for the model and experimental results are influence of \mathbf{B}_n parallel to x or y direction. When \mathbf{B}_n orient to the x or y direction due to pulsed-NMR, electron spins precess because $\mathbf{B}_n \times \mathbf{S} \neq 0$ is satisfied, resulting in a reduction of V_{NL} . However, the influence of x or y component of $\mathbf{B}_n(t_{\text{rf}})$ on the Hanle signals is ignored in the simplified model. Another possible origin of the discrepancy would come from the insufficient initialization condition. As shown in Fig. 5.6(d), it took around 900 sec for nuclei of ^{69}Ga , ^{71}Ga , and ^{75}As to be fully polarize.

Figure 5.9 (d) shows estimated f_{Rabi} using Eqs. (5.3) and (5.4), with different ac-voltage

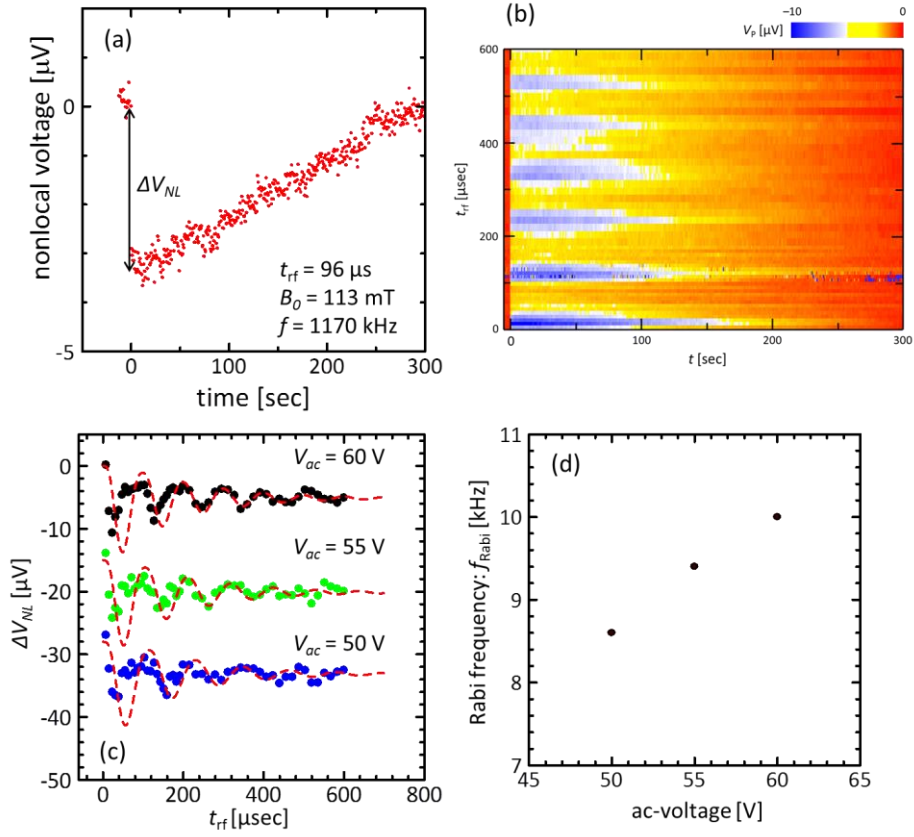


Figure 5.9 (a) Time (t) evolution of nonlocal voltage. A pulsed rf-magnetic field having width of t_{rf} was induced at $t = 0$. Amplitude of nonlocal voltage change ΔV_{NL} , defined by $V_{NL}(t = 0) - V_{NL}(t = 300)$, indicates final states of nuclear spins immediately after the rf-magnetic field pulse radiation. Similar measurements were carried out with different t_{rf} . (b) A color scale plot of V_{NL} as a function of t_{rf} and t . (c) t_{rf} dependence of V_P with different ac-voltage for the coil to apply rf-magnetic fields. (d) Applied ac-voltage dependence of f_{Rabi} . f_{Rabi} was lineally increased with increasing ac-voltage due to $2\pi f_{Rabi} = \gamma B_{rf}$.

for the coil to apply rf-magnetic field. f_{Rabi} was lineally increased with increasing ac-voltage. This result also indicate observed oscillation is the Rabi oscillation because of $2\pi f_{\text{Rabi}} = \gamma B_{\text{rf}}$. The estimated amplitude of rf-magnetic field using f_{Rabi} and $\gamma(^{69}\text{Ga})$ was around 1 mT when the ac-voltage of 60 V. This value is consistent with our bipolar amplifier and the coil circuit. Estimated T_{Rabi} was around 200 μsec for three curves in the figure 5.9 (c). The obtained T_{Rabi} in our spin injection devices is reasonable because values of T_{Rabi} from 100 to 1500 μsec were reported by other system.¹³⁻¹⁵ It is known that T_{Rabi} is affected by the existence of inhomogeneous field. However, detected nuclear spins below the detector contact in this study was in a volume of $1.0 \times 10 \times 2.5 \mu\text{m}$. Thus, inhomogeneous static and rf-magnetic field was negligible in the small space.

We observed Rabi oscillations and demonstrated coherent control nuclear spins in GaAs which means we could obtain any desired superposition of nuclear spin state by controlling pulse width. This is because highly electron spin polarization and resulting highly nuclear spin polarization were demonstrated. These results indicate Heusler alloy Co_2MnSi is promising spin source for creating the solid-state nuclear spin quantum bit, and other viable spintronic devices such as spin transistors. Coherent control of nuclear spins in spin injection devices has advantages such as smaller magnetic field and higher temperature compared with quantum Hall systems, scalable, and a simple semiconductor layer structure.

5.5 Summary

We demonstrated all-electrical polarization and detection of nuclear spins through oblique Hanle signals. Using Co_2MnSi spin source, significantly higher nuclear fields were obtained compared by the sample with the CoFe spin source. Analysis of transient behavior of nuclear spins gave an important insight towards an understanding of nuclear spin dynamics. In particular, we found initialization method for nuclear spins using spin injection devices from the investigation of characteristic time for nuclear spins to reach the steady state.

We demonstrated electrical detection of NMR using spin injection devices. Using pulsed NMR, we observed Rabi oscillation. From the observation of Rabi oscillation, we could control nuclear spin states described by a superposition of up- and down-spin states by

controlling the pulse width. These results indicate Co_2MnSi spin source is promising for advancing the implementation of nuclear-spin-based quantum bits and other spintronic devices.

References

1. I. L. Chuang, L. M. K. Vandersypen, X. Zhou, D. W. Leung, and S. Lloyd, *Nature* (London) **393**, 143 (1998).
2. M. A. Nielsen and I. L. Chuang, *Quantum Computation and Quantum Information*, (Cambridge Univ. Press, Cambridge, 2000)
3. R. Kaji, S. Adachi, H. Sasakura, and S. Muto, *Phys. Rev. B* **77**, 115345 (2008).
4. J. M. Kikkawa and D. D. Awschalom, *Science* **287**, 473 (2000)..
5. D. Gammon, Al. L. Efros, T. A. Kennedy, M. Rosen, D. S. Katzer, D. Park, S. W. Brown, V. L. Korenev, and I. A. Merkulov, *Phys. Rev. Lett.* **86**, 5176 (2001).
6. F. Meier and B. P. Zakharchenya, Edits. *Optical Orientation*, (North-Holland, New York, 1984).
7. T. Akiho, J. Shan, H.-x. Liu, K.-i. Matsuda, M. Yamamoto, and T. Uemura, *Phys Rev. B*, **87**, 235205 (2013).
8. J. Strand, X. Lou, C. Adelman, B. D. Schultz, A. F. Isakovic, C. J. Palmstrøm, and P. A. Crowell, *Phys. Rev. B* **72**, 155308 (2005).
9. P. Van Dorpe, W. Van Roy, J. De Boeck, and G. Borghs, *Phys. Rev. B* **72**, 035315 (2005).
10. M. K. Chan, Q. O. Hu, J. Zhang, T. Kondo, C. J. Palmstrøm, and P. A. Crowell, *Phys. Rev. B* **80**, 161206(R) (2009).
11. G. Salis, A. Fuhrer, and S. F. Alvarado, *Phys. Rev. B* **80**, 115332(R) (2009).
12. J. Shiogai, M. Ciorga, M. Utz, D. Schuh, T. Arakawa, M. Kohda, K. Kobayashi, T. Ono, W. Wegscheider, D. Weiss, and J. Nitta, *Appl. Phys. Lett.* **101**, 212402 (2012).
13. T. Machida, T. Yamazaki, K. Ikushima, and S. Komiyama, *Apply. Phys. Lett.*, **82**, 409 (2003).
14. G. Yusa, K. Muraki, K. Takashina, K. Hashimoto, and Y. Hirayama, *Nature* **434**, 1001 (2005).
15. H. Sanada, Y. Kondo, S. Matsuzaka, K. Morita, C. Y. Hu, Y. Ohno, and H. Ohno, *Phys. Rev. Lett.* **96**, 067602 (2006).

16. Y. Ebina, T. Akiho, H.-x. Liu, M. Yamamoto, and T. Uemura, *Appl. Phys. Lett.* **104**, 172405 (2014).
17. H.-x. Liu, Y. Honda, T. Taira, K.-i. Matsuda, M. Arita, T. Uemura, and M. Yamamoto, *Appl. Phys. Lett.* **101**, 132418 (2012).
18. G.-f. Li, Y. Honda, H.-x. Liu, K.-i. Matsuda, M. Arita, T. Uemura, M. Yamamoto, Y. Miura, M. Shirai, T. Saito, F. Shi and P. M. Voyles, *Phys. Rev. B* **89**, 014428 (2014).
19. D. Paget, G. Lampel, B. Sapoval, and V. I. Safarov, *Phys. Rev. B* **15**, 5780 (1977).
20. T. Uemura, T. Akiho, M. Harada, K.-i. Matsuda, and M. Yamamoto, *Appl. Phys. Lett.* **99**, 082108 (2011).
21. I. A. Merkulov, Al. L. Efros and M. Rosen, *Phys. Rev. B* **65**, 205309 (2002).

Chapter 6

Conclusion

This research produced five important results.

1. The tunneling anisotropic magnetoresistance effect was suppressed by inserting an MgO barrier between the CoFe and n-GaAs layers, indicating Fermi-level depinning and lowering of the Schottky barrier height of GaAs. The non-local spin-valve signal was enhanced by a factor of 38, and the sign was reversed when an MgO barrier was inserted, suggesting that the effective spin polarization increased.
2. Efficient spin injection was achieved by using a Co_2MnSi spin source. The maximum spin polarization in the GaAs channel observed in the sample with Co_2MnSi electrodes was larger than that observed in the reference sample with CoFe electrodes; this was due to the higher spin polarization of Co_2MnSi . These results indicate that the Heusler alloy is a promising spin source for spin injection into a semiconductor.
3. Spin injection into a GaAs channel and into strained InGaAs channels was detected by observation of spin-valve signals and Hanle signals using Fe electrodes. The obtained spin lifetime was much shorter for the strained InGaAs channels. Possible origins of this reduction were considered, and strain-induced spin orbit interaction was found to explain these results. The spin-dependent transport properties of strained InGaAs channels was clarified using all-electrical method. This method can be used as a tool for probing the effect of the spin relaxation mechanism as well as for realizing future semiconductor-based spintronics devices.
4. All-electrical polarization and detection of nuclear spins was demonstrated using through oblique Hanle signals. Using a Co_2MnSi spin source created significantly higher nuclear fields. Analysis of the transient behavior of nuclear spins gave an

important insight towards an understanding of nuclear spin dynamics. In particular, an initialization method for nuclear spins using spin injection devices was found by investigating the characteristic time for nuclear spins to reach the steady state.

5. Electrical detection of NMR was demonstrated using spin injection devices. Significantly larger NMR signals were obtained by using a Co_2MnSi spin source. Using pulsed NMR produced Rabi oscillation. From observation of Rabi oscillation, we could control the nuclear spin states described by a superposition of up- and down-spin states by controlling the pulse width. These results are promising for advancing the implementation of nuclear-spin-based quantum bits.

In conclusion, efficient spin injection using an MgO tunnel barrier and a Heusler alloy of Co_2MnSi was demonstrated, the transport properties of electron spins in GaAs and strained InGaAs channels were clarified, efficient polarization of nuclear spins and nuclear magneto resonance was detected, and coherent control of nuclear spins was demonstrated in spin injection devices. These research findings are applicable to novel next-generation spintronics devices such as spin transistors and nuclear spin solid-state quantum bits.

Acknowledgements

I would like to thank Professor Masafumi Yamamoto for his thoughtful discussion, advice and sincere encouragement over the year. I am sure that his advice and discussion improved this works.

I gratefully acknowledge my supervisor Associate Professor Tetsuya Uemura for his valuable discussions, support, and guidance from the early stage of this research. I sincerely feel that any achievements are due to his continuing support.

Likewise, I am grateful to Assistant Professor Kenichi Matsuda for his support and assistance on measurement setup for devices.

I am grateful to Professor Yasuo Takahashi for reviewing this thesis and offering his helpful comments.

I want to thank Masanobu Harada, Tomoyuki Taira, and all the students of the Laboratory of Nanoscale Electron Devices.

Finally, I want to thank my parents for their support and generous encouragement.

This work was partially supported by a Research Fellowship for Young Scientists from the Japan Society for the Promotion of Science.

Appendix

Publications related to this thesis

- [1] T. Akiho, T. Uemura, M. Harada, K. Matsuda, and M. Yamamoto: “Suppression of tunneling anisotropic magnetoresistance effect in $\text{Co}_2\text{MnSi}/\text{MgO}/\text{n-GaAs}$ and $\text{CoFe}/\text{MgO}/\text{n-GaAs}$ junctions by inserting a MgO barrier,” *Appl. Phys. Lett.*, **98**, 232109 (2011).
- [2] T. Akiho, T. Uemura, M. Harada, K. Matsuda, and M. Yamamoto: “Effect of MgO barrier insertion on spin-dependent transport properties of $\text{CoFe}/\text{n-GaAs}$ heterojunctions,” *Jpn. J. Appl. Phys.*, **51**, 02BM01 (2012).
- [3] T. Akiho, J. Shan, H-x. Liu, K. Matsuda, M. Yamamoto, and T. Uemura: “Electrical injection of spin-polarized electrons and electrical detection of dynamic nuclear polarization using a Heusler alloy spin source,” *Phys. Rev. B*, **87**, 235205 (2013).

Publications related to other research

- [1] T. Uemura, M. Harada, T. Akiho, K. Matsuda, and M. Yamamoto: “Influence of GaAs surface structure on tunneling anisotropic magnetoresistance and magnetocrystalline anisotropy in epitaxial $\text{Co}_{50}\text{Fe}_{50}/\text{n-GaAs}$ junctions,” *Appl. Phys. Lett.*, **98**, 102503 (2011).
- [2] T. Uemura, T. Akiho, M. Harada, K. Matsuda, and M. Yamamoto: “Non-local detection of spin-polarized electrons at room temperature in $\text{Co}_{50}\text{Fe}_{50}/\text{GaAs}$ Schottky tunnel junctions,” *Appl. Phys. Lett.*, **99**, 082108 (2011).
- [3] S. Nanot, A. W. Cummings, C. L. Pint, A. Ikeuchi, T. Akiho, K. Sueoka, R. H. Hauge, F. Leonard, and J. Kono: “Broadband, polarization-sensitive photodetector based on optically-thick films of macroscopically long, dense, and aligned carbon nanotubes,” *Scientific Reports*, **3**, 1335 (2013).
- [4] Y. Ebina, T. Akiho, H.-x. Liu, M. Yamamoto, and T. Uemura: “Effect of CoFe insertion in $\text{Co}_2\text{MnSi}/\text{CoFe}/\text{n-GaAs}$ junctions on spin injection properties,” *Appl. Phys. Lett.*, **104**, 172405 (2014).

Presentations

- [1] T. Akiho, M. Harada, T. Uemura, K.-i. Matsuda, and M. Yamamoto: “Spin-dependent transport properties of Co₂MnSi/MgO/n-GaAs tunnel junctions,” IEEE Int’l Magnetism Conf. 2011, Taipei, Taiwan, April 25-29, 2011.
- [2] T. Akiho, M. Harada, T. Uemura, K.-i. Matsuda, and M. Yamamoto: “Spin injection from Co₅₀Fe₅₀ into GaAs at room temperature,” 5th Int’l Workshop on Spin Currents, Sendai, Japan, July 25-28, 2011.
- [3] T. Akiho, M. Harada, T. Uemura, K.-i. Matsuda, and M. Yamamoto: “Effect of MgO Barrier Insertion on Spin-dependent Transport Properties of CoFe/n-GaAs,” 2011 Int’l Conf. on Solid State Devices and Materials, Nagoya, Japan, September 28-30, 2011.
- [4] T. Akiho, T. Uemura, K.-i. Matsuda, and M. Yamamoto: “Electrical spin injection from Co₂MnSi Heusler alloy into GaAs and electrical detection of dynamic nuclear polarization,” IEEE Int’l Magnetism Conf. 2012, Vancouver, Canada, May 7-11, 2012.
- [5] T. Akiho, T. Uemura, K.-i. Matsuda, and M. Yamamoto: “Electrical spin injection and electrical detection of dynamic nuclear polarization in ferromagnet/semiconductor heterojunctions,” Int’l Workshop on Spintronic Nano Materials 2012, Sapporo, Japan, November 5-6, 2012.
- [6] T. Akiho, J.-h. Shan, K.-i. Matsuda, M. Yamamoto, and T. Uemura: “Transient effects on oblique Hanle signals observed in ferromagnet/semiconductor heterojunctions with non-local four-terminal configuration,” 12th Joint MMM/Intermag Conf., Chicago, Illinois, USA, January 14 – 18, 2013.
- [7] T. Akiho, M. Yamamoto, and T. Uemura: “Spin-dependent transport properties of strained InGaAs channel investigated through all electrical spin injection and detection,” 58th Annual Conf. on Magnetism and Magnetic Materials, Denver, Colorado, USA, November 4 – 8, 2013.
- [8] T. Akiho, Y. Ebina, H.-x. Liu, M. Yamamoto, and T. Uemura: “Efficient dynamic nuclear polarization using electrical spin injection from a half-metallic spin source,” 32nd International Conf. on the Physics of semiconductors, Austin, Texas, USA, August 10–15, 2014.

- [9] 秋保貴史, 原田雅亘, 植村哲也, 松田健一, 山本眞史: 「Co₂MnSi/n-GaAs 接合におけるトンネル異方性磁気抵抗効果の MgO 層挿入効果」 PASPS-15, つくば市, 2010年12月20日-21日.
- [10] 秋保貴史, 植村哲也, 原田雅亘, 松田健一, 山本眞史: 「CoFe/n-GaAs ヘテロ接合におけるスピン依存伝導特性の MgO 層挿入効果」第72回応用物理学会学術講演会, 山形市, 2011年8月29日-9月2日.
- [11] 秋保貴史, 原田雅亘, 植村哲也, 松田健一, 山本眞史: 「Co₂MnSi を用いた GaAs へのスピン注入および動的核スピンの検出」 PASPS-16, 東京都目黒区, 2011年11月28日-29日.
- [12] T. Akiho, T. Uemura, K.-i. Matsuda, M. Yamamoto: “Electrical spin injection from Co₂MnSi Heusler alloy into GaAs and electrical detection of dynamic nuclear polarization,”第59回応用物理学関係連合講演会, 東京都新宿区, 2012年3月15日-18日.
- [13] T. Akiho, J. Shan, K.-i. Matsuda, M. Yamamoto, and T. Uemura: “Annealing temperature dependence of spin signals observed in Co₂MnSi/CoFe/n-GaAs through four-terminal non-local geometry,”第60回応用物理学会春季学術講演会, 厚木市, 2013年3月27-30日.
- [14] 秋保貴史, 劉宏喜, 蝦名優也, 山本眞史, 植村哲也: 「Co₂MnSi/CoFe/n-GaAs 接合における動的核スピン偏極」第37回日本磁気学会学術講演会, 札幌市, 2013年9月3日-6日.
- [15] T. Akiho, H.-x. Liu, K.-i. Matsuda, M. Yamamoto, and T. Uemura: “Highly-efficient dynamic nuclear polarization in GaAs using a Heusler-alloy spin source”第74回応用物理学会秋季学術講演会, 京田辺市, 2013年9月16日-20日.
- [16] T. Akiho, M. Yamamoto, T. Uemura: “Spin lifetime in strained InGaAs channels investigated through all electrical spin injection and detection” PASPS-18, 豊中市, 2013年12月9-10日.
- [17] T. Akiho, M. Yamamoto, T. Uemura: “Spin lifetime in strained InGaAs channels investigated in four-terminal nonlocal geometry”第61回応用物理学会春季学術講演会, 相模原市, 2014年3月17日-20日.
- [18] T. Akiho, Y. Ebina, H.-x. Liu, M. Yamamoto, and T. Uemura: “Electrical detection

of nuclear magnetic resonance in GaAs using transient oblique Hanle signals”第 75
回応用物理学会秋季学術講演会，札幌市， 2014 年 9 月 17 日－20 日.